Electron spin and charge in semiconductor quantum dots

Electron spin and charge in semiconductor quantum dots

Proefschrift

ter verkrijging van de graad van doctor
aan de Technische Universiteit Delft,
op gezag van de Rector Magnificus prof.dr.ir. J.T. Fokkema,
voorzitter van het College voor Promoties,
in het openbaar te verdedigen
op vrijdag 15 oktober 2004 om 15.30 uur

door

Jeroen Martijn ELZERMAN

natuurkundig ingenieur
geboren te Leiderdorp.

Dit proefschrift is goedgekeurd door de promotor:
Prof. dr. ir. L. P. Kouwenhoven

Samenstelling van de promotiecommissie:

Rector Magnificus,	voorzitter
Prof. dr. ir. L. P. Kouwenhoven	Technische Universiteit Delft, promotor
Prof. dr. S. Tarucha	Tokyo University, Japan
Prof. dr. D. Loss	Universität Basel, Zwitserland
Prof. dr. W. F. Brinkman	Princeton University, Verenigde Staten
Prof. dr. P. H. Kes	Universiteit Leiden
Prof. dr. Yu. V. Nazarov	Technische Universiteit Delft
Dr. ir. L. M. K. Vandersypen	Technische Universiteit Delft

Published and distributed by: DUP Science

DUP Science is an imprint of
Delft University Press
P.O. Box 98 Telephone: +31 15 27 85678
2600 MG Delft Telefax: +31 15 27 85706
The Netherlands E-mail: info@library.tudelft.nl

ISBN 90-407-2533-0

Keywords: quantum dots, spin qubits, Kondo effect

Cover design: Tremani <www.tremani.nl>

Copyright © 2004 by Jeroen Elzerman

All rights reserved. No part of the material protected by this copyright notice may be reproduced or utilized in any form or by any means, electronic or mechanical, including photocopying, recording or by any information storage and retrieval system, without written permission from the publisher: Delft University Press.

Printed in the Netherlands

Preface

Halfway through my M.Sc. studies in Delft, many years ago now, I was thinking about changing to a different university, a different field, maybe even dropping out of university and getting a job. I found many of the physics courses tedious and I did not enjoy living in Delft – I was generally unhappy. After about a year of doing anything except studying, I decided that it would be much better if I finished my studies anyway. I started to attend lectures about quantum mechanics and mesoscopic physics, and I began to enjoy reading and thinking about the strange ways of nature again. I remembered why I like physics.

When I joined the Quantum Transport group of Hans Mooij for my final M.Sc. project, I found a large group of motivated people from many different countries, all sharing this fascination with science. Their enthusiasm lead them to spend evenings or sometimes nights in the lab, trying to perform difficult and exciting experiments. At the same time, they were not nerds but had an active interest in things like music, art, and football. I would like to thank all the people I have met in QT for creating this atmosphere in which I immediately felt at home. You have been a decisive factor in deciding to stay in the group as a Ph.D. student – I hold you directly responsible!

This thesis is the result of an intense collaboration with many people in the quantum dot section. First of all, I am grateful to my Ph.D. advisor Leo Kouwenhoven for his great intuiton in finding interesting lines of research, and in attracting interesting people to join the group. He has also given me the opportunity to go abroad to many conferences at beautiful locations (to which he himself was invited). I have really enjoyed working closely together with Silvano De Franceschi: we started in QT at the same time, and we finish together as well. Even after all this time in the Netherlands, you are still an Italian in spirit, and I have enjoyed your mediterranean temperament, as well as your shouting and cursing (in Italian) on the football field. Wilfred van der Wiel, my supervisor when I first came into the group and my predecessor as quantum dot graduate student, has impressed me with his charm in dealing with people, always knowing how to say the most important things in just about every language on the planet.

I owe great thanks to my fellow ‘Spin Doctors’: Ronald Hanson, Laurens Willems van Beveren, Lieven Vandersypen and Frank Koppens. Ronald has been my experimental sparring partner for the last three years. I have learned a lot from his critical analysis of everything, from our work to life in general. Laurens – who actually has the entire Internet on his computer – has always been able to cheer me up when experiments were not going well, by telling a very bad joke in a way that makes it contageously funny. Lieven has joined the Spin Qubit team when it was just in its infancy, and has contributed greatly to the way its success, by his very organised approach to everything. Finally, Frank Koppens has said goodbye to a brilliant carreer in the energy providing business, in order to build a spin quantum computer. Thank you all for everything!

There is no better way to really understand something than to try and explain it to someone else. I was fortunate to have worked with a number of students, whom I would like to thank for their essential contributions to this work: Joris Wijpkema, Jacob Greidanus, Benoit Witkamp and Ivo Vink. Joris, we made our first steps into the world of QPC charge detection, the technique that I am sure will become the standard for spin qubit research. (But do you remember the Stückelberg oscillations?) Jacob, you are the only person I know who is at the same time a ‘player’, a would-be millionaire, and a christian-democrat. You have set a new standard for the acknowledgment section of students’ reports, Soul Brotha! Benoit, you programmed the entire data acquisition setup, so that we could take enough data for you to spend weeks (months?) on painstaking data analysis (up down down up up...). I hope the Nature was worth it. And Ivo, even as a student you were more valuable than some AIO’s. Good luck with the fridge! Thanks also to Jort Wever and Wouter Naber, kings of the cleanroom.

The quantum dot project has benefited tremendously from the collaboration with Professor Seigo Tarucha, who has had a large influence on this work through the ERATO project that I was a part of, for which I am very grateful. I would also like to thank Satoshi Sasaki for fabricating the vertical dots that were used to measure the singlet-triplet Kondo effect, and Mikio Eto, who provided the theoretical explanation. Furthermore, I am very grateful to Yoshiro Hirayama, Toshimasa Fujisawa, Toshiaki Hayashi and Tadashi Saku, for the many wafers and samples that were made at NTT Basic Research Laboratories in Atsugi, Japan.

On the theortical side, I would like to thank Yuli Nazarov for the always enlightening discussions about spin and Kondo effects. Many thanks also to Miriam Blaauboer, Siggi Erlingsson and Maarten Wegewijs for their theoretical input. The spin qubit project has benefited a lot from interactions with the theory group of Daniel Loss in Basel. We have learned from Daniel and Guido

Burkard, Hansres Engel and Vitaly Golovach many things ranging from what the electrochemical potential really is, to the concept of spin-to-charge conversion. It was also very nice to discuss with David DiVincenzo, the other spin-qubit guru. Finally, I am grateful to Jean-Paul Leburton for the simulations of our Gundam devices.

For the more practical help, I acknowledge the technical support from Mascha van Oossanen, Leo Lander, Willem den Braver, Wim Schot and Leo Dam. And of course there is Bram van der Enden, who has solved many experimental problems, as well as being a dominant figure in QT. Raymond Schouten has made vital contributions to the electronic part of the measurement setup. Without him, spin read-out would have been impossible. I am also thankful to Kees Harmans for help with the fridge, the electronics and the high-frequency equipment. Thanks to Herre van der Zant for the fascinating insights into group and university politics, to Peter Hadley for the physics classes I taught to Electronics students, and of course to Hans Mooij for bringing together a great group of people.

Among the many colleagues and friends I would especially like to thank Hannes Majer (the Jazz Man), Eugen Onac (the Pula Man), my office mates Alexander ter Haar and Adrian Lupascu (who have helped to introduce 'neo-professionalism' and other typical Room 1 concepts), Floor Pauw, Floris Zwaneveld, Dionne Klein and Daniel Huertas Hernando, Alberto Morpurgo, Hon Tin Man, Ewout Eijkelenboom, Nathan Kemeling, Liesbeth Venema and of course Yuki French Nakagawa. Plus everyone in the football team. Domou arigatou to all!

Most importantly, I thank my family and friends, especially Gerard Ruitenberg, Miklós Hoffer, Ib Waterreus and Merlijn Donk; de Zwolsche Boys. For their enduring friendship, even through the times when I was always in the lab, not answering my phone or replying to your mail. To my parents and brothers: I am very thankful for all the support you gave me when I was not as happy as I am now. And most of all I thank Hajnalka, for always keeping confidence in me. Nagyon szeretlek!

Jeroen Elzerman
Delft, September 2004

Contents

1 Introduction **1**
1.1 Quantum computing 2
1.2 Implementations 4
1.3 The spin qubit 5
1.4 Quantum dots 8
1.5 Transport though quantum dots 10
1.6 Spin configurations in few-electron quantum dots 15
1.7 Kondo effect in quantum dots 18
1.8 Measurement setup 21
1.9 Sample stability 26
1.10 Outline of this thesis 28
References 29

2 Few-electron quantum dot circuit with integrated charge read-out **33**
2.1 Few-electron quantum dots 34
2.2 Samples 36
2.3 Quantum Point Contact as charge detector 38
2.4 Double dot charge stability diagram 40
2.5 Tunable tunnel barriers in the few-electron regime 41
2.6 Photon-assisted tunneling 44
References 46

3 Excited-state spectroscopy on a nearly closed quantum dot via charge detection **49**
3.1 Introduction 50
3.2 Tuning the tunnel barriers 50
3.3 Excited-state spectroscopy for $N = 1$ 53
3.4 Excited-state spectroscopy for $N = 2$ 55
References 57

4 Real-time detection of single electron tunneling using a quantum point contact 59

4.1 Charge detectors 60
4.2 Sample and setup 60
4.3 Sensitivity and speed 62
4.4 Real-time single electron tunneling 64
4.5 QPC *vs.* SET 65
References 66

5 Single-shot read-out of an individual electron spin in a quantum dot 69

5.1 Measuring electron spin in quantum dots 70
5.2 Implementation 70
5.3 Two-level pulse technique 71
5.4 Tuning the quantum dot into the read-out configuration 74
5.5 Single-shot read-out of one electron spin 75
5.6 Measurement fidelity 77
References 80

6 Semiconductor few-electron quantum dots as spin qubits 85

6.1 Introduction 86
6.2 Qubit 86
6.3 Read-out 87
6.4 Initialization 90
6.5 Coherence times 91
6.6 Coherent single-spin manipulation: ESR 92
6.7 Coherent spin interactions: $\sqrt{\text{SWAP}}$ 94
6.8 Unresolved issues 95
6.9 Conclusion and outlook 96
References 97

7 The Kondo effect in the unitary limit 99

7.1 Introduction 100
7.2 Strong Kondo effect at $B = 0.4$ T 100
7.3 Unitary limit of conductance 102
7.4 Kondo temperature and scaling 103
7.5 Suppression of Kondo effect at $B = 0$ T 106
7.6 Aharonov-Bohm oscillations 106
References 108

8 Kondo effect in an integer-spin quantum dot 111
8.1 Kondo effect for odd and even N 112
8.2 Enhanced Kondo effect at singlet-triplet degeneracy 114
8.3 Lifting the singlet-triplet degeneracy 119
References 120

9 Electron cotunneling in a semiconductor quantum dot 123
9.1 Elastic and inelastic cotunneling 124
9.2 Charge stability diagram 124
9.3 Measuring the charge stability diagram in the few-electron regime 126
9.4 Resonance width for first-and higher-order tunneling 128
9.5 Optimum energy resolution 130
References 131

Summary 133

Samenvatting 137

Curriculum Vitae 141

List of publications 143

Chapter 1

Introduction

1.1 Quantum computing

More than three quarters of a century after its birth, quantum mechanics remains in many ways a peculiar theory [1]. It describes many physical effects and properties with great accuracy, but uses unfamiliar concepts like superposition, entanglement and projection, that seem to have no relation with the everyday world around us. The interpretation of these concepts can still cause controversy. The inherent strangeness of quantum mechanics already emerges in the simplest case: a quantum two-level system. Unlike a classical two-level system, which is always either in state 0 or in state 1, a quantum two-level system can just as well be in a *superposition* of states $|0\rangle$ and $|1\rangle$. It is, in some sense, in both states at the same time.

Even more exotic states can occur when two such quantum two-level systems interact: the two systems can become *entangled*. Even if we know the complete state of the system as a whole, for example $(|01\rangle - |10\rangle)/\sqrt{2}$, which tells us all there is to know about it, we cannot know the state of the two subsystems individually. In fact, the subsystems do not even have a definite state! Due to this strong connection between the two systems, a measurement made on one influences the state of the other, even though it may be arbitrarily far away. Such spooky non-local correlations enable effects like 'quantum teleportation' [2, 3].

Finally, the concept of measurement in quantum mechanics is rather special. The evolution of an isolated quantum system is deterministic, as it is governed by a first order differential equation – the Schrödinger equation. However, coupling the quantum system to a measurement apparatus forces it into one of the possible measurement eigenstates in an apparently non-deterministic way: the particular measurement outcome is random, only the probability for each outcome can be determined [1]. The question of what exactly constitutes a measurement is still not fully resolved [4].

These intriguing quantum effects pose fundamental questions about the nature of the world we live in. The goal of science is to explore these questions. At the same time, this also serves a more opportunistic purpose, since it might allow us to actually *use* the unique features of quantum mechanics to do something that is impossible from the classical point of view.

And there are still many things that we cannot do classically. A good example is prime-factoring of large integers: it is easy to take two prime numbers and compute their product. However, it is difficult to take a large integer and find its prime factors. The time it takes any classical computer to solve this problem grows exponentially with the number of digits. By making the integer large enough, it becomes essentially impossible for any classical computer to find the

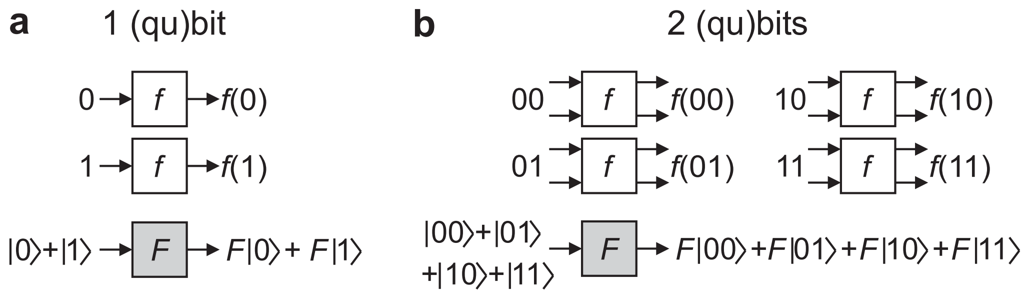

Figure 1.1: Difference between a classical and a quantum computer. **(a)** To determine the function f for the two possible input states 0 and 1, a one-bit classical computer needs to evaluate the function twice, once for every input state. In contrast, a one-qubit quantum computer can have a superposition of $|0\rangle$ and $|1\rangle$ as an input, to end up in a superposition of the two output values, $F|0\rangle$ and $F|1\rangle$. It has taken only half the number of steps as its classical counterpart. **(b)** Similarly, a two-qubit quantum computer needs only a quarter of the number of steps that are required classically. The computing power of a quantum computer scales exponentially with the number of qubits, for a classical computer the scaling is only linear.

answer within a reasonable time – such as the lifetime of the universe. This fact is used in most forms of cryptography nowadays [5].

In 1982, Richard Feynman speculated [6] that efficient algorithms to solve such hard computational problems might be found by making use of the unique features of quantum systems, such as entanglement. He envisioned a set of quantum two-level systems that are quantum mechanically coupled to each other, allowing the system as a whole to be brought into a superposition of different states. By controlling the Hamiltonian of the system and therefore its time-evolution, a computation might be performed in fewer steps than is possible classically. Essentially, such a quantum computer could take many computational steps at once; this is known as ‘quantum parallelism’.

A simplified view of the difference between a classical and a quantum computer is shown in Fig. 1.1. A one-bit classical computer is a machine that takes one input value, 0 or 1, and computes the corresponding output value, $f(0)$ or $f(1)$. A quantum computer with one quantum bit (or ‘qubit’) could take as an input value a superposition of $|0\rangle$ and $|1\rangle$, and due to the linearity of quantum mechanics the output would be a superposition of $F|0\rangle$ and $F|1\rangle$. So, in a sense it has performed two calculations in a single step. For a two-qubit system, the gain becomes even more significant: now the input can be a superposition of four states, so the quantum computer can perform four calculations in one step. In fact, it can be proved [7] that the computing power of a quantum computer scales exponentially with the number of qubits, whereas this scaling is only linear for a classical computer. Therefore, a large enough quantum computer can outperform any classical computer.

It might appear that a fundamental problem has been overlooked: according to quantum mechanics, a superposition of possible measurement outcomes can only exist before it is measured, and the measurement gives only one actual outcome. The exponential computing power thus appears inaccessible. However, by using carefully tailored quantum algorithms, an exponential speed-up can be achieved for some problems such as factoring integers [8] or simulating a quantum system [9]. For other tasks, such as searching a database, a quadratic speed-up is possible [10]. Using such quantum algorithms, a quantum computer can indeed be faster than a classical one.

Another fundamental problem is the interaction of the quantum system with the (uncontrolled) environment, which inevitably disturbs the desired quantum evolution. This process, known as 'decoherence', results in errors in the computation. Additional errors are introduced by imperfections in the quantum operations that are applied. All these errors propagate, and after some time the state of the computer will be significantly different from what it should be. It would seem that this prohibits any long computations, making it impossible for a quantum computer to use its exponential power for a non-trivial task. Fortunately, it has been shown that methods to detect and correct any errors exist [11, 12], keeping the computation on track. Of course, such methods only help if the error rate is small enough, since otherwise the correction operations create more errors than they remove. This sets a so-called 'accuracy threshold' [13, 14], which is currently believed to be around 10^{-4}. If the error per quantum operation is smaller than this threshold, any errors can be corrected and an arbitrarily long computation is possible.

Due to the development of quantum algorithms and error correction, quantum computation is feasible from a theoretical point of view. The challenge is building an actual quantum computer with a sufficiently large number of coupled qubits. Probably, more than a hundred qubits will be required for useful computations, but a system of about thirty qubits might already be able to perform valuable simulations of quantum systems.

1.2 Implementations

A number of features are required for building an actual quantum computer [16]:

1. A scalable physical system with well-characterized qubits
2. A 'universal' set of quantum gates to implement any algorithm

3. The ability to initialize the qubits to a known pure state
4. A qubit-specific measurement capability
5. Decoherence times much longer than the gate operation time

Many systems can be found which satisfy some of these criteria, but it is very hard to find a system that satisfies all of them. Essentially, we have to reconcile the conflicting demands of good access to the quantum system (in order to perform fast and reliable operations or measurements) with sufficient isolation from the environment (for long coherence times). Current state-of-the-art is a seven-bit quantum computer that has factored the number 15 into its prime factors 3 and 5, in fewer steps than is possible classically [15]. This was done using an ensemble of molecules in liquid solution, with seven nuclear spins in each molecule acting as the seven qubits. These could be controlled and read out using nuclear magnetic resonance (NMR) techniques. Although this experiment constitutes an important proof-of-principle for quantum computing, practical limitations do not allow the NMR approach to be scaled up to more than about ten qubits.

Therefore, many other implementations are currently being studied [17]. For instance, trapped ions have been used to demonstrate a universal set of one- and two-qubit operations, an elementary quantum algorithm, as well as entanglement of up to three qubits and quantum teleportation [17]. Typically, microscopic systems such as atoms or ions have excellent coherence properties, but are not easily accessible or scalable – on the other hand, larger systems such as solid-state devices, which can be accessed and scaled more easily, usually lack long decoherence times. A solid-state device with a long decoherence time would represent the best of both worlds. Such a system could be provided by the spin of an electron trapped in a quantum dot: a *spin qubit*.

1.3 The spin qubit

Our programme to build a solid-state qubit follows the proposal by Loss and DiVincenzo [18]. This describes a quantum two-level system defined by the spin orientation of a single electron trapped in a semiconductor quantum dot. The electron spin can point ‘up’ or ‘down’ with respect to an external magnetic field. These eigenstates, $|\uparrow\rangle$ and $|\downarrow\rangle$, correspond to the two basis states of the qubit.

The quantum dot that holds the electron spin is defined by applying negative voltages to metal surface electrodes (‘gates’) on top of a semiconductor (GaAs/AlGaAs) heterostructure (see Fig. 1.2). Such gated quantum dots are very controllable and versatile systems, which can be manipulated and probed

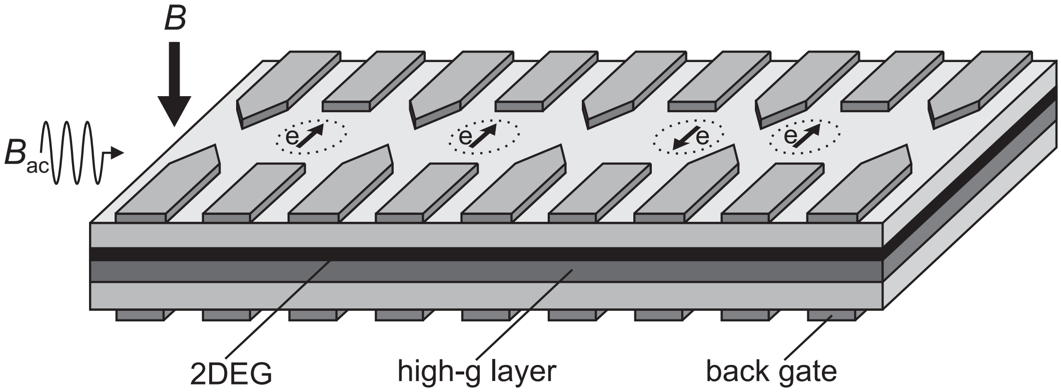

Figure 1.2: Schematic picture of the spin qubit as proposed by Loss and DiVincenzo [18]. The array of metal electrodes on top of a semiconductor heterostructure, containing a two-dimensional electron gas (2DEG) below the surface, defines a number of quantum dots (dotted circles), each holding a single electron spin (arrow). A magnetic field, B, induces a Zeeman splitting between the spin-up and spin-down states of each electron spin. The spin state is controlled either via an oscillating magnetic field, B_{ac} (on resonance with the Zeeman splitting), or via an oscillating electric field created with the back gates, which can pull the electron wavefunction into a layer with a large g-factor. Coupling between two spins is controlled by changing the voltage on the electrodes between the two dots. (Adapted from Ref. [18].)

electrically. Increasing the number of dots is straightforward, by simply adding more electrodes. Tuning all these gate voltages allows control of the number of electrons trapped on each dot, as well as the tunnel coupling between the dots. With the external magnetic field, B, we can tune the Zeeman splitting, $\Delta E_Z = g\mu_B B$, where $g \approx -0.44$ is the g-factor of GaAs, and $\mu_B = 9.27 \times 10^{-24}$ J/T is the Bohr magneton. In this way, we can control the energy levels of the qubit.

To perform single-qubit operations, different techniques are available. We can apply a microwave magnetic field on resonance with the Zeeman splitting, i.e. with a frequency $f = \Delta E_Z/h$, where h is Planck's constant. The oscillating magnetic component perpendicular to the static magnetic field B results in a spin nutation. By applying the oscillating field for a fixed duration, a superposition of $|\uparrow\rangle$ and $|\downarrow\rangle$ can be created. This magnetic technique is known as electron spin resonance (ESR).

A completely electrical alternative might be the emerging technique of g-tensor modulation [19]. In this scheme, an oscillating electric field is created by modulating the voltage applied to a (back) gate. The electric field does not couple to the spin directly, but it can push or pull the electron wavefunction somewhat into another semiconductor layer with a different g-factor. This procedure modulates the effective g-tensor felt by the electron spin. If the modulation frequency is resonant with the Zeeman splitting, the required spin nutation results and superpositions of spin states can again be created.

Two-qubit operations can be carried out purely electrically, by varying the gate voltages that control the potential barrier between two dots. It has been shown [18] that the system of two electron spins on neighboring dots, coupled via a tunnel barrier, can be mapped onto the Heisenberg exchange Hamiltonian $H = J\vec{S_1} \cdot \vec{S_2}$. This Hamiltonian describes an indirect interaction between the two spins, $\vec{S_1}$ and $\vec{S_2}$, mediated by the exchange interaction, J, which depends on the wavefunction overlap of the electrons. By lowering the tunnel barrier for some time and then raising it again, the effective spin-spin interaction is temporarily turned on. In this way, the two electron spins can be swapped or even entangled. Together with arbitrary single-spin rotations, the exchange interaction can be used to construct a universal set of quantum gates [18].

A last crucial ingredient is a method to read out the state of the spin qubit. This implies measuring the spin orientation of a single electron – a daunting task, since the electron spin magnetic moment is exceedingly small. Therefore, an indirect spin measurement is proposed [18]. First the spin orientation of the electron is correlated with its position, via 'spin-to-charge conversion'. Then an electrometer is used to measure the position of the charge, thereby revealing its spin. In this way, the problem of measuring the spin orientation has been replaced by the much easier measurement of charge.

The essential advantage of using the electron's spin degree of freedom to encode a qubit, lies in the fact that the spin is disturbed only weakly by the environment. The main source of spin decoherence and relaxation is predicted to be the phonon bath, which is coupled to the spin via the (weak) spin-orbit interaction [20, 21, 22]. In addition, fluctuations in the nuclear-spin configuration couple to the electron spin via the (even weaker) hyperfine coupling [20, 23]. In contrast, the electron's charge degree of freedom is much easier to manipulate and read out, but it is coupled via the strong Coulomb interaction to charge fluctuations, which are the source of the ubiquitous $1/f$ noise in the 'dirty' semiconductor environment. This leads to typical charge decoherence times of a few nanoseconds [24, 25]. The spin decoherence and relaxation times are predicted to be about four orders of magnitude longer [21].

Finally, it should be stressed that our efforts to create a spin qubit are not purely application-driven. Aside from the search for a spin quantum computer, many interesting questions await exploration. If we have the ability to (coherently) control and read out a single electron spin in a quantum dot, this spin

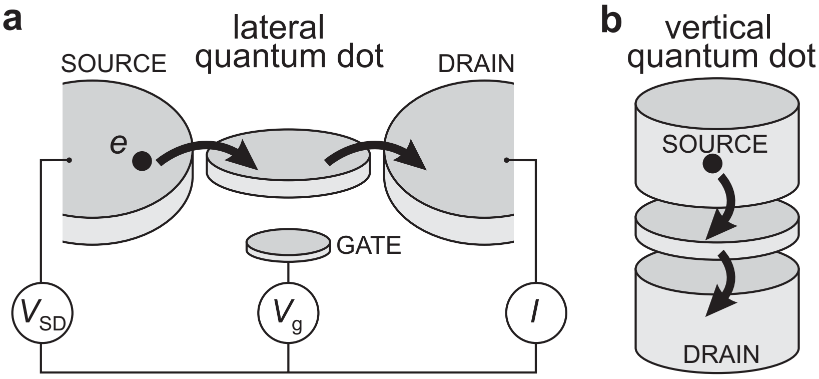

Figure 1.3: Schematic picture of a quantum dot in a lateral **(a)** and a vertical **(b)** geometry. The quantum dot (represented by a disk) is connected to source and drain contacts via tunnel barriers, allowing the current through the device, I, to be measured in response to a bias voltage, V_{SD} and a gate voltage, V_g.

could be used as a local probe of the semiconductor environment. This could shed light for instance on many details of the spin-orbit interaction or the hyperfine coupling.

1.4 Quantum dots

In this paragraph, the properties of semiconductor quantum dots are described in more detail [26]. In essence, a quantum dot is simply a small box that can be filled with electrons. The box is coupled via tunnel barriers to a source and drain reservoir, with which particles can be exchanged (see Fig. 1.3). By attaching current and voltage probes to these reservoirs, we can measure the electronic properties of the dot. The box is also coupled capacitively to one or more ‘gate’ electrodes, which can be used to tune the electrostatic potential of the dot with respect to the reservoirs. When the size of the box is comparable to the wavelength of the electrons that occupy it, the system exhibits a discrete energy spectrum, resembling that of an atom. As a result, quantum dots behave in many ways as *artificial atoms*.

Because a quantum dot is such a general kind of system, there exist quantum dots of many different sizes and materials: for instance single molecules trapped between electrodes, metallic or superconducting nanoparticles, self-assembled quantum dots, semiconductor lateral or vertical dots, and even semiconducting nanowires or carbon nanotubes between closely spaced electrodes. In this thesis, we focus on lateral (gated) semiconductor quantum dots (except in chapters 8 and 9, where vertical dots are used). These lateral devices allow all relevant

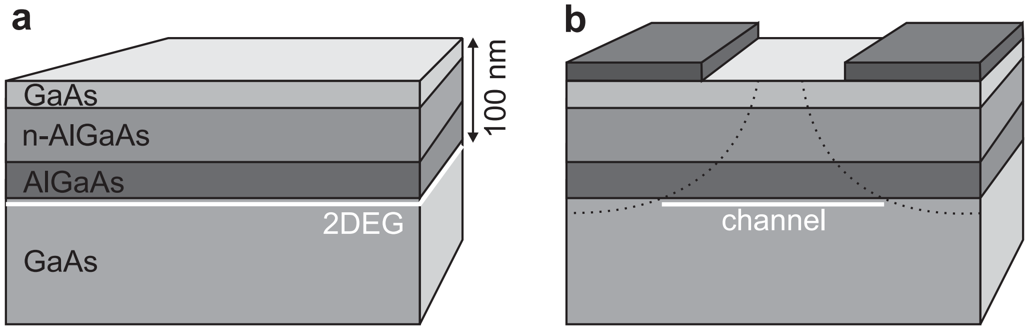

Figure 1.4: Confining electrons in a semiconductor. **(a)** Semiconductor heterostructure containing a 2DEG (indicated in white) approximately 100 nm below the surface, at the interface between GaAs and AlGaAs. The electrons in the 2DEG result from Si donors in the n-AlGaAs layer. (The thickness of the different layers is not to scale.) **(b)** By applying negative voltages to the metal electrodes on the surface of the heterostructure, the underlying 2DEG can be locally depleted. In this way, electrons can be confined to one or even zero dimensions.

parameters to be controlled in the fabrication process, or tuned *in situ*.

Fabrication of gated quantum dots starts with a semiconductor heterostructure, a sandwich of different layers of semiconducting material (see Fig. 1.4a). These layers, in our case GaAs and AlGaAs, are grown on top of each other using molecular beam epitaxy (MBE), resulting in very clean crystals. By doping the n-AlGaAs layer with Si, free electrons are introduced. These accumulate at the interface between GaAs and AlGaAs, typically 100 nm below the surface, forming a two-dimensional electron gas (2DEG) – a thin (10 nm) sheet of electrons that can only move along the interface. The 2DEG can have a high mobility and relatively low electron density (typically $10^5 - 10^6$ cm^2/Vs and $\sim 3 \times 10^{15}$ m^{-2}, respectively). The low electron density results in a large Fermi wavelength ($\sim$ 40 nm) and a large screening length, which allows us to locally deplete the 2DEG with an electric field. This electric field is created by applying (negative) voltages to metal gate electrodes on top of the heterostructure (Fig. 1.4b).

To fabricate these electrodes, we first spin a layer of organic resists (typically poly-methyl-methacrylate, PMMA) on the heterostructure surface (Fig. 1.5a). Then the gate pattern is defined by writing with a focused electron beam in the electron-sensitive resist. This locally breaks up the polymer chains, so that the exposed parts can be removed by a developer. (Note that there is some undercut of the bottom resist layer, caused by electrons backscattering from the heterostructure during exposure to the electron beam.) In the next step, metal is evaporated, which only makes contact to the heterostructure at the places where the resist has been exposed and removed. In our devices, the metal gates consist

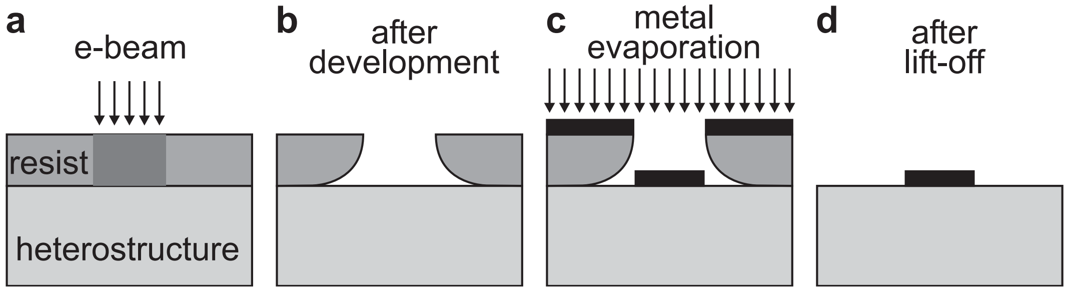

Figure 1.5: Fabrication of metal electrodes on the surface of the heterostructure. **(a)** Writing a pattern in the resist layer with an electron beam. **(b)** After developing, the resist has been locally removed. **(c)** Evaporating metal. **(d)** After lift-off, a metal electrode remains.

of a thin (5 nm) 'sticking' layer of titanium, with a 30 nm layer of gold on top. In the final so-called 'lift-off' step, the remaining resist is removed with acetone. Now metal electrodes are left at the places that were exposed to the electron beam.

The electron beam can accurately write very small patterns with a resolution of about 20 nm, allowing us to make very complicated gate structures (Fig. 1.6). By applying negative voltages to the gates, the 2DEG is locally depleted, creating one or more small islands that are isolated from the large 2DEG reservoirs. These islands are the quantum dots. In order to probe them, we need to make electrical contact to the reservoirs. For this, we use rapid thermal annealing to diffuse AuGeNi from the surface to the 2DEG below. This forms ohmic contacts that connect the 2DEG source and drain reservoirs electrically to metal bonding pads on the surface. Metal wires bonded to these pads run toward the current or voltage probes, enabling us to perform transport measurements.

1.5 Transport though quantum dots

We use two different ways to probe the behavior of electrons on a quantum dot. In the first part of the thesis (chapters 2 to 6) we mostly rely on a nearby quantum point contact (QPC) to detect changes in the number of electrons on the dot. In the second part (chapters 7 to 9) we perform conventional transport experiments. These experiments are conveniently understood using the constant interaction (CI) model [26]. This model makes two important assumptions. First, the Coulomb interactions among electrons in the dot are captured by a single constant capacitance, C. This is the total capacitance to the outside world, i.e. $C = C_S + C_D + C_g$, where C_S is the capacitance to the source, C_D that to the

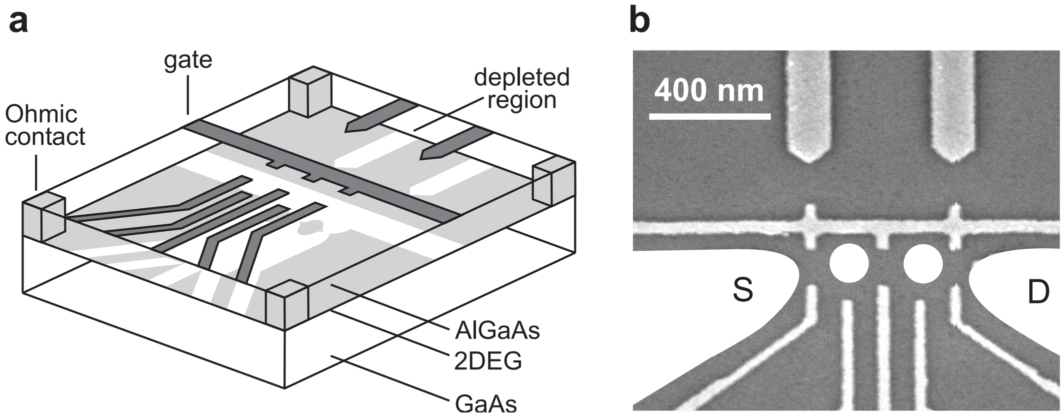

Figure 1.6: Lateral quantum dot device defined by metal surface electrodes. **(a)** Schematic view of a device. Negative voltages applied to metal gate electrodes (dark gray) lead to depleted regions (white) in the 2DEG (light gray). Ohmic contacts (light gray columns) enable bonding wires (not shown) to make electrical contact to the 2DEG reservoirs. **(b)** Scanning electron microscope image of an actual device, showing the gate electrodes (light gray) on top of the surface (dark gray). The two white dots indicate two quantum dots, connected via tunable tunnel barriers to a source (S) and drain (D) reservoir, indicated in white. The two upper gates can be used to create two quantum point contacts, in order to detect changes in the number of electrons on the dot (see chapters 2 to 6).

drain, and C_g to the gate. Second, the discrete energy spectrum is independent of the number of electrons on the dot. Under these assumptions the total energy of a N-electron dot with the source-drain voltage, V_{SD}, applied to the source (and the drain grounded), is given by

$$U(N) = \frac{[-|e|(N-N_0) + C_S V_{SD} + C_g V_g]^2}{2C} + \sum_{n=1}^{N} E_n(B) \tag{1.1}$$

where $-|e|$ is the electron charge and N_0 the number of electrons in the dot at zero gate voltage, which compensates the positive background charge originating from the donors in the heterostructure. The terms $C_S V_{SD}$ and $C_g V_g$ can change continuously and represent the charge on the dot that is induced by the bias voltage (through the capacitance C_S) and by the gate voltage V_g (through the capacitance C_g), respectively. The last term of Eq. 1.1 is a sum over the occupied single-particle energy levels $E_n(B)$, which are separated by an energy $\Delta E_n = E_n - E_{n-1}$. These energy levels depend on the characteristics of the confinement potential. Note that, within the CI model, only these single-particle states depend on magnetic field, B.

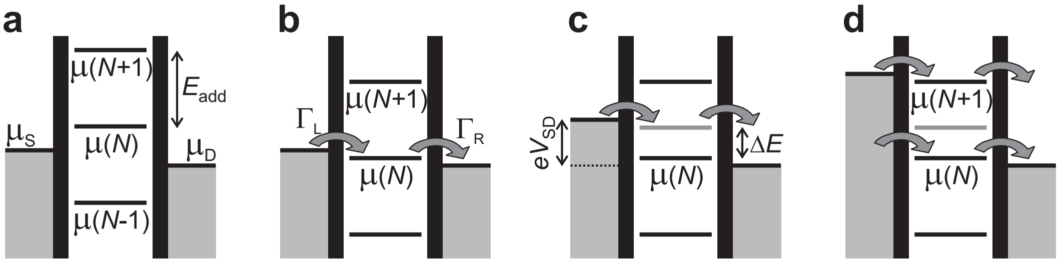

Figure 1.7: Schematic diagrams of the electrochemical potential of the quantum dot for different electron numbers. **(a)** No level falls within the bias window between μ_S and μ_D, so the electron number is fixed at $N-1$ due to Coulomb blockade. **(b)** The $\mu(N)$ level is aligned, so the number of electrons can alternate between N and $N-1$, resulting in a single-electron tunneling current. The magnitude of the current depends on the tunnel rate between the dot and the reservoir on the left, Γ_L, and on the right, Γ_R. **(c)** Both the ground-state transition between $N-1$ and N electrons (black line), as well as the transition to an N-electron excited state (gray line) fall within the bias window and can thus be used for transport (though not at the same time, due to Coulomb blockade). This results in a current that is different from the situation in (b). **(d)** The bias window is so large that the number of electrons can alternate between $N-1$, N and $N+1$, i.e. two electrons can tunnel onto the dot at the same time.

To describe transport experiments, it is often more convenient to use the electrochemical potential. This is defined as the energy required to add an electron to the quantum dot:

$$\begin{aligned}\mu(N) &\equiv U(N) - U(N-1) = \\ &= (N - N_0 - \frac{1}{2})E_C - \frac{E_C}{|e|}(C_S V_{SD} + C_g V_g) + E_N \qquad (1.2)\end{aligned}$$

where $E_C = e^2/C$ is the charging energy. The electrochemical potential for different electron numbers N is shown in Fig. 1.7a. The discrete levels are spaced by the so-called addition energy:

$$E_{add}(N) = \mu(N+1) - \mu(N) = E_C + \Delta E. \qquad (1.3)$$

The addition energy consists of a purely electrostatic part, the charging energy E_C, plus the energy spacing between two discrete quantum levels, ΔE. Note that ΔE can be zero, when two consecutive electrons are added to the same spin-degenerate level.

Of course, for transport to occur, energy conservation needs to be satisfied. This is the case when an electrochemical potential level falls within the 'bias window' between the electrochemical potential (Fermi energy) of the source (μ_S) and the drain (μ_D), i.e. $\mu_S \geq \mu \geq \mu_D$ with $-|e|V_{SD} = \mu_S - \mu_D$. Only then can an electron tunnel from the source onto the dot, and then tunnel off to the drain without losing or gaining energy. The important point to realize is that since the dot is very small, it has a very small capacitance and therefore a large charging energy – for typical dots $E_C \approx$ a few meV. If the electrochemical potential levels are as shown in Fig. 1.7a, this energy is not available (at low temperatures and small bias voltage). So, the number of electrons on the dot remains fixed and no current flows through the dot. This is known as Coulomb blockade.

Fortunately, there are many ways to lift the Coulomb blockade. First, we can change the voltage applied to the gate electrode. This changes the electrostatic potential of the dot with respect to that of the reservoirs, shifting the whole 'ladder' of electrochemical potential levels up or down. When a level falls within the bias window, the current through the device is switched on. In Fig. 1.7b $\mu(N)$ is aligned, so the electron number alternates between $N-1$ and N. This means that the Nth electron can tunnel onto the dot from the source, but only after it tunnels off to the drain can another electron come onto the dot again from the source. This cycle is known as single-electron tunneling.

By sweeping the gate voltage and measuring the current, we obtain a trace as shown in Fig. 1.8a. At the positions of the peaks, an electrochemical potential level is aligned with the source and drain and a single-electron tunneling current flows. In the valleys between the peaks, the number of electrons on the dot is fixed due to Coulomb blockade. By tuning the gate voltage from one valley to

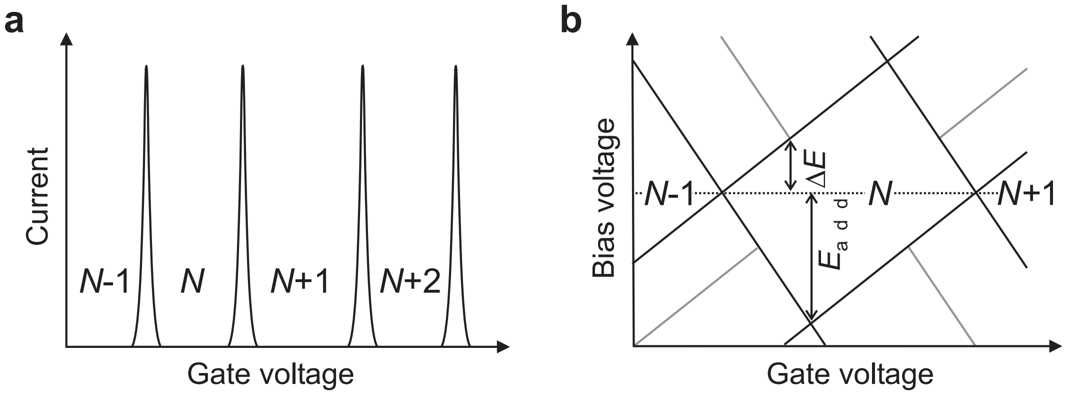

Figure 1.8: Transport through a quantum dot. **(a)** Coulomb peaks in current versus gate voltage in the linear-response regime. **(b)** Coulomb diamonds in differential conductance, dI/dV_{SD}, versus V_{SD} and V_g, up to large bias. The edges of the diamond-shaped regions (black) correspond to the onset of current. Diagonal lines emanating from the diamonds (gray) indicate the onset of transport through excited states.

the next one, the number of electrons on the dot can be precisely controlled. The distance between the peaks corresponds to $E_C + \Delta E$, and can therefore give information about the energy spectrum of the dot.

A second way to lift Coulomb blockade is by changing the source-drain voltage, V_{SD} (see Fig. 1.7c). (In general, we keep the drain potential fixed, and change only the source potential.) This increases the bias window and also 'drags' the electrochemical potential of the dot along, due to the capacitive coupling to the source. Again, a current can flow only when an electrochemical potential level falls within the bias window. By increasing V_{SD} until both the ground state as well as an excited state transition fall within the bias window, an electron can choose to tunnel not only through the ground state, but also through an excited state of the N-electron dot. This is visible as a change in the total current. In this way, we can perform excited-state spectroscopy.

Usually, we measure the current or differential conductance while sweeping the bias voltage, for a series of different values of the gate voltage. Such a measurement is shown schematically in Fig. 1.8b. Inside the diamond-shaped region, the number of electrons is fixed due to Coulomb blockade, and no current flows. Outside the diamonds, Coulomb blockade is lifted and single-electron tunneling can take place (or for larger bias voltages even double-electron tunneling is possible, see Fig. 1.7d). Excited states are revealed as changes in the current, i.e. as peaks or dips in the differential conductance. From such a 'Coulomb diamond' the excited-state splitting as well as the charging energy can be read off directly.

The simple model described above explains successfully how quantisation of charge and energy leads to effects like Coulomb blockade and Coulomb oscillations. Nevertheless, it is too simplified in many respects. For instance, the model considers only first-order tunneling processes, in which an electron tunnels first from one reservoir onto the dot, and then from the dot to the other reservoir. But when the tunnel rate between the dot and the leads, Γ, is increased, higher-order tunneling via virtual intermediate states becomes important. Such processes, which are known as 'cotunneling', are investigated in chapter 9. Furthermore, the simple model does not take into account the spin of the electrons, thereby excluding for instance exchange effects. Also the Kondo effect, an interaction between the spin on the dot and the spins of the electrons in the reservoir, cannot be accounted for. The Kondo effect is explored in chapters 7 and 8.

1.6 Spin configurations in few-electron quantum dots

The fact that electrons carry spin determines the electronic states of the quantum dot. In the simplest case – a dot containing just a single electron – spin leads to a splitting of all orbitals into Zeeman doublets, with the ground state corresponding to the electron spin pointing up (↑), and the excited state to the spin pointing down (↓). The difference between the corresponding energy levels $E_\uparrow$ and $E_\downarrow$ is given by the Zeeman energy, $\Delta E_Z = g\mu_B B$, which is approximately 25 μeV/T in GaAs.

For two electrons in a quantum dot, the situation is more complicated. For a Hamiltonian without explicit spin-dependent terms, the two-electron state is the product of the orbital and spin state. Since electrons are fermions, the total two-electron state has to be anti-symmetric under exchange of the two particles. Therefore, if the orbital part is symmetric, the spin state must be anti-symmetric, and if the spin part is anti-symmetric, the orbital state must be symmetric. The anti-symmetric two-spin state is the so-called spin singlet (S):

$$S = \frac{|\uparrow\downarrow\rangle - |\downarrow\uparrow\rangle}{\sqrt{2}} \tag{1.4}$$

which has total spin $S = 0$. The symmetric two-spin states are the so-called spin triplets (T_+, T_0 and T_-):

$$T_+ = |\uparrow\uparrow\rangle \qquad T_0 = \frac{|\uparrow\downarrow\rangle + |\downarrow\uparrow\rangle}{\sqrt{2}} \qquad T_- = |\downarrow\downarrow\rangle \tag{1.5}$$

which have total spin $S = 1$ and a quantum number m_s (corresponding to the spin z-component) of 1, 0, and -1, respectively. In a finite magnetic field, the three triplet states are split by the Zeeman splitting, ΔE_Z.

Even at zero magnetic field, the energy of the two-electron system depends on its spin configuration, through the requirement of anti-symmetry of the total state. If we consider just the two lowest orbitals, ε_0 and ε_1, then there are six possibilities to fill these with two electrons (Fig. 1.9). At zero magnetic field [27], the two-electron ground state is always the spin singlet (Fig. 1.9a), and the lowest excited states are always the three spin triplets (Fig. 1.9b–d). The energy gain of T_0 with respect to the excited spin singlet S_1 (Fig. 1.9e) is known as the exchange energy, J. It essentially results from the fact that electrons in the triplet states tend to avoid each other, reducing their mutual Coulomb energy. As the Coulomb interaction is very strong, the exchange energy can be quite large (a few 100 μeV) [28].

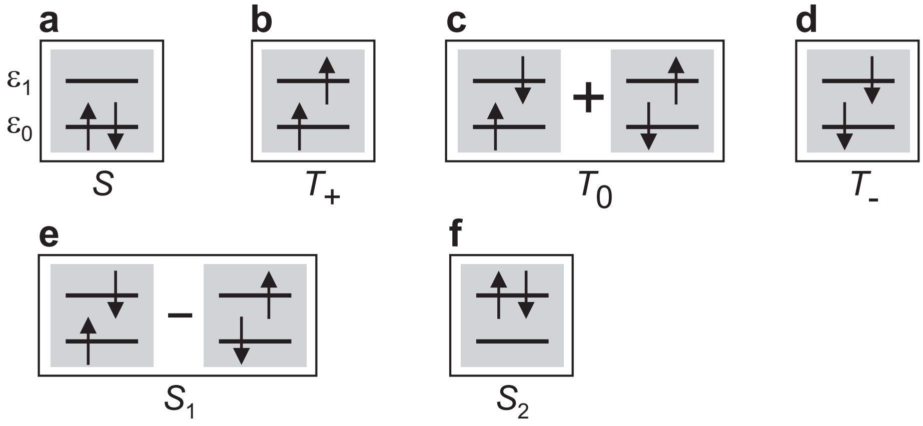

Figure 1.9: Schematic energy diagrams depicting the spin states of two electrons occupying two spin degenerate single-particle levels (ε_0 and ε_1). **(a)** Spin singlet, which is the ground state at zero magnetic field. **(b)–(d)** Lowest three spin triplet states, T_+, T_0 and T_-, which have total spin $S = 1$ and quantum number $m_s = +1$, 0 and -1, respectively. In finite magnetic field, the triplet states are split by the Zeeman energy. **(e)** Excited spin singlet state, S_1, which has an energy J compared to triplet state T_0. **(f)** Highest excited spin singlet state, S_2.

The energy difference between T_0 and the lowest singlet S, the 'singlet-triplet energy' E_{ST}, is thus considerably smaller than $\varepsilon_1 - \varepsilon_0$. In fact, besides the gain in exchange energy for the triplet states, there is also a gain in the direct Coulomb energy, related to the different occupation of the orbitals [28]. For a magnetic field above a few Tesla (perpendicular to the 2DEG plane), E_{ST} can even become negative, leading to a singlet-triplet transition of the two-electron ground state [29].

In the presence of a magnetic field, the energies of the lowest singlet and triplet states (Fig. 1.9a–d) can be expressed as:

$$\begin{aligned}
E_S &= E_\uparrow + E_\downarrow + E_C = 2E_\uparrow + \Delta E_Z + E_C \\
E_{T_+} &= 2E_\uparrow + E_{ST} + E_C \\
E_{T_0} &= E_\uparrow + E_\downarrow + E_{ST} + E_C = 2E_\uparrow + E_{ST} + \Delta E_Z + E_C \\
E_{T_-} &= 2E_\downarrow + E_{ST} + E_C = 2E_\uparrow + E_{ST} + 2\Delta E_Z + E_C.
\end{aligned}$$

Figure 1.10a shows the possible transitions between the one-electron spin-split orbital ground state and the two-electron states. We have omitted the transitions $\uparrow\leftrightarrow T_-$ and $\downarrow\leftrightarrow T_+$ since these require a change in the spin z-component of more than 1/2 and are thus spin-blocked [30]. From the energy diagram we can deduce the electrochemical potential ladder, which is shown in Fig. 1.10b. Note that $\mu_{\uparrow\leftrightarrow T_+} = \mu_{\downarrow\leftrightarrow T_0}$ and $\mu_{\uparrow\leftrightarrow T_0} = \mu_{\downarrow\leftrightarrow T_-}$. Consequently, the *three* triplet states lead to

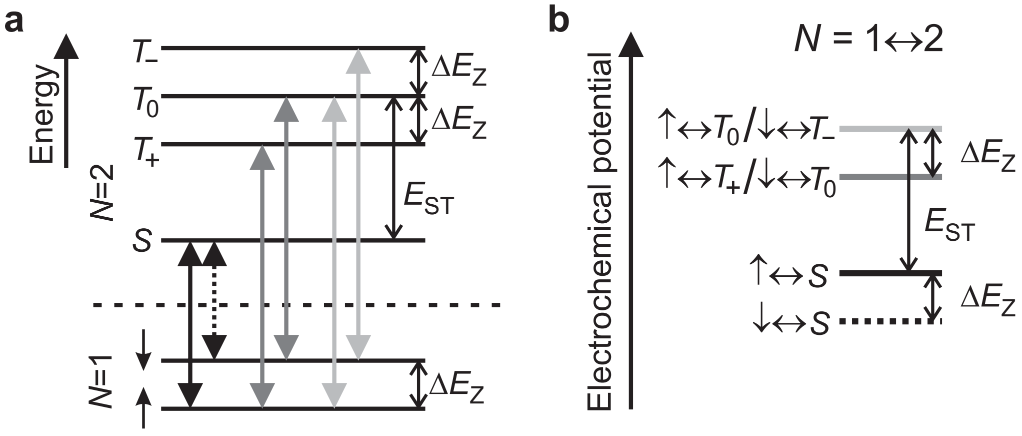
a
Energy
N=2
N=1
T_-
T_0
T_+
S
ΔE_Z
ΔE_Z
E_{ST}
ΔE_Z
b
Electrochemical potential
$N = 1 \leftrightarrow 2$
$\uparrow\leftrightarrow T_0/\downarrow\leftrightarrow T_-$
$\uparrow\leftrightarrow T_+/\downarrow\leftrightarrow T_0$
$\uparrow\leftrightarrow S$
$\downarrow\leftrightarrow S$
ΔE_Z
E_{ST}
ΔE_Z

Figure 1.10: One- and two-electron states and transitions at finite magnetic field. **(a)** Energy diagram for a fixed gate voltage. By changing the gate voltage, the one-electron states (below the dashed line) shift up or down relative to the two-electron states (above the dashed line). The six transitions that are allowed (i.e. not spin-blocked) are indicated by vertical arrows. **(b)** Electrochemical potentials for the transitions between one- and two-electron states. The six transitions in (a) correspond to only four different electrochemical potentials. By changing the gate voltage, the whole ladder of levels is shifted up or down.

only *two* resonances in first order transport through the dot.

For more than two electrons, the spin states can be much more complicated. However, in some cases and for certain magnetic field regimes they might be well approximated by a one-electron Zeeman doublet (when N is odd) or by two-electron singlet or triplet states (when N is even). But there are still differences – for instance, if $N > 2$ the ground state at zero field can be a spin triplet, due to Hund's rule [31].

The eigenstates of a two-electron double dot are also spin singlets and triplets. We can again use the diagrams in Fig. 1.9, but now the single-particle eigenstates ε_0 and ε_1 represent the symmetric and anti-symmetric combination of the lowest orbital on each of the two dots, respectively. Due to tunneling between the dots, with tunneling matrix element t, ε_0 (the 'bonding state') and ε_1 (the 'anti-bonding state') are split by an energy $2t$. By filling the two states with two electrons, we again get a spin singlet ground state and a triplet first excited state (at zero field). However, the singlet ground state is not purely S (Fig. 1.9a), but also contains a small admixture of the excited singlet S_2 (Fig. 1.9f). The admixture of S_2 depends on the competition between inter-dot tunneling and the Coulomb repulsion, and serves to lower the Coulomb energy by reducing the double occupancy of the dots [32].

If we focus only on the singlet ground state and the triplet first excited states, then we can describe the two spins $\vec{S_1}$ and $\vec{S_2}$ by the Heisenberg Hamiltonian, $H = J\vec{S_1} \cdot \vec{S_2}$. Due to this mapping procedure, J is now defined as the energy difference between the triplet state T_0 and the singlet ground state, which depends on the details of the double dot orbital states. From a Hund-Mulliken calculation [33], J is approximately given by $4t^2/U + V$, where U is the on-site charging energy and V includes the effect of the long-range Coulomb interaction. By changing the overlap of the wavefunctions of the two electrons, we can change t and therefore J. Thus, control of the inter-dot tunnel barrier would allow us to perform operations such as swapping or entangling two spins.

1.7 Kondo effect in quantum dots

The only transport mechanism we have described in section 2.5, was sequential tunneling. This first-order tunneling mechanism gives rise to a current only at the Coulomb peaks, with the number of electrons on the dot being fixed between the peaks. This description is quite accurate for a dot with very opaque tunnel barriers. However, when the dot is opened, so that the resistance of the tunnel barriers becomes comparable to the resistance quantum, $R_Q \equiv h/e^2 = 25.8$ kΩ, higher-order tunneling processes have to be taken into account. These lead to quantum fluctuations in the electron number, even when the dot is in the Coulomb blockade regime.

An example of such a higher-order tunneling event is shown in Fig. 1.11a. Energy conservation forbids the number of electrons to change, as this would cost an energy of order $E_C/2$. Nevertheless, an electron can tunnel off the dot, leaving it temporarily in a classically forbidden 'virtual' state (middle diagram in Fig. 1.11a). This is allowed by virtue of Heisenberg's energy-time uncertainty principle, as long as another electron tunnels back onto the dot immediately, so that the system returns the energy it borrowed. The final state then has the same energy as the initial one, but one electron has been transported through the dot. This process, also known as (elastic) 'cotunneling' [34], is studied in more detail in chapter 9.

If the electron spin is taken into account, then events such as shown in Fig. 1.11b can take place. Initially, the dot has a net spin up, but after the virtual intermediate state, the dot spin is flipped. Unexpectedly, it turns out that by adding many spin-flips events of higher orders coherently, the spin-flip rate diverges. The spin on the dot and the electron spins in the reservoirs are no longer separate, they have become *entangled*. The result is the appearance of a

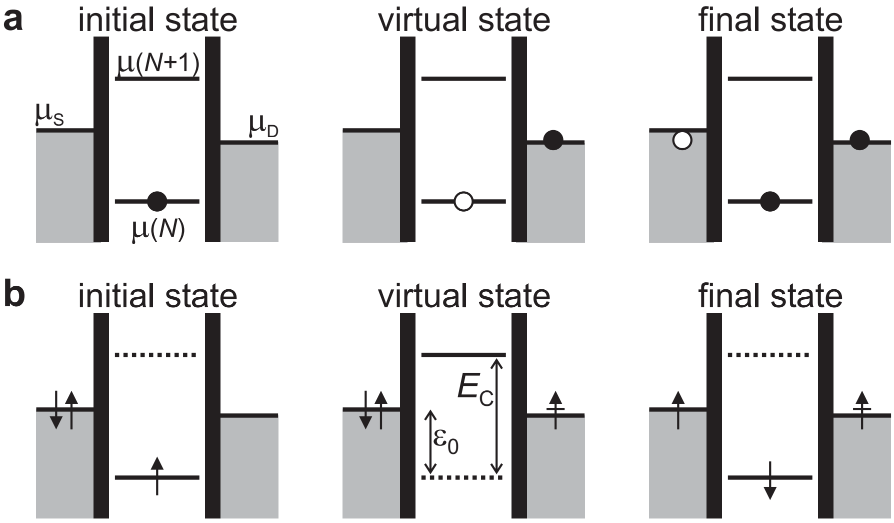

Figure 1.11: Higher-order tunneling events overcoming Coulomb blockade. **(a)** Elastic cotunneling. The Nth electron on the dot jumps to the drain to be immediately replaced by an electron from the source. Due to the small bias, such events give rise to a net current. **(b)** Spin-flip cotunneling. The spin-up electron jumps out of the dot to be immediately replaced by a spin-down electron. Many such higher-order spin-flip events together build up a spin singlet state consisting of electron spins in the reservoirs and the spin on the dot. Thus, the spin on the dot is screened.

new ground state of the system as a whole – a spin singlet. The spin on the dot is thus completely screened by the electron spins in the reservoirs.

This is completely analogous to the well-known Kondo effect, which occurs in metals containing a small concentration of magnetic impurities (e.g. cobalt). It was observed already in the 1930's [35] that below a certain temperature (typically about 10 K), the resistance of such metals would grow. This anomalous behavior was not understood, until in 1964 the Japanese theorist Jun Kondo explained it as screening of the impurity spins by the spins of the conduction electrons in the host metal [36]. The screening is accompanied by a scattering resonance at the Fermi energy of the metal, resulting in an increased resistance. In 1988, it was realized that the same Kondo effect should occur (at low temperatures) in quantum dots with a net spin [38, 39]. However, in quantum dots the scattering resonance is manifested as an increased probability for scattering from the source to the drain reservoir, i.e. as an increased conductance.

The Kondo effect appears below the so-called Kondo temperature, T_K, which corresponds to the binding energy of the Kondo singlet state. It can be expressed in terms of the dot parameters as

$$T_K = \frac{\sqrt{\Gamma E_C}}{2} e^{\pi\varepsilon_0(\varepsilon_0+E_C)/\Gamma E_C} \tag{1.6}$$

where Γ is the tunnel rate to and from the dot, and ε_0 is the energy level on the dot relative to the Fermi energy of the reservoirs. The great advantage of using quantum dots to study the Kondo effect, is that they allow these parameters to be tuned *in situ* [37]. In addition, the versatility of dots allows new and exotic regimes of the Kondo effect to be explored, as is demonstrated in chapter 8.

The main characteristics of the Kondo effect in transport through a quantum dot are schematically depicted in Fig. 1.12. For an odd number of electrons on the dot, the total spin S is necessarily non-zero, and in the simplest case $S = 1/2$. However, for an even electron number on the dot – again in the simplest scenario – all spins are paired, so that $S = 0$ and the Kondo effect is not expected to occur. This 'even-odd-asymmetry' results in the temperature dependence of the linear conductance, G, as shown in Fig. 1.12a. In the 'odd' or 'Kondo' valleys the conductance increases as the temperature is lowered, due to the Kondo effect. In the 'even' valleys, on the other hand, the conductance decreases, due to a decrease of thermally excited transport through the dot.

The temperature dependence of the conductance in the middle of the Kondo valleys is shown in Fig. 1.12b. The conductance increases logarithmically with decreasing temperature [38], and saturates at a value $2e^2/h$ at the lowest temperatures [39, 40]. Although the dot has two tunnel barriers and the charging energy

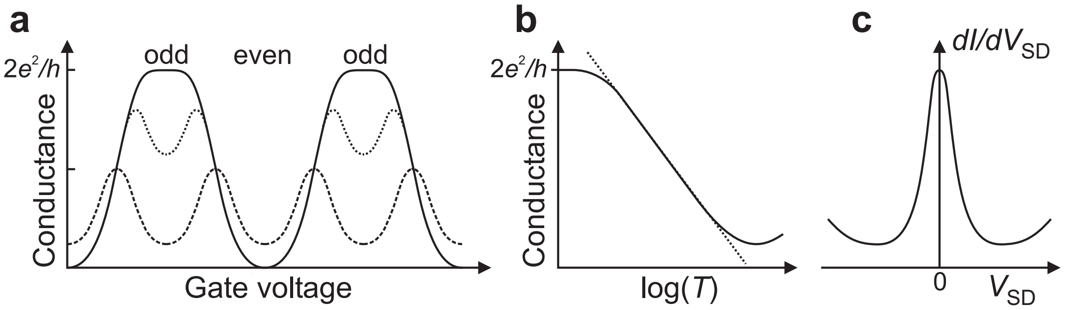

Figure 1.12: Schematic representation of the main characteristics of the Kondo effect in electron transport through a quantum dot. **(a)** Linear conductance versus gate voltage, for $T \ll T_K$ (solid line), $T \lesssim T_K$ (dotted line), and $T \gg T_K$ (dashed line). the Kondo effect only occurs for odd electron number, resulting in an odd-even asymmetry between the different Coulomb valleys. **(b)** In the odd ('Kondo') valleys the conductance increases logarithmically upon lowering the temperature, and saturates at $2e^2/h$. **(c)** The Kondo resonance leads to a zero-bias resonance in the differential conductance, dI/dV_{SD}, versus bias voltage, V_{SD}.

tends to block electrons from tunneling on or off, the Kondo effect enables electrons to pass unhindered through the dot. This complete transparency of the dot is known as the 'unitary limit' of conductance. The first experimental observation of this limit in quantum dots is reported in chapter 7. The Kondo resonance at the Fermi energy of the reservoirs is manifested as a zero-bias resonance in the differential conductance, dI/dV_{SD}, versus V_{SD}, as shown in Fig. 1.12c. The full width at half maximum of this resonance gives an estimate of the Kondo temperature.

1.8 Measurement setup

Dilution refrigerator

To resolve small energies such as the Zeeman splitting, the sample has to be cooled down to temperatures well below a Kelvin. We use an Oxford Kelvinox 300 dilution refrigerator, which has a base temperature of about 10 mK, and a cooling power in excess of 300 μW (at 100 mK). The sample holder is connected to a cold finger and placed in a copper can (36 mm inner diameter) in the bore of a superconducting magnet that can apply a magnetic field up to 16 T.

Measurement electronics

A typical measurement involves applying a source-drain voltage over (a part of) the device, and measuring the resulting current as a function of the voltages applied to the gates. The electrical circuits for the voltage-biased current measurement and for applying the gate voltages are shown in Fig. 1.13 and Fig. 1.14, respectively. The most important parts of the measurement electronics – i.e. the current-to-voltage (IV) convertor, isolation amplifier, voltage source and digital-to-analog convertors (DACs) – were all built by Raymond Schouten at Delft University. The underlying principle of the setup is to isolate the sample electrically from the measurement electronics. This is achieved via optical isolation at both sides of the measurement chain, i.e. in the voltage source, the isolation amplifier, as well as the DACs. In all these units, the electrical signal passes through analog optocouplers, which first convert it to an optical signal using an LED, and then convert the optical signal back using a photodiode. In this way, there is no galvanic connection between the two sides. In addition, all circuitry at the sample side is analog (even the DACs have no clock circuits or microprocessors), battery-powered, and uses a single clean ground (connected to the metal parts of the fridge) which is separated from the ground used by the 'dirty' electronics. All these features help to eliminate ground loops and reduce interference on the

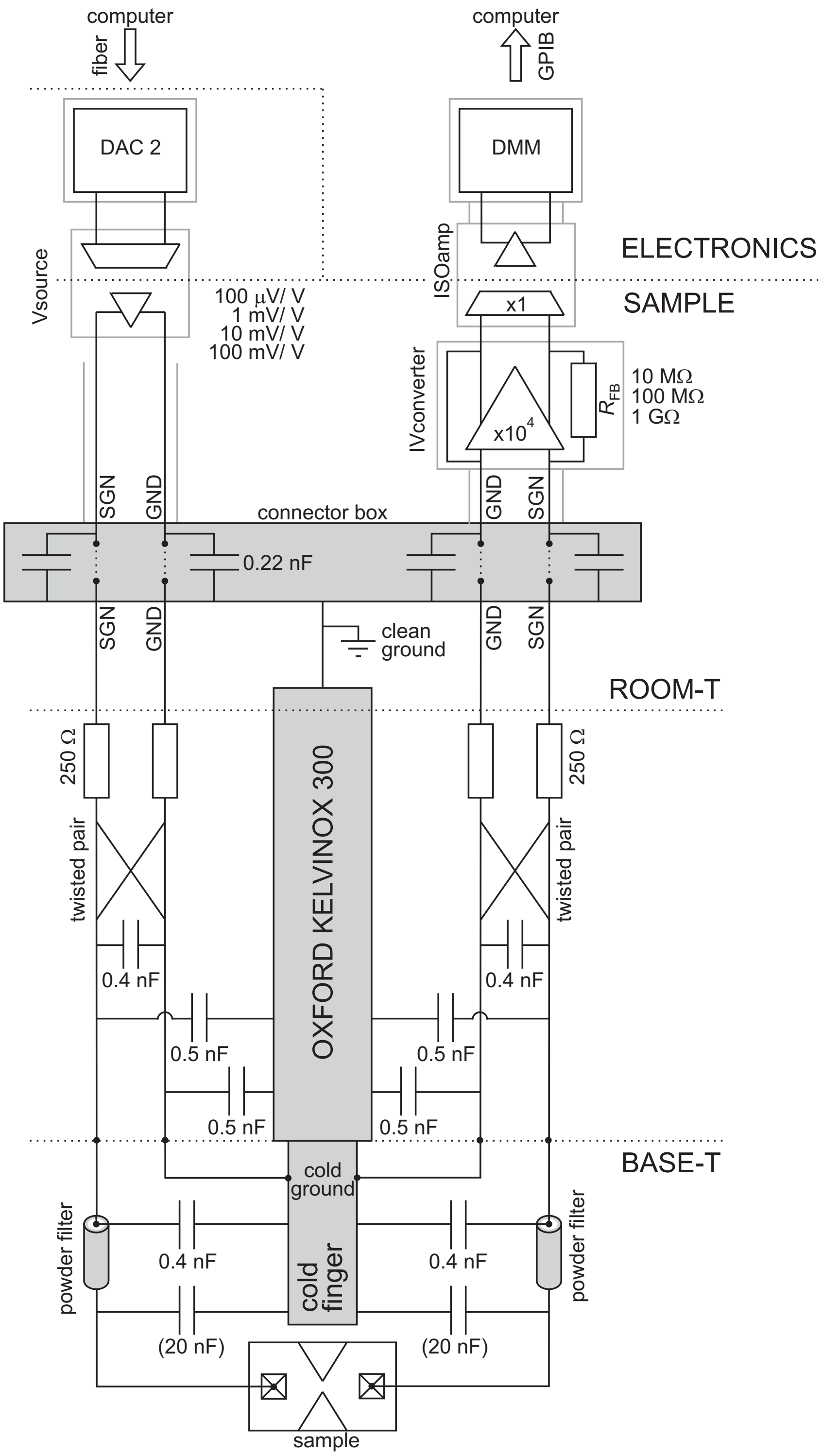
computer
fiber
computer
GPIB
DAC 2
DMM
ELECTRONICS
SAMPLE
Vsource
ISOamp
x1
100 µV/ V
1 mV/ V
10 mV/ V
100 mV/ V
IVconverter
x10^4
R_FB
10 MΩ
100 MΩ
1 GΩ
SGN
GND
GND
SGN
connector box
0.22 nF
clean ground
ROOM-T
250 Ω
250 Ω
twisted pair
twisted pair
OXFORD KELVINOX 300
0.4 nF
0.4 nF
0.5 nF
0.5 nF
0.5 nF
0.5 nF
BASE-T
cold ground
powder filter
powder filter
0.4 nF
0.4 nF
cold finger
(20 nF)
(20 nF)
sample

Figure 1.13: Electrical circuit for performing a voltage-biased current measurement. Elements shown in gray are connected to ground. Gray lines indicate the shielding of the measurement electronics and wires.

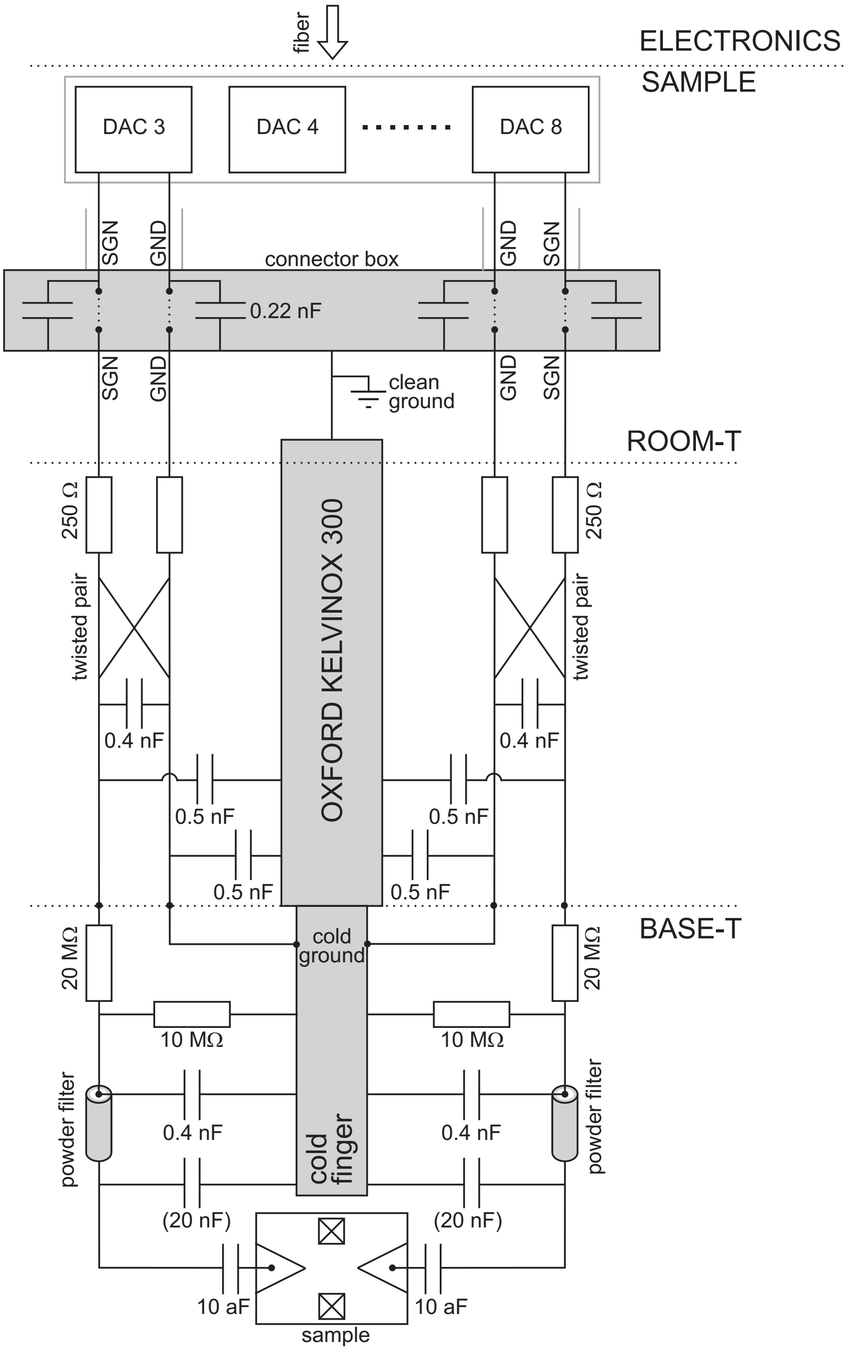
fiber
ELECTRONICS
SAMPLE
DAC 3
DAC 4
DAC 8
SGN
GND
GND
SGN
connector box
0.22 nF
SGN
GND
GND
SGN
clean ground
ROOM-T
OXFORD KELVINOX 300
250 Ω
250 Ω
twisted pair
twisted pair
0.4 nF
0.4 nF
0.5 nF
0.5 nF
0.5 nF
0.5 nF
BASE-T
cold ground
20 MΩ
20 MΩ
10 MΩ
10 MΩ
powder filter
powder filter
0.4 nF
0.4 nF
cold finger
(20 nF)
(20 nF)
10 aF
10 aF
sample

Figure 1.14: Electrical circuit for applying voltages to the gate electrodes. Elements shown in gray are connected to ground. Gray lines indicate the shielding of the measurement electronics and wires.

measurement signal.

Measurements are controlled by a computer running LabView. It sends commands via a fiber link to two DAC-boxes, each containing 8 digital-to-analog convertors, and powered by a specially shielded transformer. Most of the DACs are used to generate the voltages applied to the gate electrodes (typically between 0 and -5 V). One of the DACs controls the source-drain voltage for the device. The output voltage of this DAC (typically between +5 and -5V) is sent to a voltage source, which attenuates the signal by a factor 10, 10^2, 10^3 or 10^4 and provides optical isolation. The attenuated voltage is then applied to one of the ohmic contacts connected to the source reservoir of the device.

The resulting current coming from the drain reservoir is fed to a low-noise IV convertor. In this thesis we use two types, depending on the desired bandwidth. The first one (used in Chapters 2, 7, 8 and 9), is designed for low-frequency measurements. It has a bandwidth of about 1 kHz, and a noise floor of $\sim$ 5 fA/Hz$^{1/2}$. The feedback resistance can be set to 10 MΩ, 100 MΩ or 1GΩ, with an input resistance that is a factor 10^3 or 10^4 smaller (for the 'low noise' or 'low input resistance' setting, respectively). The faster IV convertor (used in Chapters 3, 4 and 5) has a bandwidth of about 150 kHz, and a current noise of $\sim$ 1 pA/Hz$^{1/2}$ at 100 kHz. The feedback resistance is 10 MΩ, corresponding to an input resistance of 1.3 kΩ. More characteristics are given in Chapter 4.

The signal from the IV convertor is then sent to an isolation amplifier, to provide optical isolation and possibly gain. Again we can choose a low-frequency version (up to $\sim$ 1 kHz) or a high-frequency one (up to $\sim$ 300 kHz). The voltage from the isolation amplifier is finally measured by a digital multimeter (Keithley 2700) and sent to the computer via GPIB interface. Alternatively, we can use a lock-in amplifier (Stanford EG&G 5210) if the signal to be measured is periodic, or an ADwin Gold module for very fast measurements (up to 2.2×10^6 14-bit samples per second).

Measurement wires

To make contact to the sample, 2 × 12 twisted pairs of wires run from two connector boxes at room temperature all the way down to the 'cold finger' at base temperature. The diameter and material of these wires is chosen to minimize the heat load on the mixing chamber. From room temperature to 1 Kelvin, 2 × 9 pairs consist of manganine wires (100 μm diameter), and 2 × 3 pairs of copper wires (90 μm diameter). The copper wires can be used if a large current has to be applied. From 1 Kelvin to the mixing chamber, superconducting 'Niomax' wires (50 μm diameter) are used. From the mixing chamber to the bottom of the cold finger, where thermal conductivity is no longer a constraint, we have standard copper wires. At base temperature, one wire of each twisted pair is connected to 'cold ground' (i.e. the cold finger), which is electrically connected to clean ground via the metal parts of the fridge.

All wires are thermally anchored to the fridge, by carefully wrapping them around copper posts, at several temperature stages (4 K, 1 K, $\sim$ 100 mK and $\sim$ 10 mK). At room temperature, the resistance of the wires is about 250 Ω or 150 Ω for the manganine or copper wires, respectively. At low temperature it is about 50 Ω. The wires have various parasitic capacitances to their twisted partner and to ground, as indicated in Fig. 1.13 and Fig. 1.14.

Filtering

The wires connect the device to the measurement electronics at room temperature, so they have to be carefully filtered to avoid that the electrons in the sample heat up due to spurious noise and interference. Several filtering stages are required for different frequency ranges (see Fig. 1.13 and Fig. 1.14). In the connector box at room temperature, all wires are connected to ground via 0.22 nF 'feedthrough capacitors'. At base temperature, all signal wires run through 'copper powder filters' [41]. These are copper tubes filled with copper powder, in which 4 signal wires with a length of about 2 meters each are wound. The powder absorbs the high-frequency noise very effectively, leading to an attenuation of more than -60 dB from a few 100 MHz up to more than 50 GHz [42].

To remove the remaining low-frequency noise, we solder a 20 nF capacitor between each signal wire and the cold finger ground. In combination with the $\sim$ 100 Ω resistance of the wires, this forms a low-pass RC filter with a cut-off frequency of about 100 kHz (even 10 kHz for the wire connected to the IV convertor, due to its input resistance of about 1.3 kΩ). These filters are used for the wires connecting to ohmic contacts (although they were taken out to perform some of the high-bandwidth measurements described in this thesis). For the wires connecting to gate electrodes, a 1:3 voltage divider is present (consisting of a 20 MΩ resistance in the signal line and a 10 MΩ resistance to ground). In this way, the gate voltages are filtered by a low-pass RC filter with a cut-off frequency of about 1 Hz. By combining all these filters, the electrons in the sample can be cooled to an effective temperature below 50 mK (if no extra heat loads such as coaxial cables are present).

High-frequency signals

High-frequency signals can be applied to gate electrodes via two coaxial cables. They consist of three parts, connected via standard 2.4 mm Hewlett Packard connectors (specified up to 50 GHz). From room temperature to 1 Kelvin, a 0.085

inch semi-rigid Be-Cu (inner and outer conductor) coaxial cable is used. From 1 Kelvin to the mixing chamber, we use 0.085 inch semi-rigid superconducting Nb. From the mixing chamber to the sample holder, flexible tin plated Cu coaxial cables are present. The coaxes are thermally anchored at 4 K, 1 K, $\sim$ 800 mK, $\sim$ 100 mK and base temperature, by clamping each cable firmly between two copper parts. To thermalize also the inner conductor of the coax, we use Hewlett Packard 8490D attenuators (typically -20 dB) at 1 K. These attenuators cannot be used at the mixing chamber, as they tend to become superconducting below about 100 mK. We have also tried using Inmet 50EH attenuators at the mixing chamber, but these showed the same problem.

To generate the high-frequency signals, we use a microwave source (Hewlett Packard 83650A) that goes up to 50 GHz (or 75 GHz, in combination with a 'frequency doubler'); a pulse generator (Hewlett Packard 8133A), which generates simple 10 ns to 1 μs pulses with a rise time of 60 ps; and an arbitrary waveform generator (Sony Tektronix AWS520), which can generate more complicated pulses with a rise time of 1.5 ns. With the cables described above, the fastest pulse flank we can transmit to the sample is about 200 ps. Microwave signals are transmitted with about 10 dB loss at 50 GHz.

Special care needs to be given to the connection from the coaxial cable to the chip, in order to minimize reflections. The sample holder we use, has an SMA connector that can be connected to the 2.4 mm coaxial cable. At the other end, the pin of the SMA connector sticks through a small hole in the chip carrier. This allows it to be soldered to a metal pad on the chip carrier, from which we can then bond to the chip. This sample holder is used to apply pulses or microwave signals to a gate electrode.

1.9 Sample stability

A severe experimental difficulty that is not related to the measurement setup, but to the sample itself, is the problem of 'charge switching'. It shows up in measurements as fluctuations in the position of a Coulomb peak, or as sudden jumps in the QPC-current that are not related to charging or discharging of a nearby quantum dot. Generally, these switches are attributed to (deep) traps in the donor layer that capture or release an electron close to the quantum dot [43]. This well-known but poorly understood phenomenon is a manifestation of 1/f noise in semiconductors, which causes the electrostatic potential landscape in the 2DEG to fluctuate.

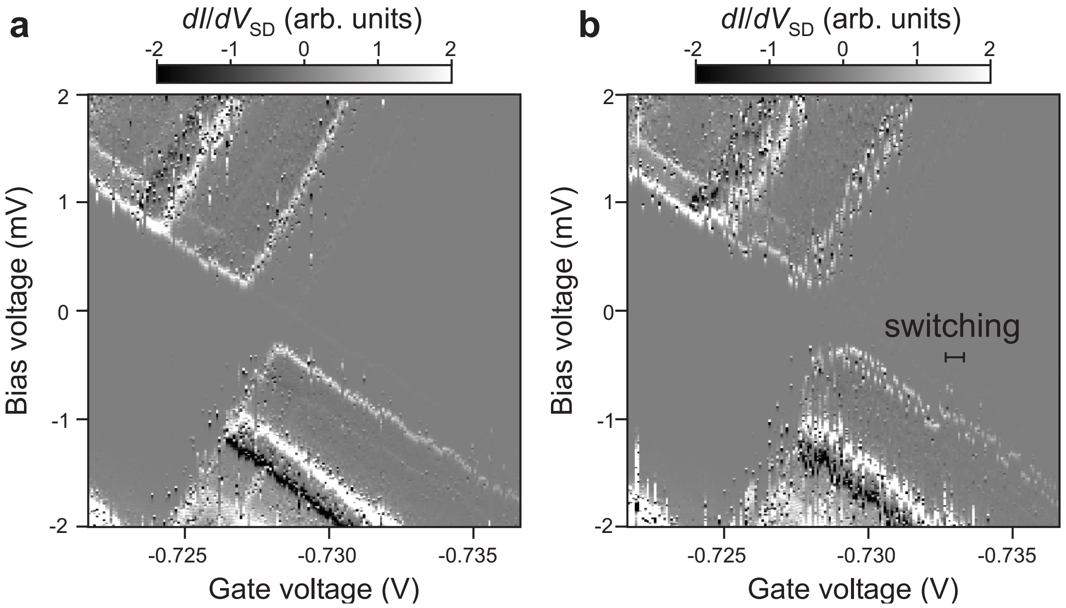

Figure 1.15: Charge switching in a large-bias measurement in the few-electron regime, for $B = 12$ T. **(a)** Differential conductance, dI/dV_{SD} (in grayscale), as a function of bias voltage and gate voltage. This measurement is considered reasonably stable. **(b)** Identical measurement, taken immediately after (a). A single two-level fluctuator has become active, causing the effective gate voltage to fluctuate between two values at any position in the figure, and leading to an apparent splitting of all the lines. This is considered a measurement of poor stability.

The strength of the fluctuations can differ enormously. In some samples, switching occurs on a time scale of seconds, making only the most trivial measurements possible, whereas in other samples, no switches are visible on a time scale of hours. It is not clear what exactly determines the stability. It certainly depends on the heterostructure, as some wafers are clearly better than others. A number of growth parameters could be important, such as the Al concentration in the AlGaAs, the doping density and method (modulation doping or delta doping), the thickness of the spacer layer between the n-AlGaAs and GaAs, the depth of the 2DEG below the surface, a possible surface layer, and many more. We have recently started a collaboration with the group of Professor Wegscheider in Regensburg to grow and characterize heterostructures in which some of these parameters are systematically varied. In this way we hope to find out what makes certain heterostructures stable.

Even for the same heterostructure, some samples are more quiet than others. The reasons for this are not clear. There are reports that stability is improved if the sample is cooled down slowly, while applying a positive voltage (about +280 mV) on all gates that are going to be used in the experiment. This procedure effectively 'freezes in' a negative charge around the gates, such that less negative gate voltages are sufficient to define the quantum dot at low temperatures. Most samples described in this thesis have been cooled down from room temperature to 4 K slowly (in one to two days) with all gates grounded. We find that in general samples get more quiet during the first week of applying the gate voltages. Finally, sample stability also involves an element of luck: Fig. 1.15 shows two Coulomb diamonds that were measured immediately after each other under identical conditions. Measurement Fig. 1.15a is reasonably quiet, but in Fig. 1.15b the effects of an individual two-level fluctuator are visible. This particular fluctuator remained active for a week, until the sample was warmed up.

Switching has made all experiments we performed more difficult, and has made some experiments that we wanted to perform impossible. Better control over heterostructure stability is therefore essential for the increasingly difficult steps towards creating a quantum dot spin qubit.

1.10 Outline of this thesis

This thesis describes experiments I have been involved in during my time in the Quantum Transport group. When I started, the focus in the quantum dot section was on studying coherent many-body phenomena, in particular the Kondo effect. Some experiments exploring this topic are described in the second part of the thesis, chapters 7 to 9. In the beginning of 2002, we decided to abandon this field and focus on quantum computing, in particular the creation of a spin qubit. The first part of the thesis, chapters 2 to 6, describes the steps we have taken towards this goal.

The first step, described in chapter 2, was the development of the 'hardware' for the spin qubit: a device consisting of two coupled quantum dots that can be filled with one electron (spin) each, and flanked by two QPCs. The system can be probed in two different ways. In the regime where the tunnel rate between the dots and the leads is large ($>$ 100 kHz), we can perform conventional measurements of transport through one dot or two dots in series. Alternatively, even if the tunnel rate is small ($<$ 100 kHz), we can use a QPC to measure changes in the (average) charge on each of the two dots. This versatility has proven to be very useful. The type of device shown in this chapter was used for all subsequent experiments.

In chapter 3, it is shown that we can determine all relevant parameters of a quantum dot even when it is coupled very weakly to only one reservoir. In this regime, inaccessible to conventional transport experiments, we use a QPC charge detector to determine the tunnel rate between the dot and the reservoir. By measuring changes in the effective tunnel rate, we can determine the excited states of the dot.

In chapter 4, the QPC as a charge detector is pushed to a faster regime (~ 100 kHz), to detect single electron tunnel events in real time. We also determine the dominant contributions to the noise, and estimate the ultimate speed and sensitivity that could be achieved with this very simple method of charge detection.

In chapter 5, we develop a technique to perform single-shot measurement of the spin orientation of an individual electron in a quantum dot. This is done by combining fast QPC charge detection with ‘spin-to-charge conversion’. This constitutes a fully electrical technique to read out a spin qubit. We use it to determine the relaxation time of the single spin, and find a value of 0.85 ms at a magnetic field of 8 T, which becomes shorter at increasing magnetic field.

Chapter 6 finishes the section on spin qubits. It puts the results in perspective, discusses the next experimental steps to be taken, and identifies some possible problems.

Chapter 7 begins the second part of the thesis, by demonstrating a textbook example of the Kondo effect. It shows that the unitary limit of conductance ($G = 2e^2/h$) can be achieved. This implies that quantum correlations between the spin on the dot and the spins in the leads can make the dot completely transparent to electrons passing through.

In chapter 8, we study an anomalous strong Kondo effect that occurs when the spin singlet and triplet configurations of a 6-electron ‘vertical’ quantum dot are degenerate.

Finally, chapter 9 identifies and quantifies different cotunneling processes that occur in a vertical quantum dot containing 2 to 6 electrons.

References

[1] R.P. Feynman, *The Feynman Lectures on Physics*, Vol. 3 (Addison Wesley, 1970).

[2] M. Riebe *et al.*, Nature **429**, 734 (2004).

[3] M. D. Barrett *et al.*, Nature **429**, 737 (2004).

[4] V.B. Braginsky and F.Y. Khalili, *Quantum Measurement* (Cambridge University Press, 1992).

[5] S. Singh, *The Code Book* (Anchor Books/Doubleday, 2000).

[6] R.P. Feynman, *The Feynman Lectures on Computation*, edited by R.W. Allen and T. Hey (Perseus Publishing, 2000).

[7] D. Deutsch, Proc. R. Soc. Lond. A, 400 (1985).

[8] P.W. Shor, in *Proceedings of 35th Annual Symposium on Foundations of Computer Science* (IEEE Press, 1994).

[9] S. Lloyd, Science **273**, 1073 (1996).

[10] L.K. Grover, Phys. Rev. Lett. **79**, 325 (1997).

[11] P.W. Shor, in *Proceedings of 37th Annual Symposium on Foundations of Computer Science*, 56 (IEEE Press, 1996).

[12] A.M. Steane, Phys. Rev. Lett. **77**, 793 (1996).

[13] A.Y. Kitaev, in *Quantum Communication, Computing, and Measurement*, edited by A.S. Holevo, O. Hirota and C.M. Caves, 181 (Plenum Press, 1997).

[14] D. Aharonov and M. Ben-Or, quant-ph/9906129 (1999).

[15] L.M.K. Vandersypen *et al.*, Nature **414**, 883 (2001).

[16] D.P. DiVincenzo, Fortschr. Phys. **48**, 771 (2000).

[17] Quantum information science and technology roadmapping project, available at http://qist.lanl.gov/.

[18] D. Loss and D.P. DiVincenzo, Phys. Rev. A **57**, 120 (1998).

[19] Y. Kato, R.C. Myers, A.C. Gossard and D.D. Awschalom, Science **299**, 1201 (2003).

[20] A.V. Khaetskii and Yu.V. Nazarov, Phys. Rev. B **64**, 125316 (2001).

[21] V.N. Golovach, A. Khaetskii and D. Loss, Phys. Rev. Lett. **93**, 016601 (2004)

[22] L.M. Woods, T.L. Reinecke and Y. Lyanda-Geller, Phys. Rev. B **66**, 161318(R) (2002).

[23] S.I. Erlingsson and Yu.V. Nazarov, Phys. Rev. B **66**, 155327 (2002).

[24] Y. Nakamura, Yu.A. Pashkin and J.S. Tsai, Nature **398**, 786 (1999).

[25] T. Hayashi, T. Fujisawa, H.D. Cheong, Y.H. Jeong, and Y. Hirayama, Phys. Rev. Lett. **91**, 226804 (2003).

[26] L.P. Kouwenhoven, C.M. Marcus, P.L. McEuen, S. Tarucha, R.M. Westervelt, and N.S. Wingreen, in *Mesoscopic Electron Transport*, edited by L.L. Sohn, L.P. Kouwenhoven and G. Schön, (Kluwer, Series E **345**, 1997), p.105-214.

[27] N.W. Ashcroft and N.D. Mermin, *Solid state physics* (Brooks/Cole 1976).

[28] S. Tarucha, D.G. Austing, Y. Tokura, W.G. van der Wiel and L.P. Kouwenhoven, Phys. Rev. Lett. **84**, 2485 (2000).

[29] W.G. van der Wiel *et al.*, Physica B **256-258**, 173 (1998).

[30] D. Weinmann, W. Häusler and B. Kramer, Phys. Rev. Lett. **74**, 984 (1995).

[31] S. Tarucha, D.G. Austing, T. Honda, R.J. van der Hage and L.P. Kouwenhoven, Phys. Rev. Lett. **77**, 3613 (1996) .

[32] V.N. Golovach and D. Loss, Europhys. Lett. **62**, 83 (2003).

[33] G. Burkard, D. Loss, and D. P. DiVincenzo, Phys. Rev. B **59**, 2070 (1999).

[34] D.V. Averin and Yu.V. Nazarov, in *Single Charge Tunneling - Coulomb Blockade Phenomena in Nanostructures*, edited by H. Grabert and M. H. Devoret (Plenum Press and NATO Scientific Affairs Division, New York, 1992), p. 217.

[35] W.J. de Haas, J.H. de Boer and G.J. van den Berg, Physica **1**, 1115 (1934).

[36] J. Kondo, Prog. Theor. Phys. **32**, 37 (1964).

[37] L.P. Kouwenhoven and L.I. Glazman, Physics World **14**, 33 (2001).

[38] L.I. Glazman and M.E. Raikh, JETP Lett. **47**, 452 (1988).

[39] T.K. Ng and P.A. Lee, Phys. Rev. Lett. **61**, 1768 (1988).

[40] A. Kawabata, J. Phys. Soc. Jpn. **60**, 3222 (1991).

[41] J.M. Martinis, M.H. Devoret and J. Clarke, Phys. Rev. B **35**, 4682 (1987).

[42] K. Bladh *et al.*, Rev. Sci. Instr. **74**,1323 (2003).

[43] J.H. Davies, *The physics of low-dimensional semiconductors* (Cambridge University Press, 1998).

Chapter 2

Few-electron quantum dot circuit with integrated charge read-out

J. M. Elzerman, R. Hanson, J. S. Greidanus,
L. H. Willems van Beveren, S. De Franceschi,
L. M. K. Vandersypen, S. Tarucha and L. P. Kouwenhoven

We report on the realization of few-electron double quantum dots defined in a two-dimensional electron gas by means of surface gates on top of a GaAs/AlGaAs heterostructure. The double quantum dots are flanked by two quantum point contacts, serving as charge detectors. These enable determination of the precise number of conduction electrons on each dot. This number can be reduced to zero while still allowing transport measurements through the double dot. Even in the few-electron case, the tunnel coupling between the two dots can be controlled over a wide range, from the weak-coupling to the strong-coupling regime. In addition, we use microwave radiation to pump an electron from one dot to the other by absorption of a single photon. The experiments demonstrate that this quantum dot circuit can serve as a good starting point for a scalable spin-qubit system.

Parts of this chapter have been published in Physical Review B **67**, 161308 (2003).

2.1 Few-electron quantum dots

The experimental development of a quantum computer is presently at the stage of realizing few-qubit circuits. In the solid state, particular success has been achieved with superconducting devices, in which two macroscopic quantum states are used as a qubit two-level system (see [1] and references therein). The opposite alternative would be the use of two-level systems defined by microscopic variables, for instance the spin (or charge) state of single electrons confined in semiconductor quantum dots [2]. For the control of one-electron quantum states by electrical voltages, the first requirement is to realize an appropriate quantum dot circuit containing just a single conduction electron.

Single-electron quantum dots have been created in self-assembled structures [3] and also in small vertical pillars defined by etching [4]. (Recently, also semiconductor nanowires and carbon nanotubes have been used for this purpose.) The disadvantage of these types of quantum dots is that they are hard to integrate into circuits with a controllable coupling between the elements, although integration of vertical quantum dot structures is currently being pursued [5, 6]. Alternatively, we can use a system of lateral quantum dots defined in a two-dimensional electron gas (2DEG) by surface gates on top of a semiconductor heterostructure [2]. Here, integration of multiple dots is straightforward, by simply increasing the number of gate electrodes. In addition, the tunnel coupling between the dots can be tuned *in situ*, since it is controlled by the gate voltages. The challenge is to reduce the number of electrons to one per quantum dot. This has long been impossible, since reducing the electron number tends to be accompanied by a decrease in the tunnel coupling, resulting in a current too small to be measured [7].

In this chapter, we demonstrate double quantum dot devices containing a voltage-controllable number of electrons, down to a single electron. We have integrated these devices with charge detectors that can read out the charge state of the double quantum dot with a sensitivity better than a single electron charge. The importance of the present circuit is that it can serve as a fully tunable two-qubit system, following the proposal by Loss and DiVincenzo [8], which describes an optimal combination of the single-electron charge degree of freedom (for convenient manipulation using electrical voltages) and the spin degree of freedom (which promises a long coherence time, essential for encoding quantum information).

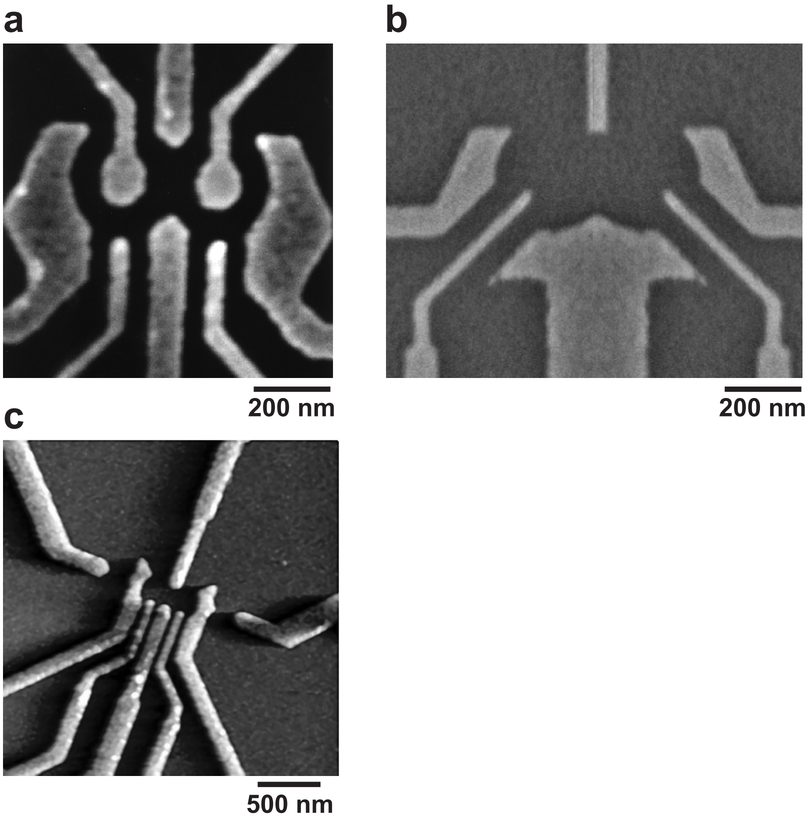

Figure 2.1: Few-electron quantum dot devices. **(a)** Scanning electron microscope image of the first sample, showing the metal gate electrodes (light) on top of a GaAs/AlGaAs heterostructure (dark) that contains a 2DEG 90 nm below the surface (with electron density 2.9×10^{11} cm^{-2}). This device was used only as a few-electron *single* dot. Due to the similarity of the image to characters from the Japanese 'Gundam' animation, this has become known as the Gundam design. The two gates coming from the top and ending in small circles (the 'eyes') were meant to make the dot confinement potential steeper, by applying a positive voltage to them (up to ~ 0.5 V). The gates were not very effective, and were left out in later designs. (The device was fabricated by Wilfred van der Wiel at NTT Basic Research Laboratories.) **(b)** Scanning electron microscope image of the second device, made on a similar heterostructure. It was used only as a few-electron *single* dot, and was more easily tunable than the first one. (The device was fabricated by Wilfred van der Wiel and Ronald Hanson at NTT Basic Research Laboratories.) **(c)** Atomic force microscope image of the third device, made on a similar heterostructure. This design, with two extra side gates to form two quantum point contacts, was operated many times as a single dot, and twice as a few-electron *double* dot. It was used for all subsequent measurements. A zoom-in of the gate structure is shown in Fig. 2.3a. (The device was fabricated by Ronald Hanson and Laurens Willems van Beveren at NTT Basic Research Laboratories.)

2.2 Samples

We have fabricated and measured several few-electron double quantum dots, of three different designs (Fig. 2.1). The first two types have only been used once as few-electron *single* dots. In both cases, one of the gate electrodes was not functioning, which prevented us from testing if these devices also function as few-electron *double* dots. The third type of device (Fig. 2.1c) did function as a double dot, and was used for all subsequent few-electron experiments (described in chapters 2 to 6).

To verify that the first device (Fig. 2.1a) can operate as a few-electron single quantum dot, we performed a large-bias measurement of the differential conductance through the dot. Going towards more negative gate voltage, a series of 'Coulomb diamonds' is revealed (Fig. 2.2a), in which the number of electrons on the dot, N, is constant. This is followed by a region in which the 'diamond' does not close, even up to a source-drain voltage of 10 mV, i.e. several times larger than the typical charging energy for a small dot ($\sim$ 2 meV). Therefore, in this region $N = 0$.

The tunnel coupling between the dot and the source and drain reservoirs could be changed by simply readjusting the gate voltages. For strong coupling, a zero-bias peak – hallmark of the Kondo effect – became visible throughout the one-electron diamond (Fig. 2.2b). From the width of the zero-bias peak (Fig. 2.2c) we found a Kondo temperature of about 0.4 K. The appearance of a one-electron Kondo effect (unpublished) implies that this quantum dot design allows the tunnel coupling to be tuned over a wide range, even in the few-electron regime. In addition, it is striking evidence that we can confine a single *spin* in a lateral quantum dot.

In the second quantum dot design (Fig. 2.1b), the narrow 'plunger' gates approach the dot more from the sides, rather than from below. In this way, they are further away from the central tunnel barrier, reducing the effect they have on the tunnel rate. Also, the gate coming from the top of the picture was made thinner, in order to make the tunnel barriers more easily controllable [7]. Thirdly, the characteristic gates ending in circles (see Fig. 2.1a) were left out. This device was quite easily tunable.

In the rest of this chapter, we use the third design (Fig. 2.1c). Two nominally identical devices are studied, both as shown in Fig. 2.3a. They consist of a double quantum dot flanked by two quantum point contacts (QPCs), defined in a 2DEG that is present below the surface of a GaAs/AlGaAs heterostructure. The layout of the double quantum dot is an extension of previously reported single dot devices [7]. The double dot is defined by applying negative voltages

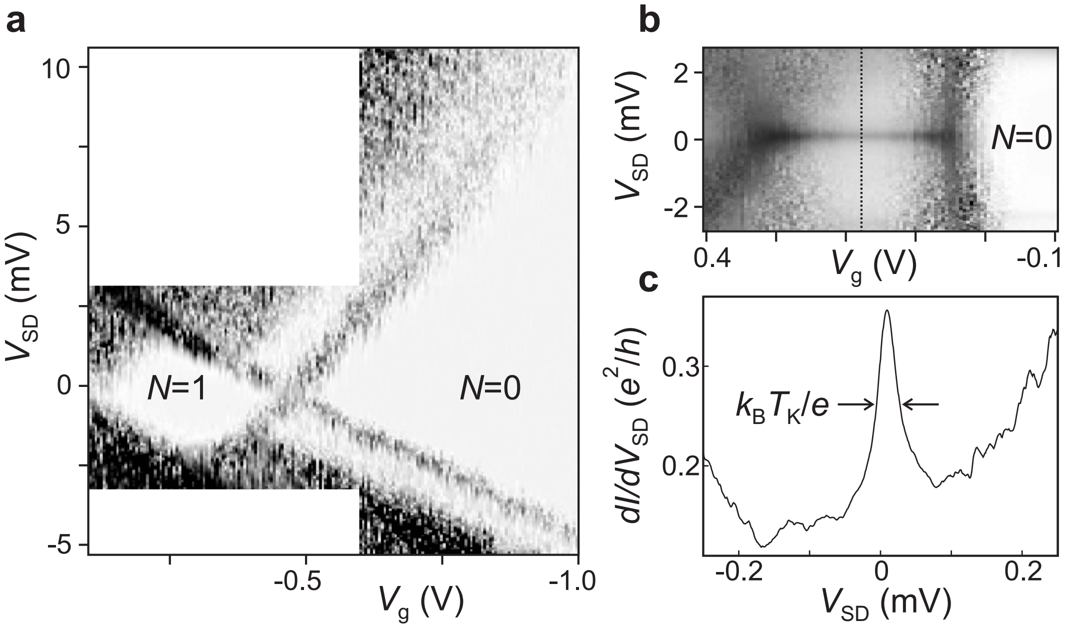

Figure 2.2: Kondo effect in a one-electron lateral quantum dot of the type shown in Fig. 2.1a. **(a)** Differential conductance (in grayscale) versus source-drain voltage, V_{SD}, and plunger gate voltage, V_g. In the white diamond and the white region to the right (indicated by $N = 1$ and $N = 0$, respectively), no current flows due to Coulomb blockade. The $N = 0$ region opens up to more than 10 mV, indicating that the dot is really empty here. **(b)** Close-up of the $N = 1$ diamond for stronger coupling to the reservoirs. A sharp Kondo resonance is visible at zero source-drain voltage. Although charge switching is very severe in this sample, the position of the Kondo resonance is very stable, as it is pinned to the Fermi energy of the reservoirs. **(c)** Kondo zero-bias peak in differential conductance, taken at the position indicated by the dotted line in (b).

to the 6 central gates. Gate T in combination with the left (right) gate, L (R), controls the tunnel barrier from the left (right) dot to drain 1 (source 2). Gate T in combination with the middle gate, M, controls the tunnel barrier between the two dots. The narrow 'plunger' gates, P_L and P_R, are used to change the electrostatic potential of the left and right dot, respectively. The left plunger gate is connected to a coaxial cable, so that we can apply high-frequency signals. In the present experiments we do not apply dc voltages to P_L. In order to control the number of electrons on the double dot, we use gate L for the left dot and P_R or R for the right dot. All measurements are performed with the sample cooled to a base temperature of about 10 mK inside a dilution refrigerator.

We first study sample 1. The individual dots are characterized using standard Coulomb blockade experiments [2], i.e. by measuring I_{DOT}. We find that the energy cost for adding a second electron to a one-electron dot is 3.7 meV. The one-electron excitation energy (i.e. the difference between the ground state and the first orbital excited state) is 1.8 meV at zero magnetic field. For a two-electron dot the energy difference between the spin singlet ground state and the spin triplet excited state is 1.0 meV at zero magnetic field. Increasing the field (perpendicular to the 2DEG) leads to a transition from a singlet to a triplet ground state at about 1.7 Tesla.

2.3 Quantum Point Contact as charge detector

As an alternative to measuring the current through the quantum dot, we can also measure the charge on the dot using one of the QPCs [9, 10]. To demonstrate this functionality, we first define only the left dot (by grounding gates R and P_R), and use the left QPC as a charge detector. The QPC is formed by applying negative voltages to $Q-L$ and L. This creates a narrow constriction in the 2DEG, with a conductance, G, that is quantized when sweeping the gate voltage V_{Q-L}. The last plateau (at $G = 2e^2/h$) and the transition to complete pinch-off (i.e. $G = 0$) are shown in Fig. 2.3b. We tune the QPC to the steepest point ($G \approx e^2/h$), where the QPC-conductance has a maximum sensitivity to changes in the electrostatic environment, including changes in the charge of the nearby quantum dot.

To change the number of electrons in the left dot, we make gate voltage V_M more negative (see Fig. 2.3c). This reduces the QPC current, due to the capacitive coupling from gate M to the QPC constriction. In addition, the changing gate voltage periodically pushes an electron out of the dot. The associated sudden change in charge lifts the electrostatic potential at the QPC constriction, resulting in a step-like feature in I_{QPC} (see the expansion in Fig. 2.3c, where the linear background is subtracted). This step indicates a change in the electron number. So, even without passing current through the dot, I_{QPC} provides information about the charge on the dot.

To enhance the charge sensitivity we apply a small modulation (0.3 mV at 17.7 Hz) to V_M and use lock-in detection to measure dI_{QPC}/dV_M [10]. The steps in I_{QPC} now appear as dips in dI_{QPC}/dV_M. Figure 2.3c shows the resulting dips, as well as the corresponding Coulomb peaks measured in the current through the dot. The coincidence of the Coulomb peaks and dips demonstrates that the QPC indeed functions as a charge detector. From the height of the step in Fig. 2.3b ($\sim$ 50 pA, typically 1-2% of the total current) compared to the noise ($\sim$ 5 pA for a measurement time of 100 ms), we estimate the sensitivity of the charge detector to be about $0.1e$, with e being the single electron charge. The unique advantage of

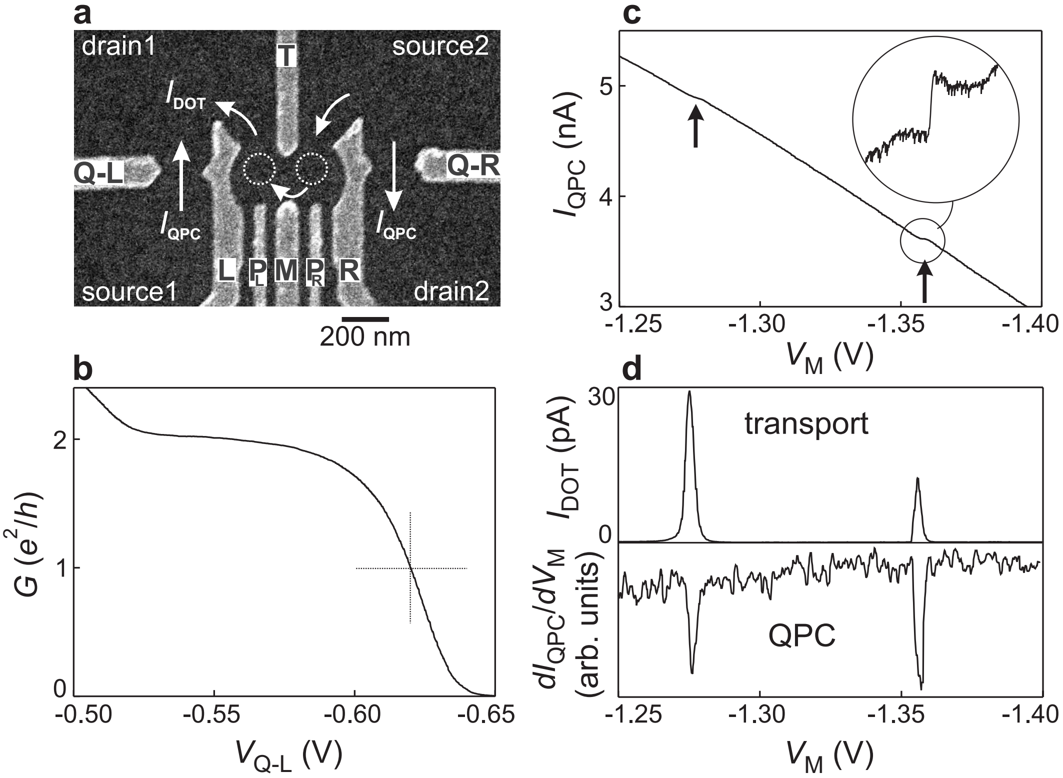

Figure 2.3: Operating the QPC as a charge detector of a single dot. **(a)** Scanning electron microscope image of the device, showing metallic surface gates (light gray) on top of a GaAs/AlGaAs heterostructure (dark gray). The device contains a 2DEG 90 nm below the surface, with an electron density of 2.9×10^{11} cm^{-2}. White dotted circles indicate the two quantum dots, white arrows show the possible current paths. A bias voltage, V_{DOT}, can be applied between source 2 and drain 1, leading to current through the dot(s), I_{DOT}. A bias voltage, V_{SD1} (V_{SD2}), between source 1 (source 2) and drain 1 (drain 2), yields a current, I_{QPC}through the left (right) QPC. **(b)** Conductance, G, of the left QPC versus gate voltage, V_{Q-L}, showing the last quantized plateau (at $G = 2e^2/h$) and the transition to complete pinch-off ($G = 0$). The QPC is set to the point of highest charge sensitivity, at $G \approx e^2/h$ (indicated by the dashed cross). **(c)**Current through the left QPC, I_{QPC}, versus left-dot gate voltage, V_M, with $V_{SD1} = 250$ μV and $V_{SD2} = V_{DOT} = 0$. Steps indicated by arrows correspond to changes in the number of electrons on the left dot. Encircled inset: the last step ($\sim$ 50 pA high), with the linear background subtracted. **(d)** Upper panel: Coulomb peaks measured in transport current through the left dot, with $V_{DOT} = 100$ μV and $V_{SD1} = V_{SD2} = 0$. Lower panel: changes in the number of electrons on the left dot measured with the left QPC, with $V_{SD1} = 250$ μV and $V_{SD2} = V_{DOT} = 0$).

QPC charge detection is that it provides a signal even when the tunnel barriers of the dot are so opaque that I_{DOT} is too small to be measured [9, 10]. This allows us to study quantum dots even when they are virtually isolated from the reservoirs. We explore this in more detail in chapters 3, 4 and 5.

2.4 Double dot charge stability diagram

The QPC can also detect changes in the charge configuration of the *double* dot. To demonstrate this, we use the QPC on the right to measure dI_{QPC}/dV_L versus V_L and V_{PR} (Fig. 2.4a), where V_L controls (mainly) the number of electrons on the left dot, and V_{PR} (mainly) that on the right. Dark lines in the figure signify a dip in dI_{QPC}/dV_L, corresponding to a change in the total number of electrons on the double dot. Together these lines form the so-called ‘honeycomb diagram’ [11, 12]. The almost-horizontal lines correspond to a change in the number of electrons on the left dot, whereas almost-vertical lines indicate a change in the electron number on the right. In the upper left region the ‘horizontal’ lines are not present, even though the QPC can still detect changes in the charge, as demonstrated by the presence of the ‘vertical’ lines. We conclude that in this region the *left* dot contains zero electrons. Similarly, a disappearance of the ‘vertical’ lines occurs in the lower right region, showing that here the *right* dot is empty. In the upper right region, the absence of lines shows that here the *double* dot is completely empty.

We are now able to identify the exact charge configuration of the double dot in every honeycomb cell, by simply counting the number of ‘horizontal’ and ‘vertical’ lines that separate it from the 00 region. In Fig. 2.4b the first few honeycomb cells are labelled according to their charge configuration, with e.g. the label ‘21’ meaning 2 electrons in the left dot and 1 on the right. Besides the dark lines, also short bright lines are visible, signifying a peak in dI_{QPC}/dV_L. These bright lines correspond to an electron being transferred from one dot to the other, with the total electron number remaining the same. (The fact that some charge transitions result in a dip in dI_{QPC}/dV_L and others in a peak, derives from the fact that we use the QPC on the *right* and apply the modulation to the gate on the *left*. When an electron is pushed out of the double dot by making V_L more negative, the QPC opens up and dI_{QPC}/dV_L displays a dip. When V_L pushes an electron from the left to the right dot, the QPC is closed slightly, resulting in a peak.) The visibility of all lines in the honeycomb pattern demonstrates that the QPC is sufficiently sensitive to detect even *inter-dot* transitions.

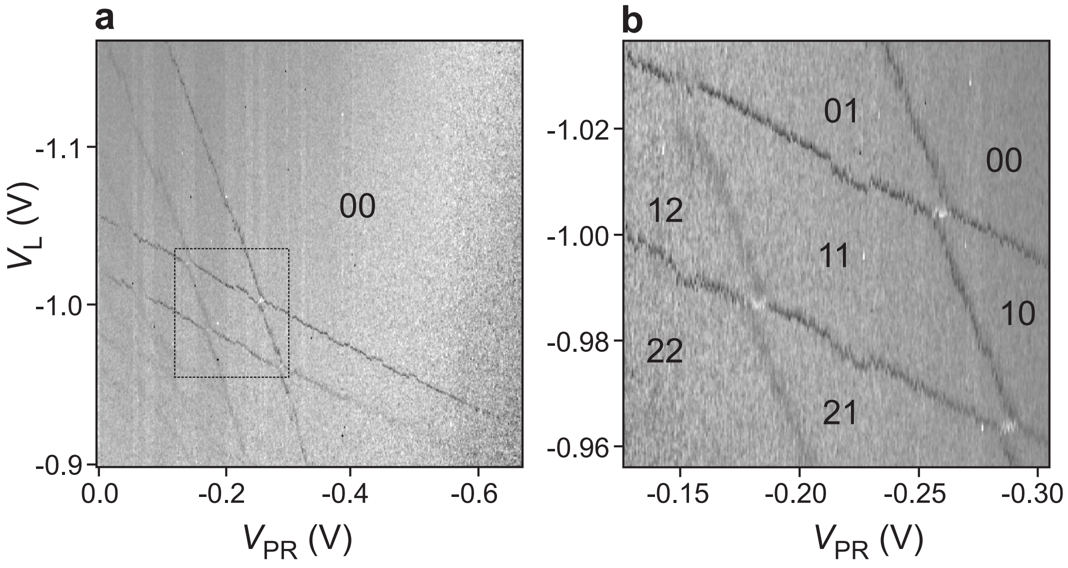

Figure 2.4: Using the QPC to measure the charge configuration of a double quantum dot in the few-electron regime. **(a)** dI_{QPC}/dV_L (in grayscale) versus V_L and V_{PR}, with $V_{SD2} = 100$ μV and $V_{SD1} = V_{DOT} = 0$. A small modulation (0.3 mV at 17.77 Hz) is applied to V_L, and the resulting modulation in I_{QPC} is measured with a lock-in amplifier to give dI_{QPC}/dV_L directly. The label '00' indicates the region where the double dot is completely empty. In the bottom left corner the dark lines are poorly visible. Here the tunnel rates to the reservoirs are quite large, leading to smearing of the steps in the QPC current, and therefore to smaller dips in dI_{QPC}/dV_L. **(b)** Zoom-in of Fig. 2.4a, showing the 'honeycomb' diagram for the first few electrons in the double dot. The black labels indicate the charge configuration, with '21' meaning 2 electrons in the left dot and 1 on the right.

2.5 Tunable tunnel barriers in the few-electron regime

In measurements of transport through lateral double quantum dots, the few-electron regime has never been reached [12]. The problem is that the gates that are used to deplete the dots also strongly influence the tunnel barriers. Reducing the electron number would therefore always lead to the Coulomb peaks becoming unmeasurably small, but not necessarily due to an empty double dot. The QPC detectors now permit us to compare charge and transport measurements.

Figure 2.5a shows the current through the double dot in the same region as shown in Fig. 2.4b. In the bottom left region the gates are not very negative, hence the tunnel barriers are quite open. Here the resonant current at the charge transition points is quite high ($\sim$ 100 pA, dark gray), and lines due to cotunneling

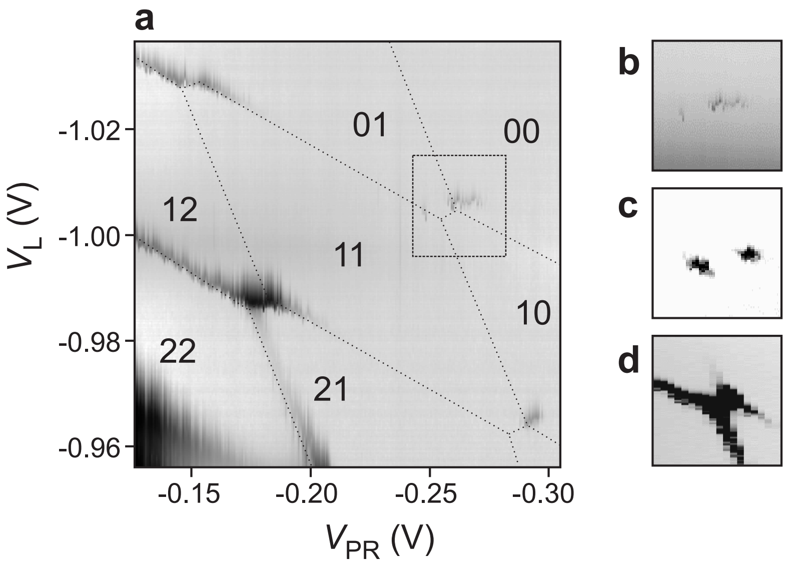

Figure 2.5: Current through the double quantum dot in the few-electron regime. **(a)** I_{DOT} (in logarithmic grayscale) versus V_L and V_{PR} in the same region as shown in Fig. 2.4b, with $V_{DOT} = 100\ \mu$V and $V_{SD1} = V_{SD2} = 0$. Dotted lines are extracted from Fig.2.4b. Dark gray indicates a current flowing, with the darkest regions (in the bottom left corner) corresponding to $\sim$ 100 pA. In the light gray regions current is zero due to Coulomb blockade. Inside the dashed square, the last triple points are faintly visible ($\sim$ 1 pA). (A smoothly varying background current due to a small leakage current from a gate to the 2DEG has been subtracted from all traces.) **(b)** Close-up of the region inside the dashed square in (a), showing the last two triple points before the double dot is completely empty. The current at these triple points is very small ($<$ 1 pA) since the tunnel barriers are very opaque. **(c)** Same two triple points for different values of the voltage applied to the gates defining the tunnel barriers. For these settings, the two individual triple points are well resolved, with a height of about 5 pA. The cotunneling current is not visible. **(d)** Same two triple points, but now with the gate voltages such that the tunnel barriers are very transparent. The current at the triple points is about 70 pA, and the cotunneling current is clearly visible.

are also visible [12]. Towards the top right corner the gate voltages become more negative, thereby closing off the barriers and reducing the current peaks (lighter gray). The last 'triple points' [12] that are visible ($< 1pA$) are shown in the dashed square. Using the dotted lines, extracted from the measured charge transition lines in Fig. 2.4b, we label the various regions in the figure according to the charge configuration of the double dot. Apart from a small shift, the dotted lines correspond nicely to the regions where a transport current is visible. This allows us to be confident that the triple points in the dashed square are really the last ones before the double quantum dot is empty. We are thus able to measure

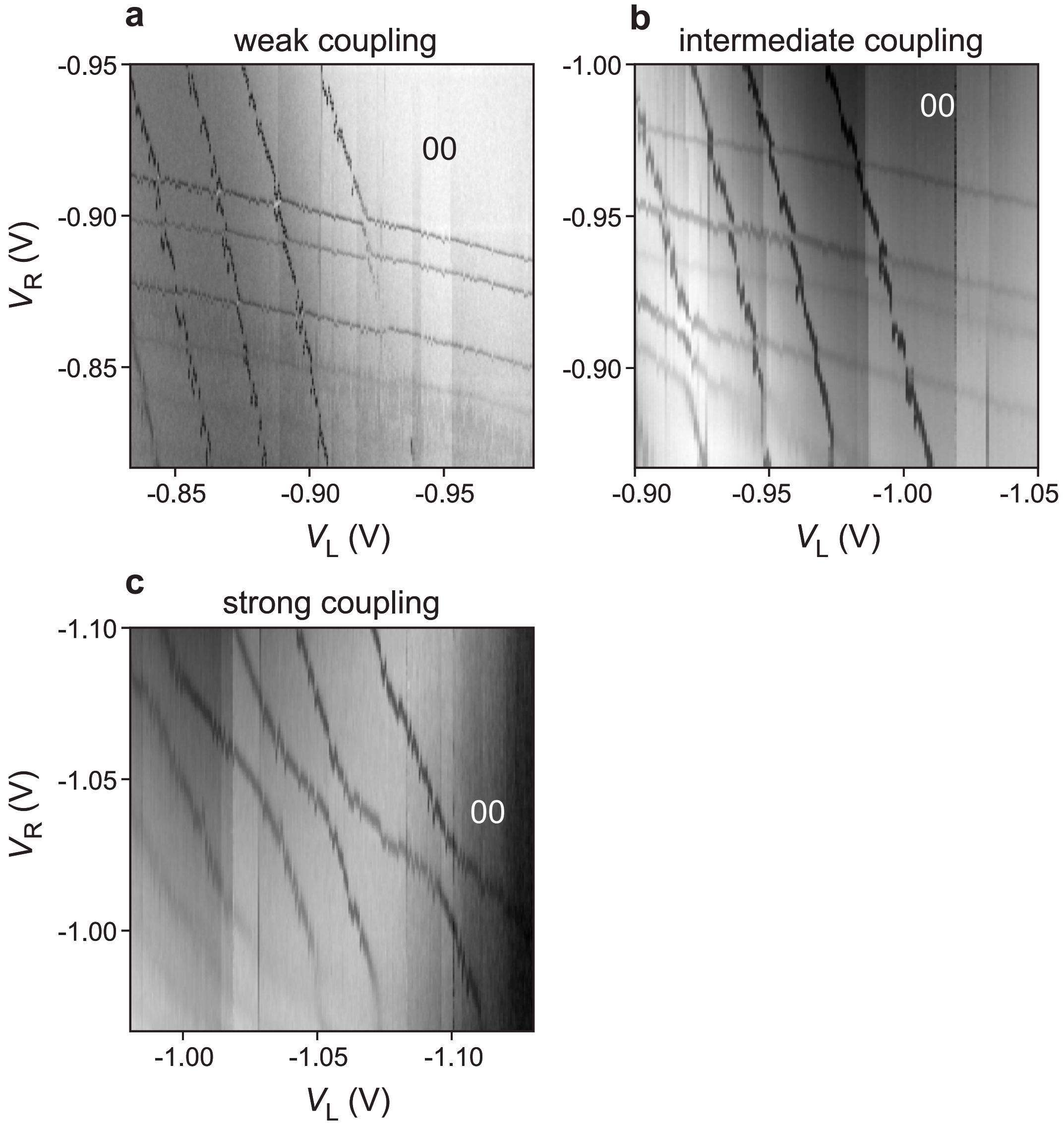

Figure 2.6: Controlling the inter-dot coupling (in sample 2) with V_M. These charge stability diagrams of the double quantum dot are measured using the QPC on the left. A small modulation (3 mV at 235 Hz) is applied to gate PR, and dI_{QPC}/dV_{PR} is measured with a lock-in amplifier and plotted in grayscale versus V_L and V_R. A magnetic field of 6 Tesla is applied in the plane of the 2DEG. **(a)** Weak-coupling regime. V_M is such that all dark lines indicating charge transitions are straight. The tunnel-coupling between the two dots is therefore negligible compared to the capacitive coupling. **(b)** Intermediate-coupling regime. V_M is 0.07 V less negative than in (a), such that lines in the bottom left corner are slightly curved. This signifies that here the inter-dot tunnel-coupling is comparable to the capacitive coupling. **(c)** Strong-coupling regime. V_M is 0.1 V less negative than in (b), such that all lines are very curved. This implies that the tunnel-coupling is dominating over the capacitive coupling and the double dot behaves as a single dot.

transport through a one-electron double quantum dot.

Even in the few-electron regime, the double dot remains fully tunable. By changing the voltage applied to gate T, we can make the tunnel barriers more transparent, leading to a larger current through the device. We use this procedure to increase the current at the last set of triple points. For the gate voltages used in Fig. 2.5b, the resonant current is very small (< 1 pA), and the triple points are only faintly visible. By making V_T less negative, the resonant current peaks grow to about 5 pA (Fig. 2.5c). The two triple points are clearly resolved an the cotunneling current is not visible. By changing V_T even more, the current at the last triple points can be increased to ~ 70 pA (Fig. 2.5d). For these settings, the triple points have turned into lines, due to the increased cotunneling current. This sequence demonstrates that we can tune the few-electron double dot from being nearly isolated from the reservoirs, to being very transparent.

We can also control the inter-dot coupling, by changing the voltage applied to gate M. This is demonstrated with a QPC charge measurement (performed on sample 2). We apply a square wave modulation of 3 mV at 235 Hz to the rightmost plunger gate, P_R, and measure dI_{QPC}/dV_{PR} using a lock-in amplifier. Fig. 2.6a shows the familiar honeycomb diagram in the few-electron regime. All lines indicating charge transitions are very straight, implying that for the gate settings used, the tunnnel-coupling between the two dots is negligible compared to the capacitive coupling. This is the so-called weak-coupling regime. (We note that the regular shape of the honeycomb pattern demonstrates that the double dot as a whole is still quite well-coupled to the leads, so that the total number of electrons can always find its lowest-energy value, unlike in Ref. [13].) By making V_M less negative, the tunnel barrier between the two dots is made more transparent, and the intermediate-coupling regime is reached (Fig. 2.6b). Most lines are still straight, except in the bottom left corner, where they are slightly curved. This signifies that here the inter-dot tunnel-coupling is comparable to the capacitive coupling. If we make V_M even less negative, we reach the strong-coupling regime (Fig. 2.6c). In this case, all lines are very curved, implying that the tunnel-coupling is dominating over the capacitive coupling. In this regime the double dot behaves like a single dot.

2.6 Photon-assisted tunneling

The use of gated quantum dots for quantum state manipulation in time requires the ability to modify the potential at high frequencies. We investigate the high-frequency behavior in the region around the last triple points (Fig. 2.7a), with a

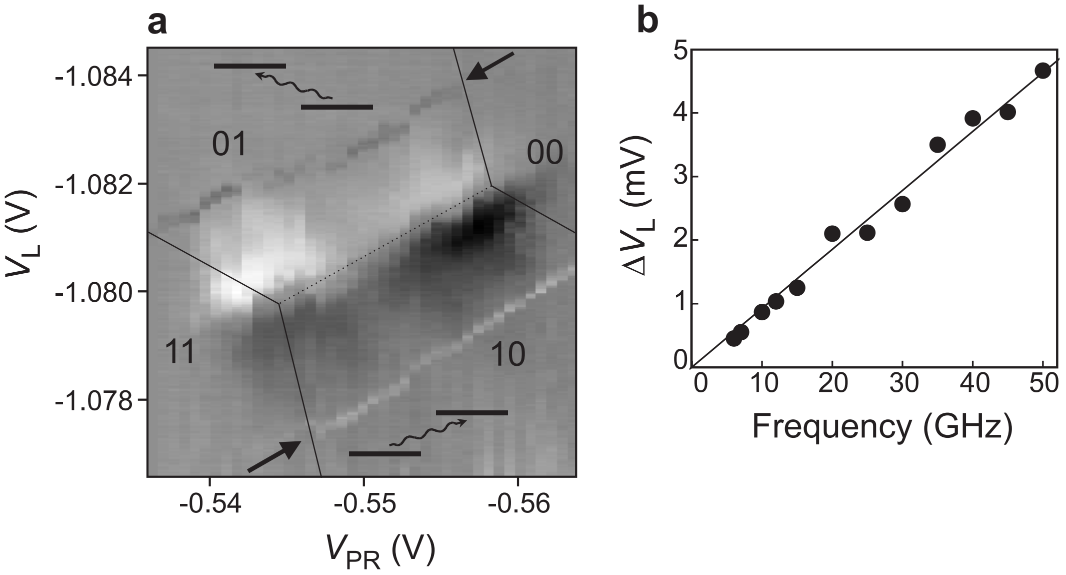

Figure 2.7: Photon-assisted tunneling in a one-electron double quantum dot. **(a)** Current through the double dot at the last set of triple points, with zero bias voltage ($V_{DOT} = V_{SD1} = V_{SD2} = 0$). A microwave signal of 50 GHz is applied to P_L. The microwaves pump a current, I_{DOT}, by absorption of single photons [12]. This photon-assisted current shows up as two lines, indicated by the two arrows. The white line (bottom) corresponds to electrons being pumped from the left to the right reservoir, the dark line (top) corresponds to pumping in the reverse direction. In the middle, around the dotted line separating the 01 from the 10 configuration, a finite current is induced by an unwanted voltage drop over the double dot, due to asymmetric coupling of the ac-signal to the two leads. **(b)** Separation between the two photon-assisted tunneling lines versus microwave frequency. The dependence is linear down to the lowest frequency of about 6 GHz, from which it follows that the inter-dot tunnel coupling (half the energy difference between bonding and anti-bonding state) is smaller than ~ 12 μeV.

50 GHz microwave-signal applied to gate P_L. At the dotted line the 01 and 10 charge states are degenerate in energy, so one electron can tunnel back and forth between the two dots. Away from this line there is an energy difference and only one charge state is stable. However, if the energy difference matches the photon energy, the transition to the other dot is possible by absorption of a single photon. Such photon-assisted tunneling events give rise to the two lines indicated by the arrows. At the lower (higher) line electrons are pumped from the the left (right) dot to the other one, giving rise to a negative (positive) photon-assisted current. We find that the distance (in terms of gate voltage) between the two photon-assisted tunneling lines, ΔV_L, scales linearly with frequency (Fig. 2.7b), as expected in the weak-coupling regime [12]. From the absence of bending of

the line in Fig. 2.7b down to a frequency of 6 GHz, it follows that the inter-dot tunnel coupling is smaller than about 12 μeV.

The realization of a controllable few-electron quantum dot circuit represents a significant step towards controlling the coherent properties of single electron spins in quantum dots [8, 14]. Integration with the QPCs permits charge read-out of closed quantum dots. We note that charge read-out only affects the spin state indirectly, via the spin-orbit interaction. The back-action on the spin should therefore be small (until spin-to-charge conversion is initiated), and can be further suppressed by switching on the charge detector only during the read-out stage. Experiments described in the following chapters focus on increasing the speed of the charge measurement, such that single-shot read-out of a single electron spin can be accomplished [14, 15].

We thank T. Fujisawa, T. Hayashi, Y. Hirayama, C. J. P. M. Harmans, B. van der Enden, and R. Schouten for valuable discussions and help. This work was supported by the Specially Promoted Research Grant-in-Aid for Scientific Research, from the Ministry of Education, Culture, Sports, Science and Technology in Japan, the DARPA-QUIST program (DAAD19-01-1-0659), and the Dutch Organisation for Fundamental Research on Matter (FOM).

References

[1] D. Vion, A. Aassime, A. Cottet, P. Joyez, H. Pothier, C. Urbina, D. Estève, and M. H. Devoret, Science **296**, 886 (2002).

[2] L. P. Kouwenhoven, C. M. Marcus, P. L. McEuen, S. Tarucha, R. M. Westervelt, and N. S. Wingreen, in *Mesoscopic Electron Transport*, edited by L. L. Sohn, L. P. Kouwenhoven, and G. Schön, NATO Advanced Study Institutes, Ser. E, Vol. **345** (Kluwer, Dordrecht, Boston, 1997), pp. 105-214.

[3] P. M. Petroff, A. Lorke, and A. Imamoglu, Phys. Today, 46 (May 2001).

[4] L. P. Kouwenhoven, D. G. Austing, and S. Tarucha, Rep. Prog. Phys. **64** (6), 701 (2001).

[5] K. Ono, D. G. Austing, Y. Tokura, and S. Tarucha, Science **297**, 1313 (2002).

[6] T. Hatano, M. Stopa, T. Yamaguchi, T. Ota, K. Yamada, and S. Tarucha, Phys. Rev. Lett. **3**, 066806 (2004).

[7] M. Ciorga, A. S. Sachrajda, P. Hawrylak, C. Gould, P. Zawadzki, S. Jullian, Y. Feng, and Z. Wasilewski, Phys. Rev. B **61**, R16315 (2000).

[8] D. Loss and D. P. DiVincenzo, Phys. Rev. A **57**, 120 (1998).

[9] M. Field, C. G. Smith, M. Pepper, D. A. Ritchie, J. E. F. Frost, G. A. C. Jones, and D. G. Hasko, Phys. Rev. Lett. **70**, 1311 (1993).

[10] D. Sprinzak, Y. Ji, M. Heiblum, D. Mahalu, and H. Shtrikman, Phys. Rev. Lett. **88**, 176805 (2002).

[11] H. Pothier, P. Lafarge, C. Urbina, D. Estève, and M. H. Devoret, Europhys. Lett. **17**, 249 (1992).

[12] W. G. van der Wiel, S. De Franceschi, J. M. Elzerman, T. Fujisawa, S. Tarucha, and L. P. Kouwenhoven, Rev. Mod. Phys. **75**, 1 (2003), see also cond-mat/0205350v2.

[13] A. W. Rushforth, C. G. Smith, M. D. Godfrey, H. E. Beere, D. A. Ritchie, and M. Pepper, Phys. Rev. B **69**, 113309 (2004).

[14] L. M. K. Vandersypen, R. Hanson, L. H. Willems van Beveren, J. M. Elzerman, J. S. Greidanus, S. De Franceschi, and L. P. Kouwenhoven, in *Quantum Computing and Quantum Bits in Mesoscopic Systems*, Kluwer Academic/Plenum Publishers, New York 2003), see also quant-ph/0207059.

[15] A. Aassime, G. Johansson, G. Wendin, R. J. Schoelkopf, and P. Delsing, Phys. Rev. Lett. **86**, 3376 (2001).

Chapter 3

Excited-state spectroscopy on a nearly closed quantum dot via charge detection

J. M. Elzerman, R. Hanson, L. H. Willems van Beveren,
L. M. K. Vandersypen and L. P. Kouwenhoven

We demonstrate a method for measuring the discrete energy spectrum of a quantum dot connected very weakly to a single lead. A train of voltage pulses applied to a metal gate induces tunneling of electrons between the quantum dot and a reservoir. The effective tunnel rate depends on the number and nature of the energy levels in the dot made accessible by the pulse. Measurement of the charge dynamics thus reveals the energy spectrum of the dot, as demonstrated for a dot in the few-electron regime.

Parts of this chapter have been published in Applied Physics Letters **84**, 4617 (2004).

3.1 Introduction

Few-electron quantum dots are considered as qubits for quantum circuits, where the quantum bit is stored in the spin or orbital state of an electron in a single or double dot. The elements in such a device must have functionalities such as initialization, one- and two-qubit operations and read-out [1]. For all these functions it is necessary to have precise knowledge of the qubit energy levels. Standard spectroscopy experiments involve electron transport through the quantum dot while varying both a gate voltage and the source-drain voltage [2]. This requires that the quantum dot be connected to two leads with a tunnel coupling large enough to obtain a measurable current [3].

Coupling to the leads unavoidably introduces decoherence of the qubit: even if the number of electrons on the dot is fixed due to Coulomb blockade, an electron can tunnel out of the dot and be replaced by another electron through a second-order tunneling process, causing the quantum information to be irretrievably lost. Therefore, to optimally store qubits in quantum dots, higher-order tunneling has to be suppressed, i.e. the coupling to the leads must be made as small as possible. Furthermore, real-time observation of electron tunneling, important for single-shot read-out of spin qubits via spin-to-charge conversion, also requires a small coupling of the dot to the leads. In this regime, current through the dot would be very hard or even impossible to measure. Therefore an alternative spectroscopic technique is needed, which does not rely on electron transport through the quantum dot.

Here we present spectroscopy measurements using charge detection. Our method resembles experiments on superconducting Cooper-pair boxes and semiconductor disks which have only one tunnel junction so that no net current can flow. Information on the energy spectrum can then be obtained by measuring the energy for adding an electron or Cooper-pair to the box, using a single-electron transistor (SET) operated as a charge detector [4, 5, 6]. We are interested in the excitation spectrum for a given number of electrons on the box, rather than the addition spectra. We use a quantum point contact (QPC) as an electrometer [7] and excitation pulses with repetition rates comparable to the tunnel rates to the lead, to measure the discrete energy spectrum of a nearly isolated one- and two-electron quantum dot.

3.2 Tuning the tunnel barriers

The quantum dot and QPC are defined in the two-dimensional electron gas (2DEG) in a GaAs/$\mathrm{Al}_{0.27}\mathrm{Ga}_{0.73}$As heterostructure by dc voltages on gates T, M, R

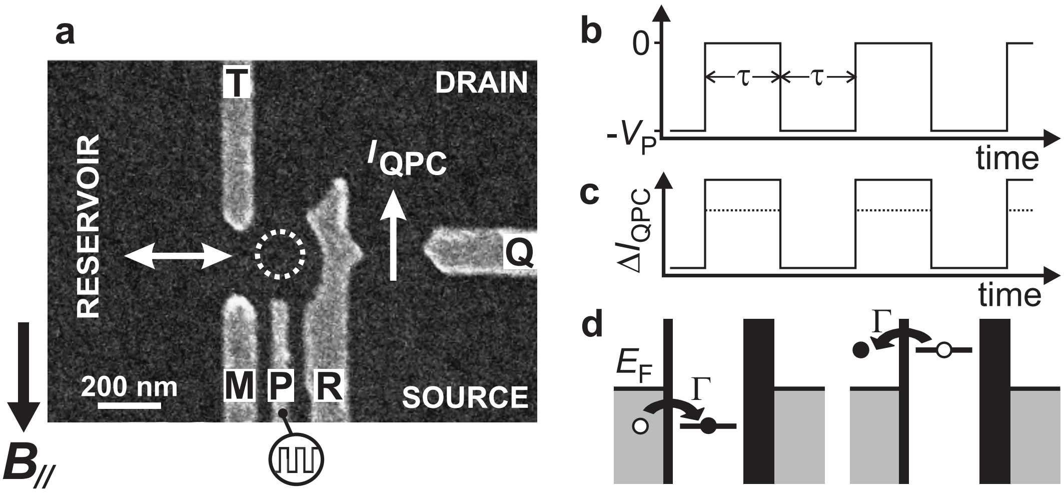

Figure 3.1: QPC response to a pulse train applied to the plunger gate. **(a)** Scanning electron micrograph of a quantum dot and quantum point contact, showing only the gates used in the present experiment (the complete device is described in ref. [12]) and chapter 2. **(b)** Pulse train applied to gate P. **(c)** Schematic response in QPC current, ΔI_{QPC}, when the charge on the dot is unchanged by the pulse (solid line) or increased by one electron charge during the 'high' stage of the pulse (dashed). **(d)** Schematic electrochemical potential diagrams during the high (left) and low (right) pulse stage, when the ground state is pulsed across the Fermi level in the reservoir, E_F.

and Q (Fig. 3.1a). The dot's plunger gate, P, is connected to a coaxial cable, to which we can apply voltage pulses (rise time 1.5 ns). The QPC charge detector is operated at a conductance of about e^2/h with source-drain voltage $V_{SD} = 0.2$ mV. All data are taken with a magnetic field $B_{//} = 10$ T applied in the plane of the 2DEG, at an effective electron temperature of about 300 mK.

We first describe the procedure for setting the gate voltages such that tunneling in and out of the dot take place through one barrier only (i.e. the other is completely closed), and the remaining tunnel rate be well controlled. For gate voltages far away from a charge transition in the quantum dot, a pulse applied to gate P (Fig. 3.1b) modulates the QPC current via the cross-capacitance only (solid trace in Fig. 3.1c). Near a charge transition, the dot can become occupied with an extra electron during the high stage of the pulse (Fig. 3.1d). The extra electron on the dot reduces the current through the QPC. The QPC response to the pulse is thus smaller when tunneling takes place (dotted trace in Fig. 3.1c). We denote the amplitude of the difference between solid and dotted traces as the 'electron response'.

Now, even when tunneling is allowed energetically, the electron response is only non-zero when an electron has sufficient time to actually tunnel into the dot

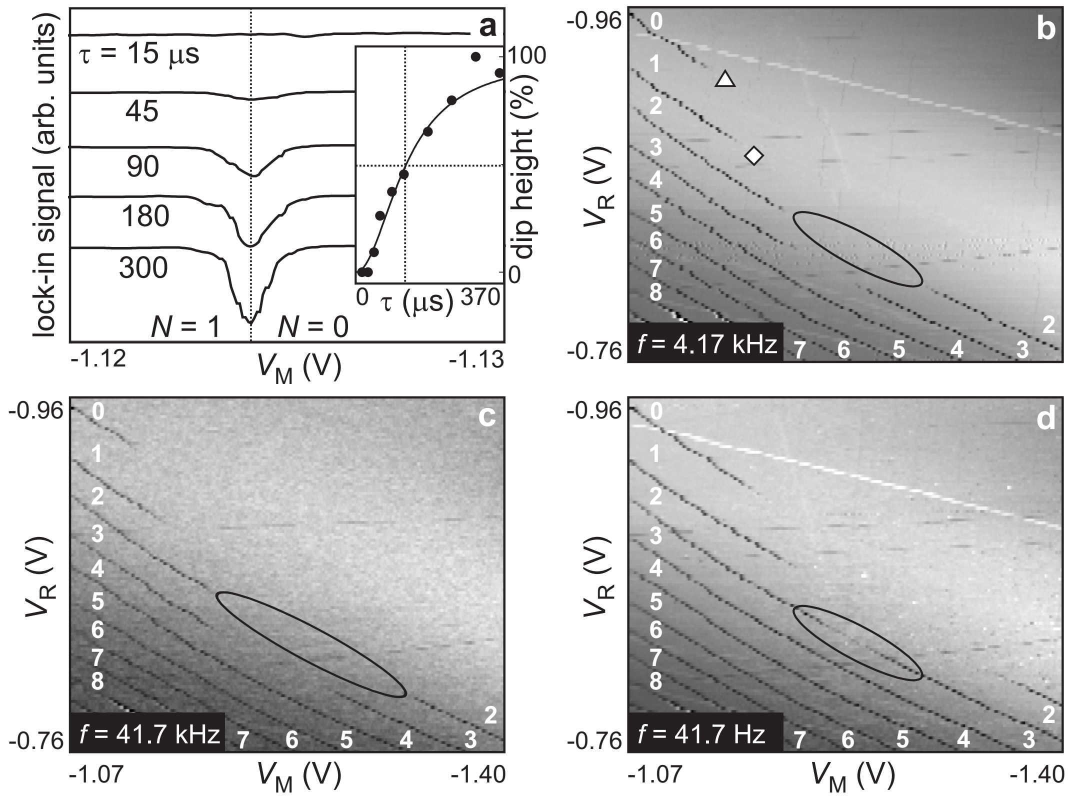

Figure 3.2: Lock-in detection of electron tunneling. **(a)** Lock-in signal at $f = 1/(2\tau)$ versus V_M for different pulse times, τ, with $V_P = 1$ mV. The dip due to the electron response disappears for shorter pulses. (Individual traces have been lined up horizontally to compensate for a fluctuating offset charge, and have been given a vertical offset for clarity.) (Inset) Height of the dip versus τ, as a percentage of the maximum height (obtained at long τ). Circles: experimental data. Dashed lines indicate the pulse time ($\tau \approx 120$ μs) for which the dip size is half its maximum value. Solid line: calculated dip height using $\Gamma = (40\ \mu\text{s})^{-1}$. **(b)** Lock-in signal in grayscale versus V_M and V_R for $V_P = 1$ mV and $f = 4.17$ kHz. Dark lines correspond to dips as in (a), indicating that the electron number changes by one. White labels indicate the absolute number of electrons on the dot. **(c)** Same plot as in (b), but with larger pulse repetition frequency ($f = 41.7$ kHz). **(d)** Same plot as in (b), but with smaller pulse repetition frequency ($f = 41.7$ Hz).

during the pulse time, τ. By measuring the electron response as a function of τ, we can extract the tunnel rate, Γ, as demonstrated in Fig. 3.2a. We apply a pulse train to gate P with equal up and down times, so the repetition rate is $f = 1/(2\tau)$ (Fig. 3.1b). The QPC response is measured using lock-in detection at frequency f [8], and is plotted versus the dc voltage on gate M. For long pulses (lowest curves) the traces show a dip, which is due to the electron response when crossing the zero-to-one electron transition. Here, $f \ll \Gamma$ and tunneling occurs quickly on the scale of the pulse duration. For shorter pulses the dip gradually disappears. We find analytically [9] that the dip height is proportional to $1 - \pi^2/(\Gamma^2\tau^2 + \pi^2)$, so the dip height should equal half its maximum value when $\Gamma\tau = \pi$. From the data (inset to Fig. 3.2a), we find that this happens for $\tau \approx 120$ μs, giving $\Gamma \approx (40$ $\mu\mathrm{s})^{-1}$. Using this value for Γ in the analytical expression given above, we obtain the solid line in the inset to Fig. 3.2a, which nicely matches the measured data points.

We explore several charge transitions in Fig. 3.2b, which shows the lock-in signal in grayscale for $\tau = 120$ μs, i.e. $f = 4.17$ kHz. The slanted dark lines correspond to dips as in Fig. 3.2a. From the absence of further charge transitions past the topmost dark line, we obtain the absolute electron number starting from zero. In the top left region of Fig. 3.2b, the right tunnel barrier (between gates R and T) is much more opaque than the left tunnel barrier (between M and T). Here, charge exchange occurs only with the left reservoir (indicated as 'reservoir' in Fig. 3.1a). Conversely, in the lower right region charge is exchanged only with the drain reservoir. In the middle region, indicated for the two-to-three electron transition by an ellipse, both barriers are too opaque and no charge can flow into or out of the dot during the 120 μs pulse; consequently the electron response becomes zero and thus the dark line disappears. For shorter pulses, i.e. larger pulse repetition frequency, the region where the dark line disappears becomes wider (ellipse in Fig. 3.2c). For longer pulses the dark line reappears (Fig. 3.2d). By varying the voltages on gates M and R, we can thus precisely set the tunnel rate to the left or right reservoir for each charge transition.

3.3 Excited-state spectroscopy for $N = 1$

For spectroscopy measurements on a one-electron dot, we set the gate voltages near the zero-to-one electron transition at the point indicated as △ in Fig. 3.2b. At this point, the dot is operated as a charge box, with all tunnel events occurring through just a single barrier. The pulse repetition rate is set to 385 Hz, so that the dip height is half its maximum value. The electron response is then very sensitive to changes in the tunnel rate, which occur when an excited state becomes accessible for tunneling.

Fig. 3.3a shows the electron response for a pulse amplitude larger than was used for the data in Fig. 3.2. The dip now exhibits a shoulder on the right side (indicated by 'b'), which we can understand as follows. Starting from the right ($N = 0$), the dip develops as soon as the ground state (GS) is pulsed across the

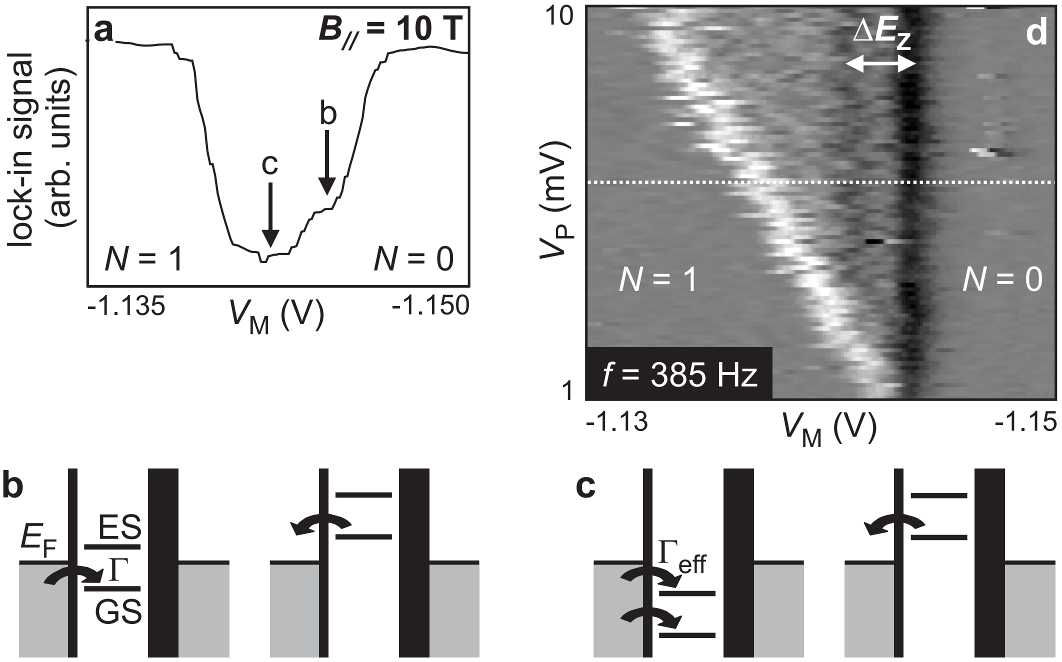

Figure 3.3: Excited-state spectroscopy in a one-electron dot. **(a)** Lock-in signal at $f = 385$ Hz versus V_M, with $V_P = 6$ mV. The dip is half the maximum value (obtained at low f and small V_P) from which we conclude that $\Gamma \approx 2.4$ kHz. **(b)** Schematic electrochemical potential diagrams for the case that only the GS is pulsed across E_F. **(c)** Idem when both the GS and an ES are pulsed across E_F. **(d)** Derivative of the lock-in signal with respect to V_M, plotted as a function of V_M and V_P (individual traces have been lined up to compensate for a fluctuating offset charge). The curve in (a) is taken at the dotted line. The Zeeman energy splitting between the one-electron GS (spin-up) and first ES (spin-down) is indicated by ΔE_Z.

Fermi level E_F and an electron can tunnel into the dot (Fig. 3.3b). As V_M is made less negative, we reach the point where both the GS and an excited state (ES) are pulsed across E_F (Fig. 3.3c). The effective rate for tunneling on the box is now the sum of the rate for tunneling in the GS and for tunneling in the ES, and as a result the dip becomes deeper (the electron response increases). When V_M is made even less negative, the one-electron GS lies below E_F during both stages of the pulse, so there is always one electron on the dot. The electron response is now zero and the dip ends.

The derivative of a set of curves as in Fig. 3.3a is plotted in Fig. 3.3d. Three lines are observed. The right vertical, dark line corresponds to the right flank of the dip in Fig. 3.3a, the onset of tunneling to the GS. The slanted bright line corresponds to the left flank of the dip in Fig. 3.3a (with opposite sign in the derivative) and reflects the pulse amplitude. The second, weaker, but clearly visible dark vertical line represents an ES. The distance between the two vertical lines is proportional to the energy difference between GS and ES.

We identify the ground and first excited state observed in this spectroscopy experiment as the spin-up and spin-down state of a single electron on the quantum dot. For $B_{//} = 10$ T, the Zeeman energy is about 0.21 meV [10], while the excitation energy of the first orbital excited state is of order 1 meV. The distance between the two vertical lines can, in principle, be converted to energy and directly provide the spin excitation energy. However, it is difficult to determine independently the conversion factor between gate voltage and energy in this regime of a nearly closed quantum dot. Instead we take the measured Zeeman splitting from an earlier transport measurement [10] and deduce the conversion factor from gate voltage to energy, $\alpha = 105$ meV/V. This value will be used below, to convert the two-electron data to energy.

3.4 Excited-state spectroscopy for $N = 2$

Fig. 3.4a shows pulse spectroscopy data for the one-to-two electron transition, taken with the gate settings indicated by $\diamond$ in Fig. 3.2b. The rightmost vertical line corresponds to transitions between the one-electron GS (spin-up) and the two-electron GS (spin singlet) only. As V_P is increased above 5 mV, the two-electron ES (spin triplet) also becomes accessible, leading to an enhanced tunnel rate [11]. This gives rise to the left vertical line, and the distance between the two vertical lines corresponds to the singlet-triplet energy splitting ΔE_{ST}. Converted to energy, we obtain $\Delta E_{ST} = 0.49$ meV.

Excitations of the one-electron dot can be made visible at the one-to-two electron transition as well, by changing the pulse frequency to 1.538 kHz (Fig. 3.4b). This is too fast for electrons to tunnel if only the GS is accessible, so the rightmost line almost vanishes. However, a second slanted line becomes visible (indicated by the arrow in Fig. 3.4b), corresponding not to an increased tunnel rate into the dot (due to an $N = 2$ ES), but to an increased tunnel rate out of the dot (due to an $N = 1$ ES). Specifically, if the pulse amplitude is sufficiently large, either the spin-up or the spin-down electron can tunnel out of the two-electron dot. This is explained schematically in Fig. 3.4c and d.

Similar experiments at the transition between two and three electrons, and for tunnel rates to the reservoir ranging from 12 Hz to 12 kHz, yield similar excitation spectra.

This work demonstrates that an electrometer such as a QPC can reveal not only the charge state of a quantum dot, but also its tunnel coupling to the outside

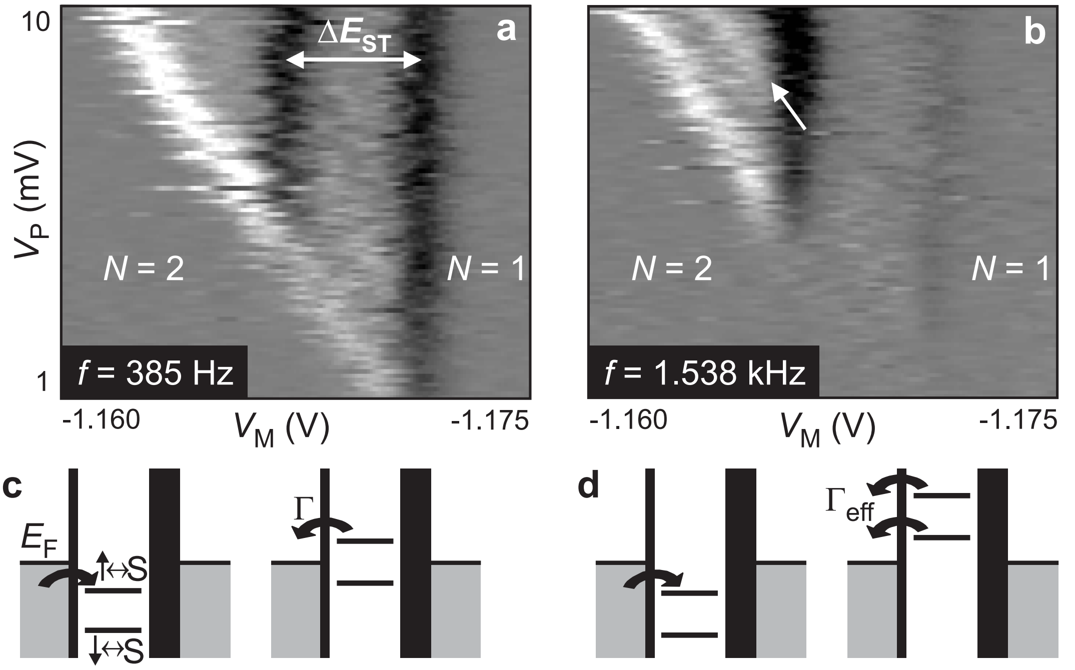

Figure 3.4: Excited state spectroscopy in a two-electron dot. **(a)** Similar to Fig. 3.3d, but for the one-to-two electron transition. Again, $f = 385$ Hz. We clearly observe the singlet-triplet splitting ΔE_{ST} (individual traces in (a) and (b) have been lined up). **(b)** Same experiment but with $f = 1.538$ kHz, which increases the contrast for excited states. An extra slanted line appears (arrow), corresponding to the $N = 1$ ES, spin-down. **(c)** Schematic electrochemical potential diagram for the case that only the spin-down electron can leave from the two-electron GS (spin singlet). This occurs to the left of the bright line indicated by the arrow in (b). **(d)** Idem when either the spin-up or the spin-down electron can leave from the spin singlet. This occurs to the right of the arrow in (b), and leads to a larger effective tunnel rate.

world and the energy level spectrum of its internal states. We can thus access all the relevant properties of a quantum dot, even when it is almost completely isolated from the leads.

We thank T. Fujisawa, S. Tarucha, T. Hayashi, T. Saku, Y. Hirayama and R.N. Schouten for useful discussions and experimental help. This work was supported by the DARPA-QUIST program, the ONR and the EU-RTN network on spintronics.

References

[1] D. Loss and D.P. DiVincenzo, Phys. Rev. A **57**, 120 (1998).

[2] L.P. Kouwenhoven, C.M. Marcus, P.L. McEuen, S. Tarucha, R.M. Westervelt, and N.S. Wingreen, in Mesoscopic Electron Transport, v. 345 of NATO Advanced Study Institutes, Ser. E: Applied Sciences, L. L. Sohn, L. P. Kouwenhoven, G. Schön, Eds. (Kluwer Academic, Dordrecht, 1997).

[3] M. Ciorga, A. S. Sachrajda, P. Hawrylak, C. Gould, P. Zawadzki, S. Jullian, Y. Feng, and Z. Wasilewski1, Phys. Rev. B **61**, R16315 (2000).

[4] P. Lafarge, H. Pothier, E.R. Williams, D. Esteve, C. Urbina, and M.H. Devoret, Zeitschrift für Physik B, **85**, 327 (1991).

[5] R.C. Ashoori, H. L. Stormer, J. S. Weiner, L. N. Pfeiffer, S. J. Pearton, K. W. Baldwin, and K. W. West, Phys. Rev. Lett. **68**, 3088 (1992).

[6] K.W. Lehnert, K. Bladh, L. F. Spietz, D. Gunnarsson, D. I. Schuster, P. Delsing, and R. J. Schoelkopf, Phys. Rev. Lett. **90**, 027002 (2003).

[7] M. Field, C. G. Smith, M. Pepper, D. A. Ritchie, J. E. F. Frost, G. A. C. Jones, and D. G. Hasko, Phys. Rev. Lett. **70**, 1311 (1993).

[8] D. Sprinzak, Y. Ji, M. Heiblum, D. Mahalu, and H. Shtrikman, Phys. Rev. Lett. **88**, 176805 (2002).

[9] This expression is obtained by multiplying the probability that the dot is empty, $P(t)$, with a sine-wave of frequency f (as is done in the lock-in amplifier), and averaging the resulting signal over one period. $P(t)$ is given by $\exp(-\Gamma t)(1-\exp(-\Gamma\tau))/(1-\exp(-2\Gamma\tau))$ during the high stage of the pulse, and by $1-P(t-\tau)$ during the low stage.

[10] R. Hanson, B. Witkamp, L. M. K. Vandersypen, L. H. Willems van Beveren, J. M. Elzerman, and L. P. Kouwenhoven, Phys. Rev. Lett. **91**, 196802 (2003).

[11] The expected Zeeman splitting of the triplet state is not resolved here.

[12] J. M. Elzerman, R. Hanson, J. S. Greidanus, L. H. Willems van Beveren, S. De Franceschi, L. M. K. Vandersypen, S. Tarucha, and L. P. Kouwenhoven, Phys. Rev. B **67**, R161308 (2003).

Chapter 4

Real-time detection of single electron tunneling using a quantum point contact

L. M. K. Vandersypen, J. M. Elzerman, R. N. Schouten,
L. H. Willems van Beveren, R. Hanson and L. P. Kouwenhoven

We observe individual tunnel events of a single electron between a quantum dot and a reservoir, using a nearby quantum point contact (QPC) as a charge meter. The QPC is capacitively coupled to the dot, and the QPC conductance changes by about 1% if the number of electrons on the dot changes by one. The QPC is voltage biased and the current is monitored with an IV-convertor at room temperature. At present, we can resolve tunnel events separated by only 8 μs, limited by noise from the IV-convertor. Shot noise in the QPC sets a 10 ns lower bound on the accessible timescales.

This chapter has been submitted for publication in Applied Physics Letters (2004).

4.1 Charge detectors

Fast and sensitive detection of charge has greatly propelled the study of single-electron phenomena. The most sensitive electrometer known today is the single-electron transistor (SET) [1], incorporated into a radio-frequency resonant circuit [2]. Such RF-SETs can be used for instance to detect charge fluctuations on a quantum dot, capacitively coupled to the SET island [3, 4]. Already, real-time electron tunneling between a dot and a reservoir has been observed on a sub-μs timescale [3].

A much simpler electrometer is the quantum point contact (QPC). The conductance, G_Q, through the QPC channel is quantized, and at the transitions between quantized conductance plateaus, G_Q is very sensitive to the electrostatic environment, including the number of electrons, N, on a dot in the vicinity [5]. This property has been exploited to measure fluctuations in N in real-time, on a timescale from seconds [6] down to about 10 ms [7].

Here we demonstrate that a QPC can be used to detect single-electron charge fluctuations in a quantum dot in less than $10\,\mu$s, and analyze the fundamental and practical limitations on sensitivity and bandwidth.

4.2 Sample and setup

The quantum dot and QPC are defined in the two-dimensional electron gas (2DEG) formed at a GaAs/$\mathrm{Al_{0.27}Ga_{0.73}As}$ interface 90 nm below the surface, by applying negative voltages to metal surface gates (Fig. 4.1a). The device is attached to the mixing chamber of a dilution refrigerator with a base temperature of 20 mK, and the electron temperature is $\sim$ 300 mK in this measurement. The dot is set near the $N = 0$ to $N = 1$ transition, with the gate voltages tuned such that the dot is isolated from the QPC drain, and has a small tunnel rate, Γ, to the reservoir. Furthermore, the QPC conductance is set at $G_Q = 1/R_Q \approx (30\,\mathrm{k}\Omega)^{-1}$, roughly halfway the transition between $G_Q = 2e^2/h$ and $G_Q = 0$, where it is most sensitive to the electrostatic environment [9].

A schematic of the electrical circuit is shown in Fig. 4.1b. The QPC source and drain are connected to room temperature electronics by signal wires, which run through Cu-powder filters at the mixing chamber to block high frequency noise ($>$ 100 MHz) coming from room temperature. Each signal wire is twisted with a ground wire from room temperature to the mixing chamber. A voltage, V_i, is applied to the source via a home-built opto-coupled isolation stage. The current through the QPC, I, is measured via an IV-convertor connected to the drain, and an opto-coupled isolation amplifier, both home-built as well. The IV-

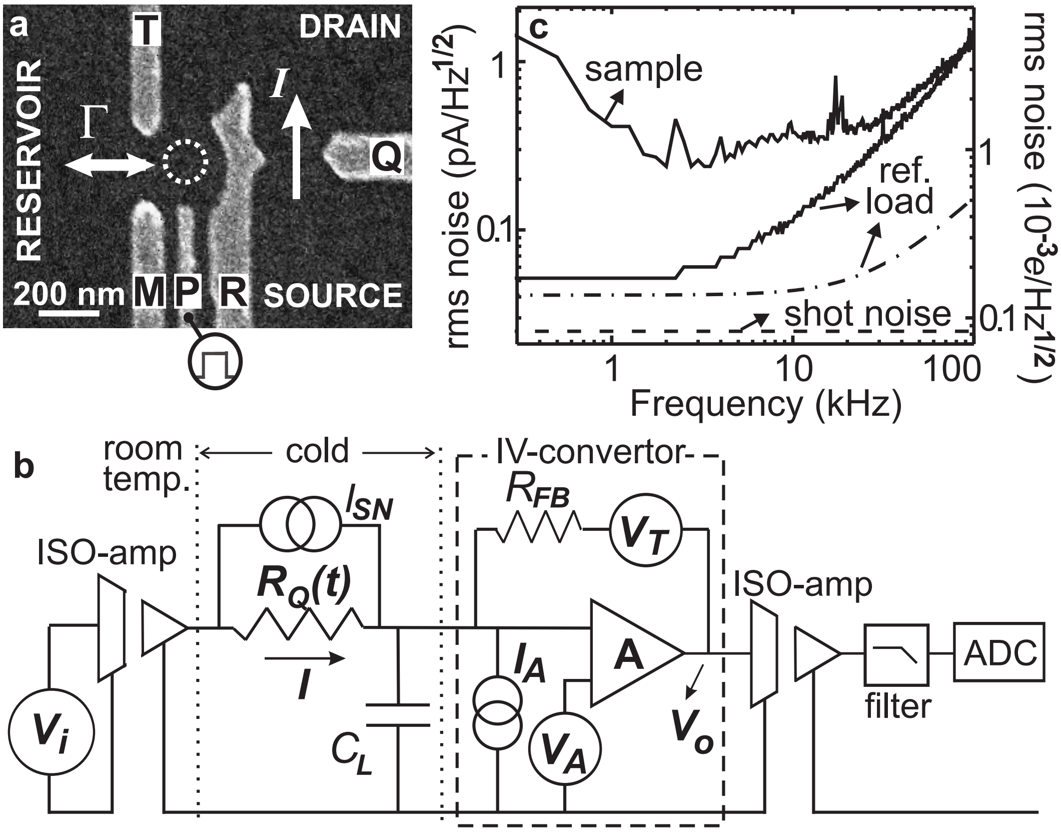
a
T
DRAIN
RESERVOIR
Γ
I
Q
200 nm
M
P
R
SOURCE
c
sample
ref.
load
shot noise
1
0.1
1
10
100
Frequency (kHz)
rms noise (pA/Hz$^{1/2}$)
1
0.1
rms noise (10^{-3}e/Hz$^{1/2}$)
b
room
temp.
cold
IV-convertor
ISO-amp
I_{SN}
$R_Q(t)$
R_{FB}
V_T
I
I_A
A
V_o
V_i
C_L
V_A
ISO-amp
filter
ADC

Figure 4.1: Characterization of the experimental setup. **(a)** Scanning electron micrograph of a device as used in the experiment (gates which are grounded are hidden). Gates T, M and R define the quantum dot (dotted circle), and gates R and Q form the QPC. Gate P is connected to a pulse source via a coaxial cable. See Ref. [8] for a more detailed description. **(b)** Schematic of the experimental set-up, including the most relevant noise sources. The QPC is represented by a resistor, R_Q. **(c)** Noise spectra measured when the IV-convertor is connected to the sample (top solid trace), and, for reference, to an open-ended 1 m twisted pair of wires (lower solid trace). The latter represents a 300 pF load, if we include the 200 pF measured amplifier input capacitance. The diagram also shows the calculated noise level for the 300 pF reference load (dotted-dashed) and the shot noise limit (dashed). The left and right axes express the noise in terms of current through the QPC and electron charge on the dot respectively.

convertor is based on a dual low-noise JFET (Interfet 3602). Finally, the signal is AC-coupled to an 8th-order elliptic low-pass filter (SRS650), and the current fluctuations, ΔI, are digitized at 2.2×10^6 14-bit samples per second (ADwin Gold).

The measurement bandwidth is limited by the low-pass filter formed by the capacitance of the line and Cu-powder filters, $C_L \approx 1.5$ nF, and the input impedance of the IV-convertor, $R_i = R_{FB}/A$. Thermal noise considerations (below) impose $R_{FB} = 10\,\mathrm{M}\Omega$. We choose the amplifier gain $A = 10000$, such that $1/(2\pi R_i C_L) \approx 100$ kHz. The bandwidth of the amplifier inside the IV-convertor is 500 kHz, and the output ISO-amp bandwidth is 300 kHz. However, we shall see that the true limitation to measurement speed is not the bandwidth but the signal-to-noise ratio.

4.3 Sensitivity and speed

The measured signal corresponding to a single electron charge on the dot amounts to $\Delta I \approx 0.3$ nA with the QPC biased at $V_i = 1$ mV, a 1% change in the overall current I ($I \approx 30$ nA, consistent with the series resistance of R_Q, $R_i = 1$ kΩ and the resistance of the Ohmic contacts of about 2 kΩ). Naturally, the signal strength is proportional to V_i, but we found that for $V_i \geq 1$ mV, the dot occupation was affected, possibly due to heating. We therefore proceed with the analysis using $I = 30$ nA and $\Delta I = 0.3$ nA.

The most relevant noise sources [10] are indicated in the schematic of Fig. 4.1b. In Table 4.1, we give an expression and value for each noise contribution in terms of rms current at the IV-convertor input, so it can be compared directly to the signal, ΔI. We also give the corresponding value for the rms charge noise on the quantum dot. Shot noise, I_{SN}, is intrinsic to the QPC and therefore unavoidable. Both I_{SN} and ΔI are zero at QPC transmission $T = 0$ or $T = 1$, and maximal at $T = 1/2$; here we use $T \leq 1/2$. The effect of thermal noise, V_T, can be kept small compared to other noise sources by choosing R_{FB} sufficiently large; here $R_{FB} = 10$ MΩ. The JFET input voltage noise is measured to be $V_A = 0.8$ nV/$\sqrt{\mathrm{Hz}}$. As a result of V_A, it is as if a noise current flows from the IV-convertor

noise	rms noise current		rms charge noise
source	expression	A/$\sqrt{\mathrm{Hz}}$	$e/\sqrt{\mathrm{Hz}}$
I_{SN}	$\sqrt{T(1-T)2eI}$	49×10^{-15}	1.6×10^{-4}
V_T	$\sqrt{4k_BT/R_{FB}}$	41×10^{-15}	1.4×10^{-4}
V_A	$V_A\frac{1+j2\pi f R_Q C_L}{R_Q}$		
V_A, low f	V_A/R_{FB}	32×10^{-15}	1.1×10^{-4}
V_A, high f	$V_A 2\pi f C_L$	$7.5 \times 10^{-18} f$	$2.5 \times 10^{-8} f$
I_A	I_A	-	-

Table 4.1: Contributions to the noise current at the IV-convertor input. By dividing the noise current by 300 pA (the signal corresponding to one electron charge leaving the dot), we obtain the rms charge noise on the dot.

input leg to ground, through the QPC in parallel with the line capacitance. Due to the capacitance, C_L, the rms noise current resulting from V_A increases with frequency; it equals ΔI at 120 kHz. There is no specification available for the JFET input current noise, I_A, but usually I_A is small in JFETs.

We summarize the expected noise spectrum in Fig. 4.1c, and compare this with the measured noise spectrum in the same figure. For a 300 pF reference load, the noise level measured below a few kHz is 52 fA/$\sqrt{\text{Hz}}$, close to the noise current due to V_T, as expected; at high frequencies, the measured noise level is significantly higher than would be caused by V_A in combination with the 300 pF load, and appears to be dominated by I_A. With the sample connected, we observe substantial $1/f^2$ noise ($1/f$ in the noise amplitude), presumably from spurious charge fluctuations near the QPC, as well as interference at various frequencies. Near 100 kHz, the spectrum starts to roll off because of the 100 kHz low-pass filter formed by $C_L = 1.5$ nF and $R_i = 1$ kΩ (for the reference load, C_L is only 300 pF so the filter cut-off is at 500 kHz).

From the data, we see that the measured charge noise integrated from DC is comparable to e at 80 kHz, and 2.5 times smaller than e around 40 kHz. We set the cut-off frequency of the external low-pass filter at 40 kHz, so we should see clear steps in time traces of the QPC current, corresponding to single electrons tunneling on or off the dot.

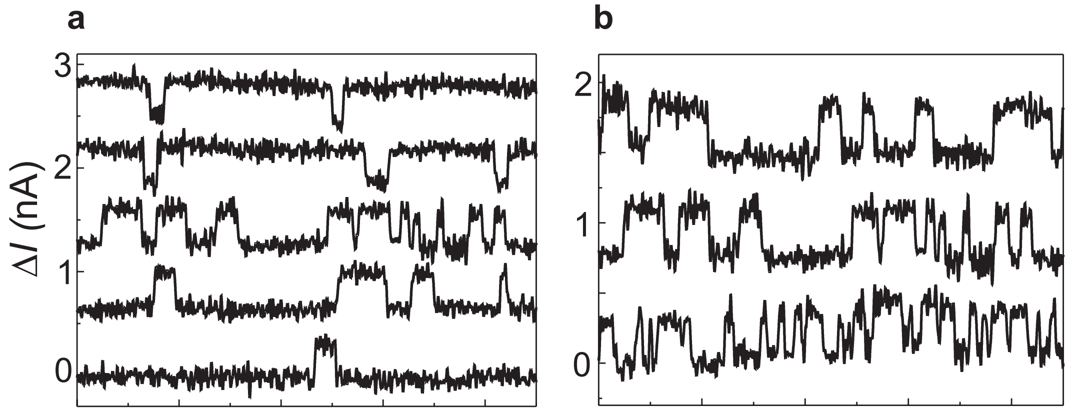

Figure 4.2: Measured changes in the QPC current, ΔI, with the electrochemical potential in the dot and in the reservoir nearly equal. ΔI is 'high' and 'low' for 0 and 1 electrons on the dot respectively ($V_i = 1$ mV; the steps in ΔI are ≈ 300 pA). Traces are offset for clarity. **(a)** The dot potential is lowered from top to bottom. **(b)** The tunnel barrier is lowered from top to bottom.

4.4 Real-time single electron tunneling

We test this experimentally, in the regime where the electrochemical potential in the dot is nearly lined up with the electrochemical potential in the reservoir. The electron can then *spontaneously* tunnel back and forth between the dot and the reservoir, and the QPC current should exhibit a random telegraph signal (RTS). This is indeed what we observe experimentally (Fig. 4.2). In order to ascertain that the RTS really originates from electron tunnel events between the dot and the reservoir, we verify that (1) the dot potential relative to the Fermi level determines the fraction of the time an electron resides in the dot (Fig. 4.2a) and (2) the dot-reservoir tunnel barrier sets the RTS frequency (Fig. 4.2b). The shortest steps that clearly reach above the noise level are about 8 μs long. This is consistent with the 40 kHz filter frequency, which permits a rise time of 8 μs.

Next, we *induce* tunnel events by pulsing the dot potential, so N predictably changes from 0 to 1 and back to 0. The response of the QPC current to such a pulse contains two contributions (Fig. 4.3a). First, the shape of the pulse is reflected in ΔI, as the pulse gate couples capacitively to the QPC. Second, some time after the pulse is started, an electron tunnels into the dot and ΔI goes down by about 300 pA. Similarly, ΔI goes up by 300 pA when an electron leaves the dot, some time after the pulse ends. We observe that the time before tunneling takes place is randomly distributed, and obtain a histogram of this time simply by averaging over many single-shot traces (Fig. 4.3b). The measured distribution

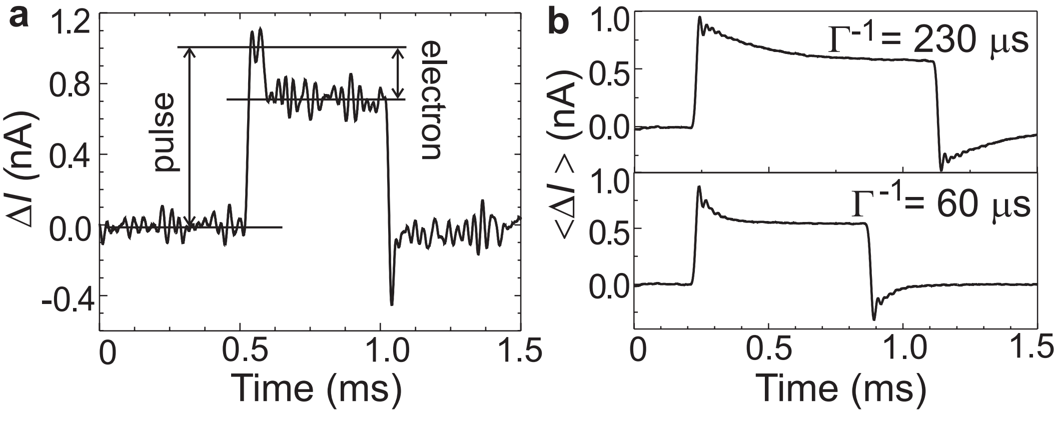

Figure 4.3: QPC pulse response. **(a)** Measured changes in the QPC current, ΔI, when a pulse is applied to gate P, near the degeneracy point between 0 and 1 electrons on the dot ($V_i = 1$ mV). **(b)** Average of 286 traces as in (a). The top and bottom panel are taken with a different setting of gate M. The damped oscillation following the pulse edges is due to the 8th-order 40 kHz filter.

decays exponentially with the tunnel time, characteristic of a Poisson process. The average time before tunneling corresponds to Γ^{-1}, and can be tuned by adjusting the tunnel barrier.

4.5 QPC *vs.* SET

Our measurements clearly demonstrate that a QPC can serve as a fast and sensitive charge detector. Compared to an SET, a QPC offers several practical advantages. First, a QPC requires fabrication and tuning of just a single additional gate when integrated with a quantum dot defined by metal gates, whereas an SET requires two tunnel barriers, and a gate to set the island potential. Second, QPCs are more robust and easy to use in the sense that spurious, low-frequency fluctuations of the electrostatic potential hardly change the QPC sensitivity to charges on the dot (the transition between quantized conductance plateaus has an almost constant slope over a wide range of electrostatic potential), but can easily spoil the SET sensitivity.

With an RF-SET, a sensitivity to charges on a quantum dot of $\approx 2 \times 10^{-4} e/\sqrt{\text{Hz}}$ has been reached [3], and theoretically even a ten times better sensitivity is possible [2]. Could a QPC reach similar sensitivities?

The noise level in the present measurement could be reduced by a factor of two or three using a JFET input-stage which better balances input voltage noise and input current noise. Further improvements can be obtained by lowering the capacitance of the filters in the line, or the line capacitance itself, by placing the IV-convertor close to the sample, inside the refrigerator.

Much more significant reductions in the instrumentation noise could be realized by embedding the QPC in a resonant electrical circuit and measuring the damping of the resonator. We estimate that with an ‘RF-QPC’ and a low-temperature HEMT amplifier, a sensitivity of $2 \times 10^{-4} e/\sqrt{\text{Hz}}$ could be achieved with the present sample. The noise from the amplifier circuitry is then only 2.5 times larger than the shot noise level.

To what extent the signal can be increased is unclear, as we do not yet understand the mechanism through which the dot occupancy is disturbed for $V_i > 1$ mV [12]. Certainly, the capacitive coupling of the dot to the QPC channel can easily be five times larger than it is now by optimizing the gate design [6]. Keeping $V_i = 1$ mV , the sensitivity would then be $4 \times 10^{-5} e/\sqrt{\text{Hz}}$, and a single electron charge on the dot could be measured within a few ns.

Finally, we point out that a QPC can reach the quantum limit of detection [11], where the measurement induced decoherence takes the minimum value permitted by quantum mechanics. Qualitatively, this is because (1) information on the charge state of the dot is transferred only to the QPC current and not to degrees of freedom which are not observed, and (2) an external perturbation in the QPC current does not couple back to the charge state of the dot.

We thank R. Schoelkopf, K. Schwab and K. Harmans for useful discussions, T. Fujisawa T. Hayashi, T. Saku and Y. Hirayama for help with device fabrication, and the DARPA-QUIST program, the ONR, the EU-RTN network on spintronics, and the Dutch Organisation for Fundamental Research on Matter (FOM) for financial support.

References

[1] T.A. Fulton and G.J. Dolan, Phys. Rev. Lett. **59**, 109 (1987).

[2] R.J. Schoelkopf, P. Wahlgren, A.A. Kozhevnikov, P. Delsing, and D.E. Prober, Science **280**, 1238 (1998).

[3] W. Lu, Z. Ji, L. Pfeiffer, K.W. West, and A.J. Rimberg, Nature **423**, 422 (2003).

[4] T. Fujisawa, T. Hayashi, Y. Hirayama, H.D Cheong and Y.H. Jeong, Appl. Phys. Lett. **84**, 2343 (2004).

[5] M. Field, C.G. Smith, M. Pepper, D.A. Richie, J.E.F. Frost, G.A.C. Jones, and D.G. Hasko, Phys. Rev. Lett. **70**, 1311 (1993).

[6] J. Cooper, C.G. Smith, D.A. Ritchie, E.H. Linfield, Y. Jin, and H. Launois, Phys. E **6**, 457 (2000).

[7] R. Schleser, E. Ruh, T. Ihn, K. Ennslin, D.C. Driscoll, and A.C. Gossard, cond-mat/0406568.

[8] J.M. Elzerman, R. Hanson, J.S. Greidanus, L.H. Willems van Beveren, S. De Franceschi, L.M.K. Vandersypen, S. Tarucha, and L.P. Kouwenhoven, Phys. Rev. B **67**, 161308 (2003).

[9] Despite a $B = 10$ T field in the plane of the 2DEG, no spin-split plateau is visible.

[10] P. Horowitz and W. Hill, The Art of Electronics (Cambridge University Press, Cambridge, UK, 1989).

[11] A.N. Korotkov, Phys. Rev. B **60**, 5737 (1999); A.A. Clerk, S.M. Girvin and A.D. Stone, Phys. Rev. B **67**, 165324 (2003).

[12] The statistics of the RTS were altered for $V_i > 1$ mV, irrespective of (1) whether V_i was applied to the QPC source or drain, (2) the potential difference between the reservoir and the QPC source/drain, and (3) the QPC transmission T.

Chapter 5

Single-shot read-out of an individual electron spin in a quantum dot

J. M. Elzerman, R. Hanson, L. H. Willems van Beveren,
B. Witkamp, L. M. K. Vandersypen and L. P. Kouwenhoven

Spin is a fundamental property of all elementary particles. Classically it can be viewed as a tiny magnetic moment, but a measurement of an electron spin along the direction of an external magnetic field can have only two outcomes [1]: parallel or anti-parallel to the field. This discreteness reflects the quantum mechanical nature of spin. Ensembles of many spins have found diverse applications ranging from magnetic resonance imaging [2] to magneto-electronic devices [3], while individual spins are considered as carriers for quantum information. Read-out of single spin states has been achieved using optical techniques [4], and is within reach of magnetic resonance force microscopy [5]. However, electrical read-out of single spins [6, 7, 8, 9, 10, 11, 12, 13] has so far remained elusive. Here, we demonstrate electrical single-shot measurement of the state of an individual electron spin in a semiconductor quantum dot [14]. We use spin-to-charge conversion of a single electron confined in the dot, and detect the single-electron charge using a quantum point contact; the spin measurement visibility is $\sim 65\%$. Furthermore, we observe very long single-spin energy relaxation times (up to ~ 0.85 ms at a magnetic field of 8 Tesla), which are encouraging for the use of electron spins as carriers of quantum information.

This chapter has been published in Nature **430**, 431 (2004).

5.1 Measuring electron spin in quantum dots

In quantum dot devices, single electron charges are easily measured. Spin states in quantum dots, however, have only been studied by measuring the average signal from a large ensemble of electron spins [17, 18, 19, 20, 21, 22]. In contrast, the experiment presented here aims at a single-shot measurement of the spin orientation (parallel or antiparallel to the field, denoted as spin-$\uparrow$ and spin-$\downarrow$, respectively) of a particular electron; only one copy of the electron is available, so no averaging is possible. The spin measurement relies on spin-to-charge conversion [20, 21] followed by charge measurement in a single-shot mode [15, 16]. Fig. 5.1a schematically shows a single electron spin confined in a quantum dot (circle). A magnetic field is applied to split the spin-$\uparrow$ and spin-$\downarrow$ states by the Zeeman energy. The dot potential is then tuned such that if the electron has spin-$\downarrow$ it will leave, whereas it will stay on the dot if it has spin-$\uparrow$. The spin state has now been correlated with the charge state, and measurement of the charge on the dot will reveal the original spin state.

5.2 Implementation

This concept is implemented using a structure [23] (Fig. 5.1b) consisting of a quantum dot in close proximity to a quantum point contact (QPC). The quantum dot is used as a box to trap a single electron, and the QPC is operated as a charge detector in order to determine whether the dot contains an electron or not. The quantum dot is formed in the two-dimensional electron gas (2DEG) of a GaAs/AlGaAs heterostructure by applying negative voltages to the metal surface gates M, R, and T. This depletes the 2DEG below the gates and creates a potential minimum in the centre, that is, the dot (indicated by a dotted white circle). We tune the gate voltages such that the dot contains either zero or one electron (which we can control by the voltage applied to gate P). Furthermore, we make the tunnel barrier between gates R and T sufficiently opaque that the dot is completely isolated from the drain contact on the right. The barrier to the reservoir on the left is set [24] to a tunnel rate $\Gamma \approx (0.05 \text{ ms})^{-1}$. When an electron tunnels on or off the dot, it changes the electrostatic potential in its vicinity, including the region of the nearby QPC (defined by R and Q). The QPC is set in the tunnelling regime, so that the current, I_{QPC}, is very sensitive to electrostatic changes [25]. Recording changes in I_{QPC} thus permits us to measure on a timescale of about 8 μs whether an electron resides on the dot or not (L.M.K.V. *et al.*, see chapter 4). In this way the QPC is used as a charge detector with a resolution much better than a single electron charge and a measurement

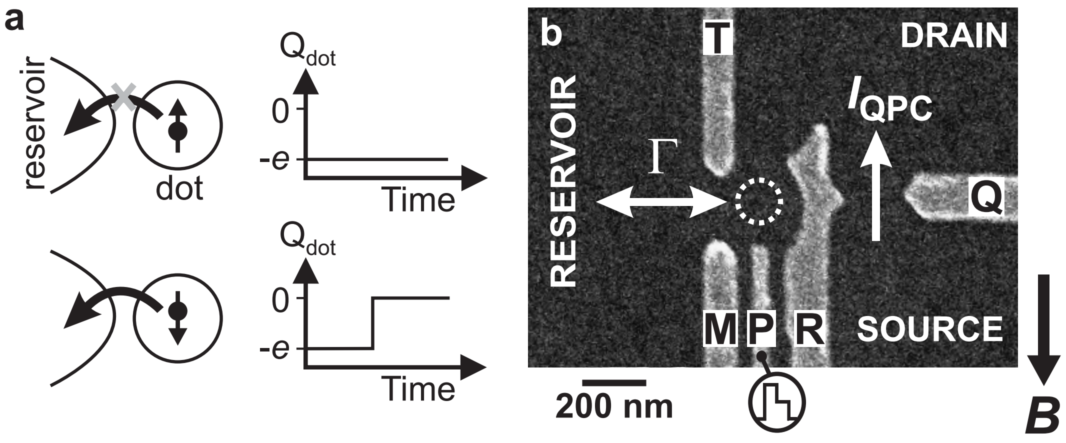

Figure 5.1: Spin-to-charge conversion in a quantum dot coupled to a quantum point contact. **(a)** Principle of spin-to-charge conversion. The charge on the quantum dot, Q_{dot}, remains constant if the electron spin is ↑, whereas a spin-↓ electron can escape, thereby changing Q_{dot}. **(b)** Scanning electron micrograph of the metallic gates on the surface of a GaAs/$Al_{0.27}Ga_{0.73}As$ heterostructure containing a two-dimensional electron gas (2DEG) 90 nm below the surface. The electron density is 2.9×10^{15} m^{-2}. (Only the gates used in the present experiment are shown, the complete device is described in Ref. [23].) Electrical contact is made to the QPC source and drain and to the reservoir via Ohmic contacts. With a source-drain bias voltage of 1 mV, I_{QPC} is about 30 nA, and an individual electron tunnelling on or off the dot changes I_{QPC} by ~ 0.3 nA. The QPC-current is sent to a room temperature current-to-voltage convertor, followed by a gain 1 isolation amplifier, an AC-coupled 40 kHz SRS650 low-pass filter, and is digitized at a rate of 2.2×10^6 samples/s. With this arrangement, the step in I_{QPC} resulting from an electron tunnelling is clearly larger than the rms noise level, provided it lasts at least 8 μs. A magnetic field, B, is applied in the plane of the 2DEG.

timescale almost ten times shorter than $1/\Gamma$.

The device is placed inside a dilution refrigerator, and is subject to a magnetic field of 10 T (unless noted otherwise) in the plane of the 2DEG. The measured Zeeman splitting in the dot [21], $\Delta E_Z \approx 200\mu\text{eV}$, is larger than the thermal energy (25 μeV) but smaller than the orbital energy level spacing (1.1 meV) and the charging energy (2.5 meV).

5.3 Two-level pulse technique

To test our single-spin measurement technique, we use an experimental procedure based on three stages: 1) empty the dot, 2) inject one electron with unknown spin, and 3) measure its spin state. The different stages are controlled by voltage

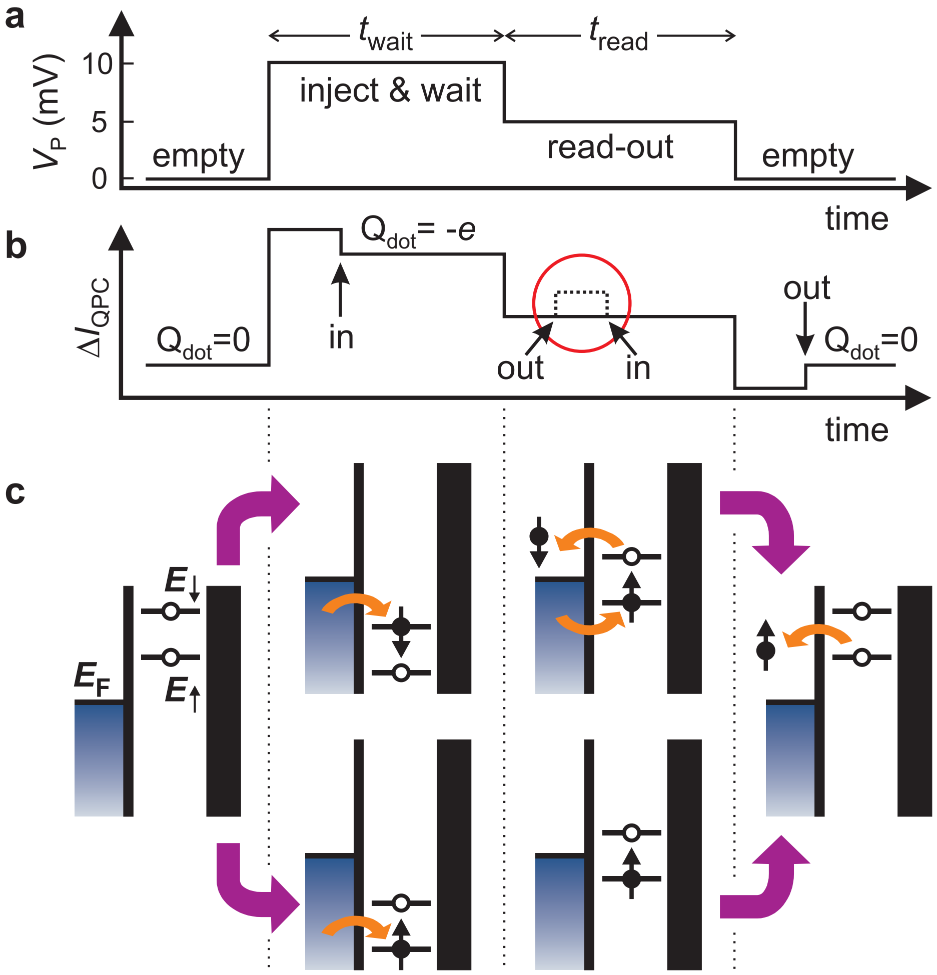
a
t_{wait}
t_{read}
V_P (mV)
10
5
0
empty
inject & wait
read-out
empty
time
b
ΔI_{QPC}
Q_{dot}=0
in
Q_{dot}= -e
out
in
out
Q_{dot}=0
time
c
$E_\downarrow$
E_F
$E_\uparrow$

Figure 5.2: Two-level pulse technique used to inject a single electron and measure its spin orientation. **(a)** Shape of the voltage pulse applied to gate P. The pulse level is 10 mV during t_{wait} and 5 mV during t_{read} (which is 0.5 ms for all measurements). **(b)** Schematic QPC pulse-response if the injected electron has spin-↑ (solid line) or spin-↓ (dotted line; the difference with the solid line is only seen during the read-out stage). Arrows indicate the moment an electron tunnels into or out of the quantum dot. **(c)** Schematic energy diagrams for spin-↑ ($E_\uparrow$) and spin-↓ ($E_\downarrow$) during the different stages of the pulse. Black vertical lines indicate the tunnel barriers. The tunnel rate between the dot and the QPC-drain on the right is set to zero. The rate between the dot and the reservoir on the left is tuned to a specific value, Γ. If the spin is ↑ at the start of the read-out stage, no change in the charge on the dot occurs during t_{read}. In contrast, if the spin is ↓, the electron can escape and be replaced by a spin-↑ electron. This charge transition is detected in the QPC-current (dotted line inside red circle in (b)).

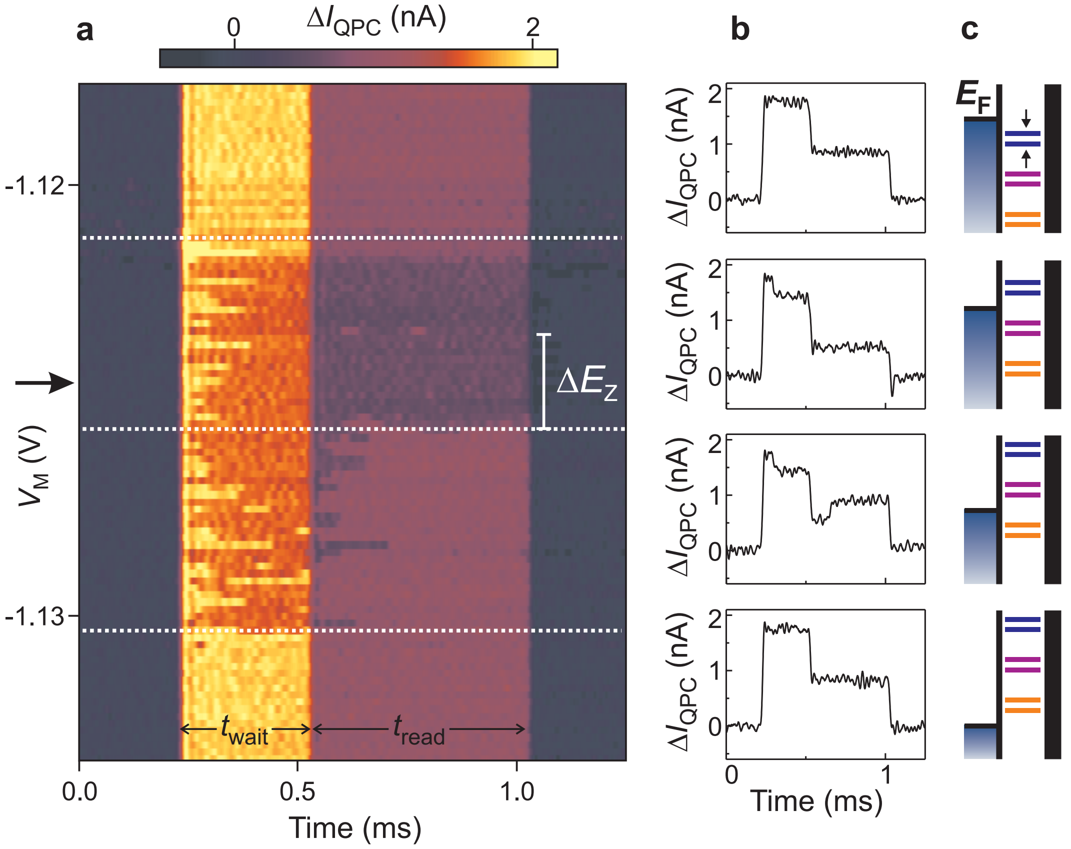

Figure 5.3: Tuning the quantum dot into the spin read-out configuration. We apply a two-stage voltage pulse as in Fig. 5.2a ($t_{wait} = 0.3$ ms, $t_{read} = 0.5$ ms), and measure the QPC-response for increasingly negative values of V_M. **(a)** QPC-response (in colour-scale) versus V_M. Four different regions in V_M can be identified (separated by white dotted lines), with qualitatively different QPC-responses. **(b)** Typical QPC-response in each of the four regions. This behaviour can be understood from the energy levels during all stages of the pulse. **(c)** Schematic energy diagrams showing $E_\uparrow$ and $E_\downarrow$ with respect to E_F before and after the pulse (blue), during t_{wait} (orange) and during t_{read} (purple), for four values of V_M. For the actual spin read-out experiment, V_M is set to the optimum position (indicated by the arrow in a).

pulses on gate P (Fig. 5.2a), which shift the dot's energy levels (Fig. 5.2c). Before the pulse the dot is empty, as both the spin-↑ and spin-↓ levels are above the Fermi energy of the reservoir, E_F. Then a voltage pulse pulls both levels below E_F. It is now energetically allowed for an electron to tunnel onto the dot, which will happen after a typical time $\sim \Gamma^{-1}$. The particular electron can have spin-↑ (shown in the lower diagram) or spin-↓ (upper diagram). (The tunnel rate for spin-↑ electrons is expected to be larger than that for spin-↓ electrons [26], i.e.

$\Gamma_\uparrow > \Gamma_\downarrow$, but we do not assume this a priori.) During this stage of the pulse, lasting t_{wait}, the electron is trapped on the dot and Coulomb blockade prevents a second electron to be added. After t_{wait} the pulse is reduced, in order to position the energy levels in the read-out configuration. If the electron spin is ↑, its energy level is below E_F, so the electron remains on the dot. If the spin is ↓, its energy level is above E_F, so the electron tunnels to the reservoir after a typical time $\sim \Gamma_\downarrow^{-1}$. Now Coulomb blockade is lifted and an electron with spin-↑ can tunnel onto the dot. This occurs on a timescale $\sim \Gamma_\uparrow^{-1}$ (with $\Gamma = \Gamma_\uparrow + \Gamma_\downarrow$). After t_{read}, the pulse ends and the dot is emptied again.

The expected QPC-response, ΔI_{QPC}, to such a two-level pulse is the sum of two contributions (Fig. 5.2b). First, due to a capacitive coupling between pulse-gate and QPC, ΔI_{QPC} will change proportionally to the pulse amplitude. Thus, ΔI_{QPC} versus time resembles a two-level pulse. Second, ΔI_{QPC} tracks the charge on the dot, i.e. it goes up whenever an electron tunnels off the dot, and it goes down by the same amount when an electron tunnels on the dot. Therefore, if the dot contains a spin-↓ electron at the start of the read-out stage, ΔI_{QPC} should go up and then down again. We thus expect a characteristic step in ΔI_{QPC} during t_{read} for spin-↓ (dotted trace inside red circle). In contrast, ΔI_{QPC} should be flat during t_{read} for a spin-↑ electron. Measuring whether a step is present or absent during the read-out stage constitutes our spin measurement.

5.4 Tuning the quantum dot into the read-out configuration

To perform spin read-out, V_M has to be fine-tuned so that the position of the energy levels with respect to E_F is as shown in Fig. 5.2c. To find the correct settings, we apply a two-level voltage pulse and measure the QPC-response for increasingly negative values of V_M (Fig. 5.3a). Four different regions in V_M can be identified (separated by white dotted lines), with qualitatively different QPC-responses. The shape of the typical QPC-response in each of the four regions (Fig. 5.3b) allows us to infer the position of $E_\uparrow$ and $E_\downarrow$ with respect to E_F during all stages of the pulse (Fig. 5.3c).

In the top region, the QPC-response just mimics the applied two-level pulse, indicating that here the charge on the dot remains constant throughout the pulse. This implies that $E_\uparrow$ remains below E_F for all stages of the pulse, thus the dot remains occupied with one electron. In the second region from the top, tunnelling occurs, as seen from the extra steps in ΔI_{QPC}. The dot is empty before the pulse, then an electron is injected during t_{wait}, which escapes after the pulse. This corresponds to an energy level diagram similar to before, but with $E_\uparrow$ and $E_\downarrow$ shifted up due to the more negative value of V_M in this region. In the third region from the top, an electron again tunnels on the dot during t_{wait}, but now it can escape already during t_{read}, irrespective of its spin. Finally, in the bottom region no electron-tunneling is seen, implying that the dot remains empty throughout the pulse.

Since we know the shift in V_M corresponding to shifting the energy levels by ΔE_Z, we can set V_M to the optimum position for the spin read-out experiment (indicated by the arrow). For this setting, the energy levels are as shown in Fig. 5.2c, i.e. E_F is approximately in the middle between $E_\uparrow$ and $E_\downarrow$ during the read-out stage.

5.5 Single-shot read-out of one electron spin

Fig. 5.4a shows typical experimental traces of the pulse-response recorded after proper tuning of the DC gate voltages (see Fig. 5.3). We emphasize that each trace involves injecting one particular electron on the dot and subsequently measuring its spin state. Each trace is therefore a single-shot measurement. The traces we obtain fall into two different classes; most traces qualitatively resemble the one in the top panel of Fig. 5.4a, some resemble the one in the bottom panel. These two typical traces indeed correspond to the signals expected for a spin-↑ and a spin-↓ electron (Fig. 5.2b), a strong indication that the electron in the top panel of Fig. 5.4a was spin-↑ and in the bottom panel spin-↓. The distinct signature of the two types of responses in ΔI_{QPC} permits a simple criterion for identifying the spin [27]: if ΔI_{QPC} goes above the threshold value (red line in Fig. 5.4a and chosen as explained below), we declare the electron ‘spin-down’; otherwise we declare it ‘spin-up’. Fig. 5.4b shows the read-out section of twenty more ‘spin-down’ traces, to illustrate the stochastic nature of the tunnel events.

The random injection of spin-↑ and spin-↓ electrons prevents us from checking the outcome of any individual measurement. Therefore, in order to further establish the correspondence between the actual spin state and the outcome of our spin measurement, we change the probability to have a spin-↓ at the beginning of the read-out stage, and compare this with the fraction of traces in which the electron is declared ‘spin-down’. As t_{wait} is increased, the time between injection and read-out, t_{hold}, will vary accordingly ($t_{hold} \approx t_{wait}$). The probability for the spin to be ↓ at the start of t_{read} will thus decay exponentially to zero, since electrons in the excited spin state will relax to the ground state ($k_BT << \Delta E_Z$). For a set of 15 values of t_{wait} we take 625 traces for each t_{wait}, and count the

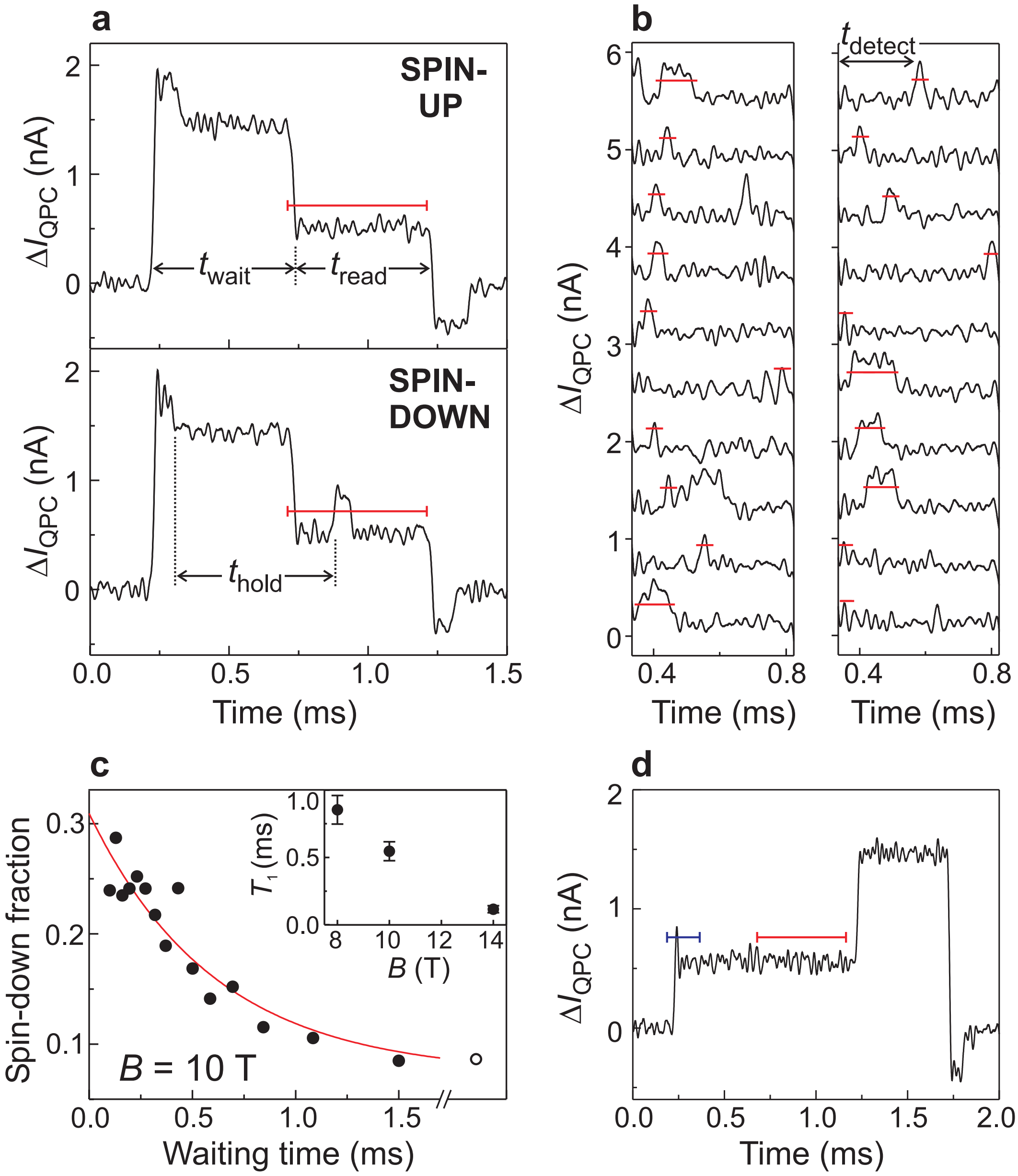

Figure 5.4: Single-shot read-out of one electron spin. **(a)** Time-resolved QPC measurements. Top panel: an electron injected during t_{wait} is declared 'spin-up' during t_{read}. Bottom panel: the electron is declared 'spin-down'. **(b)** Examples of 'spin-down' traces (for $t_{wait} = 0.1$ ms). Only the read-out segment is shown, and traces are offset for clarity. The time when ΔI_{QPC} first crosses the threshold, t_{detect}, is recorded to make the histogram in Fig. 5.7a. **(c)** Fraction of 'spin-down' traces versus t_{wait}, out of 625 traces for each waiting time. Open dot: spin-down fraction using modified pulse shape (d). Red solid line: exponential fit to the data. Inset: T_1 versus B. **(d)** Typical QPC-signal for a 'reversed' pulse, with the same amplitudes as in Fig. 5.2a, but a reversed order of the two stages. The blue threshold is used in Fig. 5.7b

.

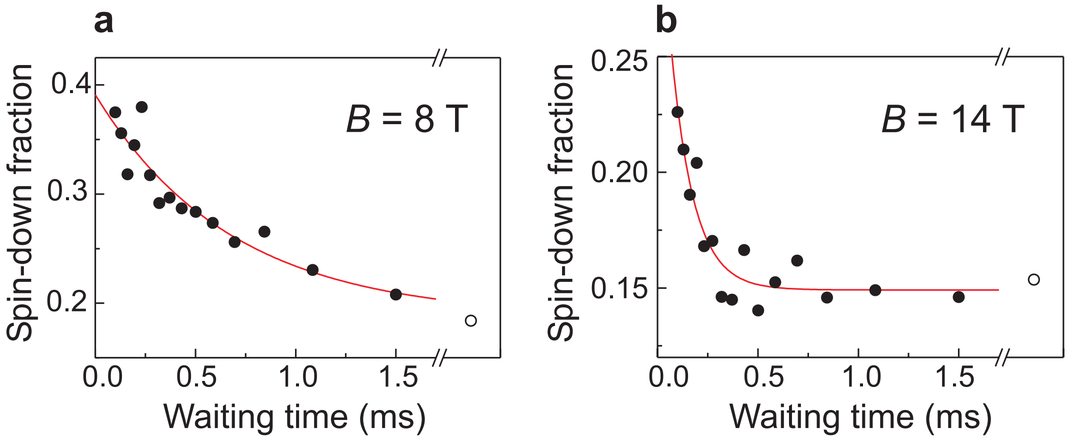

Figure 5.5: Measurement of the spin-relaxation time as in Fig. 5.4c, but at different magnetic fields. Averaging the results of an exponential fit (as shown) over three similar measurements yields **(a)**, $T_1 = (0.85 \pm 0.11)$ ms at 8 T and **(b)**, $T_1 = (0.12 \pm 0.03)$ ms at 14 T.

fraction of traces in which the electron is declared 'spin-down' (Fig. 5.4c). The fact that the expected exponential decay is clearly reflected in the data confirms the validity of the spin read-out procedure.

We extract a single-spin energy relaxation time, T_1, from fitting the datapoints in Fig. 5.4c (and two other similar measurements) to $\alpha + C\exp(-t_{wait}/T_1)$, and obtain an average value of $T_1 \approx (0.55 \pm 0.07)$ ms at 10 Tesla. This is an order of magnitude longer than the lower bound on T_1 established earlier [21], and clearly longer than the time needed for the spin measurement (of order $1/\Gamma_\downarrow \approx 0.11$ ms). A similar experiment at 8 Tesla gives $T_1 \approx (0.85 \pm 0.11)$ ms and at 14 Tesla we find $T_1 \approx (0.12 \pm 0.03)$ ms (Fig. 5.5). More experiments are needed in order to test the theoretical prediction that relaxation at high magnetic fields is dominated by spin-orbit interactions [28, 29, 30], with smaller contributions resulting from hyperfine interactions with the nuclear spins [28, 31] (cotunnelling is insignificant given the very small tunnel rates). We note that the obtained values for T_1 refer to our entire device under active operation: i.e. a single spin in a quantum dot subject to continuous charge detection by a QPC.

5.6 Measurement fidelity

For applications in quantum information processing it is important to know the accuracy, or fidelity, of the single-shot spin read-out. The measurement fidelity is characterised by two parameters, α and β (inset to Fig. 5.7a), which we now

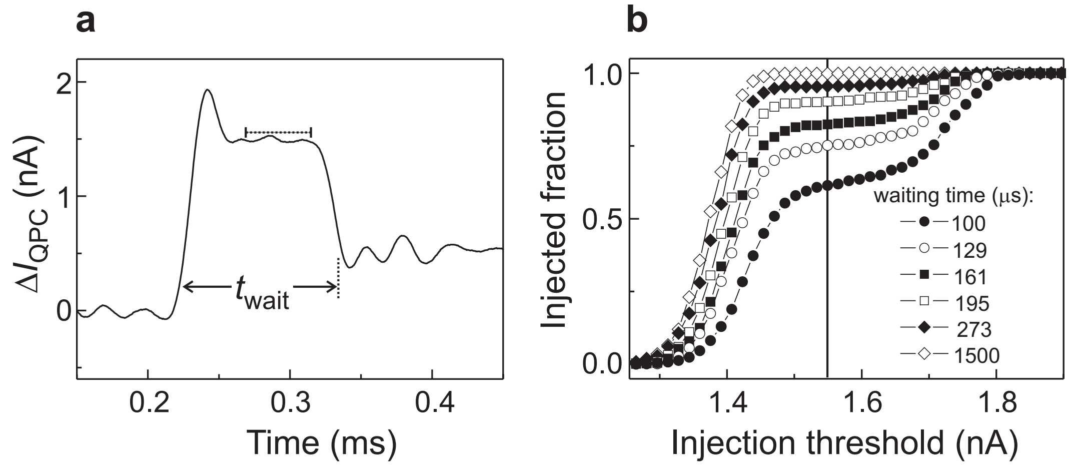

Figure 5.6: Setting the injection threshold. **(a)** Example of QPC-signal for the shortest waiting time used (0.1 ms). The dotted horizontal line indicates the injection threshold. Injection is declared successful if the QPC-signal is below the injection threshold for a part or all of the last 45 μs before the end of the injection stage (t_{wait}). Traces in which injection was not successful, i.e. no electron was injected during t_{wait}, are disregarded. **(b)** Fraction of traces in which injection was successful, out of a total of 625 taken for each waiting time. The threshold chosen for analysing all data is indicated by the vertical line.

determine for the data taken at 10 T.

The parameter α corresponds to the probability that the QPC-current exceeds the threshold even though the electron was actually spin-↑, for instance due to thermally activated tunnelling or electrical noise (similar to 'dark counts' in a photon detector). The combined probability for such processes is given by the saturation value of the exponential fit in Fig. 5.4c, α, which depends on the value of the threshold current. We analyse the data in Fig. 5.4c using different thresholds, and plot α in Fig. 5.7b.

The parameter β corresponds to the probability that the QPC-current stays below the threshold even though the electron was actually spin-↓ at the start of the read-out stage. Unlike α, β cannot be extracted directly from the exponential fit (note that the fit parameter $C = p(1-\alpha-\beta)$ contains two unknowns: $p = \Gamma_\downarrow/(\Gamma_\uparrow+\Gamma_\downarrow)$ and β). We therefore estimate β by analysing the two processes that contribute to it. First, a spin-↓ electron can relax to spin-↑ before spin-to-charge conversion takes place. This occurs with probability $\beta_1 = 1/(1+T_1\Gamma_\downarrow)$. From a histogram (Fig. 5.7a) of the actual detection time, t_{detect} (see Fig. 5.4b), we find $\Gamma_\downarrow^{-1} \approx 0.11$ ms, yielding $\beta_1 \approx 0.17$. Second, if the spin-↓ electron does tunnel off the dot but is replaced by a spin-↑ electron within about 8 μs, the resulting

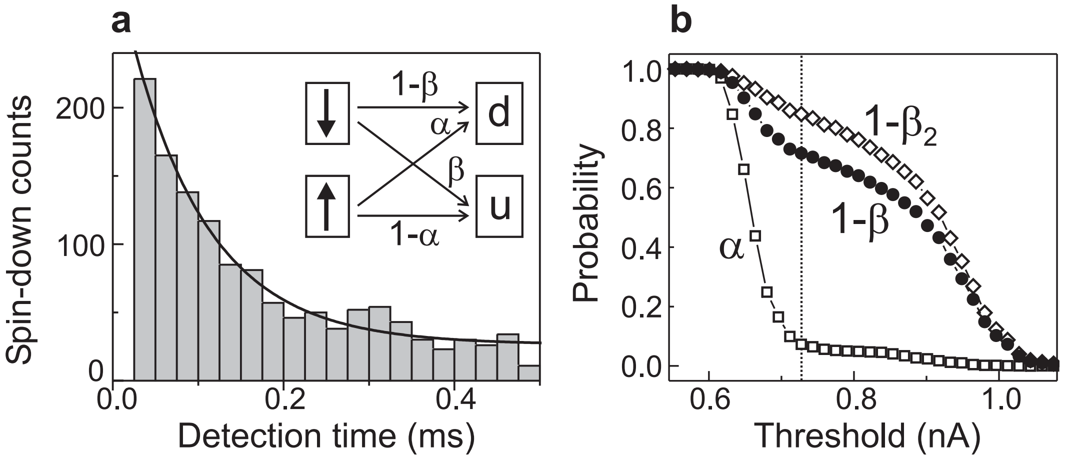

Figure 5.7: Measurement fidelity. **(a)** Histogram showing the distribution of detection times, t_{detect}, in the read-out stage (see Fig. 5.4b for definition t_{detect}). The exponential decay is due to spin-↓ electrons tunnelling out of the dot (rate = $\Gamma_{\downarrow}$) and due to spin flips during the read-out stage (rate = $1/T_1$). Solid line: exponential fit with a decay time $(\Gamma_{\downarrow} + 1/T_1)^{-1}$ of 0.09 ms. Given that $T_1 = 0.55$ ms, this yields $\Gamma_{\downarrow}^{-1} \approx 0.11$ ms. Inset: fidelity parameters. A spin-↓ electron is declared 'down' (d) or 'up' (u) with probability $1 - \beta$ or β, respectively. A spin-↑ electron is declared 'up' or 'down' with probability $1 - \alpha$ or α, respectively. **(b)** Open squares represent α, obtained from the saturation value of exponential fits as in Fig. 5.4c for different values of the read-out threshold. A current of 0.54 nA (0.91 nA) corresponds to the average value of ΔI_{QPC} when the dot is occupied (empty) during t_{read}. Open diamonds: measured fraction of 'reverse-pulse' traces in which ΔI_{QPC} crosses the injection threshold (blue line in Fig. 5.4d). This fraction approximates $1-\beta_2$, where β_2 is the probability of identifying a spin-↓ electron as 'spin-up' due to the finite bandwidth of the measurement setup. Filled circles: total fidelity for the spin-↓ state, $1 - \beta$, calculated using $\beta_1 = 0.17$. The vertical dotted line indicates the threshold for which the visibility $1-\alpha-\beta$ (separation between filled circles and open squares) is maximal. This threshold value of 0.73 nA is used in the analysis of Fig. 5.4.

QPC-step is too small to be detected. The probability that a step is missed, β_2, depends on the value of the threshold. It can be determined by applying a modified ('reversed') pulse (Fig. 5.4d). For such a pulse, we know that in each trace an electron is injected in the dot, so there should always be a step at the start of the pulse. The fraction of traces in which this step is nevertheless missed, i.e. ΔI_{QPC} stays below the threshold (blue line in Fig. 5.4d), gives β_2. We plot $1-\beta_2$ in Fig. 5.7b (open diamonds). The resulting total fidelity for spin-↓ is given by $1 - \beta \approx (1 - \beta_1)(1 - \beta_2) + (\alpha\beta_1)$. The last term accounts for the case when a spin-↓ electron is flipped to spin-↑, but there is nevertheless a step in ΔI_{QPC} due to the dark-count mechanism [32]. In Fig. 5.7b we also plot the extracted value of $1-\beta$ as a function of the threshold.

We now choose the optimal value of the threshold as the one for which the visibility $1-\alpha-\beta$ is maximal (dotted vertical line in Fig. 5.7b). For this setting, $\alpha \approx 0.07$, $\beta_1 \approx 0.17$, $\beta_2 \approx 0.15$, so the measurement fidelity for the spin-↑ and the spin-↓ state is ∼ 0.93 and ∼ 0.72 respectively. The measurement visibility in a single-shot measurement is thus at present 65%.

Significant improvements in the spin measurement visibility can be made by lowering the electron temperature (smaller α) and especially by making the charge measurement faster (smaller β). Already, the demonstration of single-shot spin read-out and the observation of T_1 of order 1 ms are encouraging results for the use of electron spins as quantum bits.

We thank D. P. DiVincenzo, H. A. Engel, T. Fujisawa, V. Golovach, Y. Hirayama, D. Loss, T. Saku, R. Schouten, and S. Tarucha for technical support and helpful discussions. This work was supported by a Specially Promoted Research Grant-in-Aid from the Japanese Ministry of Education, the DARPA-QUIST program, the ONR, the EU-RTN network on spintronics, and the Dutch Organisation for Fundamental Research on Matter (FOM).

References

[1] Sakurai, J. J. Modern Quantum Mechanics. Addison-Wesley (Reading MA, USA, 1994).

[2] Wehrli, F. W. The origins and nature of nuclear magnetic resonance imaging. Physics Today **6**, 34 (1992).

[3] Wolf, S. A. et al. Spintronics: a spin-based electronics vision for the future. Science **294**, 1488-1495 (2001).

[4] Blatt, R. and Zoller, P. Quantum Jumps. Eur. J. Phys. **9**, 250-279 (1988).

[5] Mamin, H. J., Budakian, R., Chui, B. W. and Rugar, D. Detection and manipulation of statistical polarization in small spin ensembles. Phys. Rev. Lett. **91**, 207604 (2003).

[6] Loss, D. and DiVincenzo, D. P. Quantum computation with quantum dots. Phys. Rev. A **57**, 120-126 (1998).

[7] Kane, B. E. A silicon-based nuclear spin quantum computer. Nature **393**, 133-137 (1998).

[8] Vandersypen, L. M. K. et al. Quantum computing with electron spins in quantum dots, in Quantum Computing and Quantum Bits in Mesoscopic Systems, Kluwer Academic/Plenum Publishers (New York, 2003). See also http://xxx.lanl.gov/abs/quant-ph/0207059 (2002).

[9] Xiao, M., Martin, I. and Jiang, H. W. Probing the spin state of a single electron trap by random telegraph signal. Phys. Rev. Lett. **91**, 078301 (2003).

[10] Friesen, M., Tahan, C., Joynt, R., and Eriksson, M. A. Spin readout and initialization in a semiconductor quantum dot. Phys. Rev. Lett. **92**, 037901 (2004).

[11] Engel, H. et al. Measurement efficiency and n-shot read out of spin qubits. http://xxx.lanl.gov/abs/cond-mat/0309023 (2003).

[12] Ionicioiu, R. and Popescu, A. E. Single spin measurement using spin-orbital entanglement. http://xxx.lanl.gov/abs/quant-ph/0310047 (2003).

[13] Greentree, A. D., Hamilton, A. R., Hollenberg, L. C. L. and Clark, R. G. Electrical readout of a spin qubit without double occupancy. http://xxx.lanl.gov/abs/cond-mat/0403449 (2004).

[14] Kouwenhoven, L. P., Austing, D. G. and Tarucha, S. Few-electron quantum dots. Rep. Prog. Phys. **64**, 701-736 (2001).

[15] Lu, W., Ji, Z., Pfeiffer, L., West, K. W. and Rimberg, A. J. Real-time detection of electron tunnelling in a quantum dot. Nature **423**, 422 (2003).

[16] Fujisawa, T., Hayashi, T., Hirayama, Y., Cheong, H. D. and Jeong, Y. H. Electron counting of single-electron tunnelling current. Appl. Phys. Lett. **84**, 2343 (2004).

[17] Weis, J., Haug, R. J., von Klitzing, K. and Ploog, K. Lateral transport through a single quantum dot with a magnetic field parallel to the current. Surf. Sci. **305**, 664 (1994).

[18] Kouwenhoven, L. P. et al. Excitation spectra of circular, few-electron quantum dots. Science **278**, 1788 (1997).

[19] Ciorga, M. et al. Readout of a single electron spin based quantum bit by current detection. Physica E **11**, 35 (2001).

[20] Fujisawa, T., Austing, D. G., Tokura, Y., Hirayama, Y. and Tarucha, S. Allowed and forbidden transitions in artificial hydrogen and helium atoms. Nature **419**, 278-281 (2002).

[21] Hanson, R. et al. Zeeman energy and spin relaxation in a one-electron quantum dot. Phys. Rev. Lett. **91**, 196802 (2003).

[22] Folk, J. A., Potok, R. M., Marcus, C. M. and Umansky, V. A gate-controlled bidirectional spin filter using quantum coherence. Science **299**, 679 (2003).

[23] Elzerman, J. M. et al. Few-electron quantum dot circuit with integrated charge read out. Phys. Rev. B **67**, R161308 (2003).

[24] Elzerman, J. M., Hanson, R., Willems van Beveren, L. H., Vandersypen, L. M. K. and Kouwenhoven, L. P. Excited-state spectroscopy on a nearly-closed quantum dot via charge detection. Appl. Phys. Lett. **84**, 4617-4619 (2004).

[25] Field, M. et al. Measurements of Coulomb blockade with a noninvasive voltage probe. Phys. Rev. Lett. **70**, 1311 (1993).

[26] Hanson, R. *et al.* Semiconductor few-electron quantum dot operated as a bipolar spin filter. http://xxx.lanl.gov/abs/cond-mat/011414 (2003)

[27] The automated data analysis procedure first corrects for the offset of each trace. This offset, resulting from low-frequency interference signals or charge switches, is found by making a histogram of the QPC current during the read-out stage of a particular trace. The histogram typically displays a peak due to fluctuations around the average value corresponding to an occupied dot. The center of a gaussian fit to the histogram gives the offset. Then each trace is checked to make sure that an electron was injected during the injection stage, by evaluating if the signal goes below the injection threshold (dotted horizontal line in Fig. 5.6a). If not, the trace is disregarded. Finally, to determine if a trace corresponds to 'spin-up' or 'spin-down', we disregard all points that lie below the previous point (since these could correspond to points on the falling pulse flank at the end of the injection stage), and check if any of the remaining points are above the threshold.

[28] Khaetskii, A. V. and Nazarov, Y. V. Spin-flip transitions between Zeeman sublevels in semiconductor quantum dots. Phys. Rev. B **64**, 125316 (2001).

[29] Golovach, V. N., Khaetskii, A. and Loss, D. Phonon-induced decay of the electron spin in quantum dots. http://xxx.lanl.gov/abs/cond-mat/0310655 (2003).

[30] Woods, L. M., Reinecke, T. L. and Lyanda-Geller, Y. Spin relaxation in quantum dots. Phys. Rev. B **66**, 161318(R) (2002).

[31] Erlingsson, S. I. and Nazarov, Y. V. Hyperfine-mediated transitions between a Zeeman split doublet in GaAs quantum dots: The role of the internal field. Phys. Rev. B **66**, 155327 (2002).

[32] Let us assume there is a spin-$\downarrow$ electron on the dot at the start of the read-out stage. The probability that the $\downarrow$-electron tunnels out (i.e. that it does

not relax to spin-$\uparrow$) is given by $1-\beta_1$. The probability that this tunnel event is detected (i.e. is not too fast) is given by $1-\beta_2$. Therefore, the probability that a spin-$\downarrow$ electron tunnels out and is detected, is $(1-\beta_1)(1-\beta_2)$. In addition, there is the possibility that the $\downarrow$-electron relaxes, with probability β_1, but a step in the QPC signal is nevertheless detected, with probability α, due to the 'dark count' mechanism. Therefore, the total probability that a spin-$\downarrow$ electron is declared 'spin-down' is given by $(1-\beta_1)(1-\beta_2)+(\alpha\beta_1)$ approximately.

Chapter 6

Semiconductor few-electron quantum dots as spin qubits

J. M. Elzerman, R. Hanson, L. H. Willems van Beveren,
F. Koppens, I. T. Vink, L. M. K. Vandersypen and L. P.
Kouwenhoven

The previous chapters described the progress we have made towards using a single electron spin in a lateral quantum dot as a spin qubit. In this chapter, we critically evaluate the steps we have taken and the ones we still have to take. Fabrication and characterization of a double quantum dot containing two coupled spins has been achieved, as well as initialization and single-shot read-out of the spin state. The single-spin relaxation time was found to be very long, but the decoherence time is still unknown. We present concrete ideas on how to proceed towards coherent spin operations. Single-spin manipulation relies on a microfabricated wire located close to the quantum dot, and two-spin interactions are controlled via the tunnel barrier connecting the respective quantum dots. To demonstrate superposition and entanglement of spin states, we plan to use a charge detection approach, without relying on transport measurements.

Some of the ideas in this chapter have been described in *Quantum Computing and Quantum Bits in Mesoscopic Systems*, Kluwer Academic, New York (2003) (see also quant-ph/0207059), and in cond-mat/0311414.

6.1 Introduction

In the previous chapters we have described experiments aimed at creating a quantum dot spin qubit according to the proposal by Loss and DiVincenzo [1] (see also paragraph 1.3). The key ingredients for these experiments – performed over the last two years – are a fully tunable few-electron double quantum dot and a quantum point contact (QPC) charge detector. We have operated the QPC in three different ways:

1. By measuring its DC conductance, changes in the average charge on the double dot are revealed, which can be used to identify the charge configuration of the system.
2. By measuring the conductance in real-time (with a bandwidth of ~ 100 kHz), we can detect individual electrons tunneling on or off the dot (in less than 10 μs).
3. By measuring the QPC response to a gate voltage pulse train (with the proper frequency) using a lock-in amplifier, we can determine the tunnel rate between the dot and a reservoir. In addition, by using a large pulse amplitude and measuring changes in the effective tunnel rate, we can identify excited states of the dot.

Using these techniques, we have demonstrated that our GaAs/AlGaAs quantum dot circuit is a promising candidate for a spin qubit. However, we do not have a fully functional qubit yet, as coherent manipulation of a single- or a two-spin system has so far remained elusive. In this chapter, we evaluate the experimental status of the spin qubit project in terms of the DiVincenzo requirements [2], and also discuss some related issues that have arisen over the past two years. We arrive at a realistic path towards the experimental demonstration of single- and two-qubit gates and the creation of entanglement of spins in quantum dot systems. We argue that demonstration of these steps is easiest by using the QPC charge detection approach, without relying on transport measurements.

6.2 Qubit

The first of the five DiVincenzo requirements is to have a scalable physical system with well-characterized qubits. We have fabricated double quantum dot devices in which a single electron can be confined in each of the two dots (see chapter 2). The spin states $|\uparrow\rangle$ and $|\downarrow\rangle$ of the electron, subject to a large magnetic field B, correspond to the two states of the proposed qubit two-level system. The Zeeman splitting, ΔE_Z, between the two states can be tuned with the magnetic field, according to $\Delta E_Z = g\mu_B B$, with $g \approx -0.44$ the electron g-factor in GaAs [3], and μ_B the Bohr magneton.

These one-electron dots can be fully characterized using a QPC as a charge detector, with the techniques developed in chapters 2 and 3. First of all, we can use the QPC to monitor the charge configuration of the double dot, in order to reach the regime where both dots contain just a single electron. Then we can evaluate and tune the tunnel rate from each dot to the reservoir using the lock-in technique described above. The same technique can be employed to determine the energy spectrum of each of the two dots, i.e. the Zeeman splitting between the two qubit states, as well as the energy of orbital excited states. Furthermore, the QPC can be used to monitor the inter-dot tunnel barrier, both qualitatively (from the curvature of lines in the honeycomb diagram, as shown in Fig. 2.6) and quantitatively (by performing photon-assisted tunneling spectroscopy to measure the tunnel splitting between the one-electron bonding and anti-bonding state, as in Ref. [4]). In principle, it is even possible to use the lock-in technique to measure the exchange splitting J between the delocalized two-electron singlet and triplet spin states. However, in practical situations the splitting might be too small (< 20 μeV) to be resolved using tunneling spectroscopy.

We can thus determine all relevant parameters of the two-spin system without performing transport measurements. The essential advantage of the QPC technique is that it works even for a dot that is very weakly coupled to just a *single* reservoir, with a tunnel rate between zero and ~ 100 kHz (limited by the bandwidth of the current measurement setup). This gives us more freedom to design simpler dots with fewer gates, which could therefore be easier to operate.

6.3 Read-out

We have achieved single-shot read-out of the spin orientation of an individual electron in a quantum dot (see chapter 5). Our approach utilizes the Zeeman splitting, induced by a large magnetic field parallel to the 2DEG, to create spin-to-charge conversion (Fig. 6.1a). This is followed by real-time detection of single-electron tunneling events using the QPC. The total visibility of the spin measurement is $\sim 65\%$, limited mostly by the ~ 40 kHz bandwidth of our current measurement setup, and also by thermal excitation of electrons out of the quantum dot, due to the high effective electron temperature of ~ 300 mK.

We estimate that we can improve the visibility of the spin read-out technique

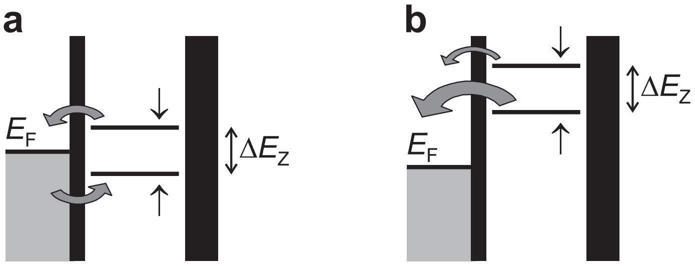

Figure 6.1: Schematic energy diagrams depicting spin-to-charge conversion based on a difference in *energy* **(a)** between $|\uparrow\rangle$ and $|\downarrow\rangle$, or on a difference in *tunnel rate* **(b)**.

to more than 90% by lowering the electron temperature below 100 mK, and especially by using a faster way to measure the charge on the dot. This could be possible with a 'radio-frequency QPC' (RF-QPC), similar to the well-known RF-SET [5]. In this approach, the QPC is embedded in an LC circuit with a resonant frequency of ~ 1 GHz. By measuring the reflection or transmission of a resonant carrier wave, we estimate that it should be possible to read out the charge state of the nearby quantum dot in $\sim 1\ \mu$s, an order of magnitude faster than is currently attainable.

A disadvantage of the read-out technique based on the Zeeman splitting is that it relies on accurate positioning of the dot-levels with respect to the Fermi energy of the reservoir, E_F (see Fig. 6.1a). This makes the spin read-out very sensitive to charge switches, which can easily push the $|\uparrow\rangle$ level above E_F, or pull $|\downarrow\rangle$ below E_F, resulting in a measurement error. To counteract this effect, a large enough Zeeman splitting is required (in chapter 5 a magnetic field of more than 8 Tesla was used, although with a more stable sample a lower field might be sufficient). On the other hand, a smaller Zeeman splitting is desirable because it implies a lower and therefore more convenient resonance frequency for coherent spin manipulation. In addition, the spin relaxation time is expected to be longer at smaller ΔE_Z. Therefore, a different spin read-out mechanism that is less sensitive to charge switches and can function at lower fields would be very useful.

A particularly convenient way to perform spin-to-charge conversion could be provided by utilizing not a difference in *energy* between spin-up and spin-down, but a difference in *tunnel rate* (Fig. 6.1b). To read out the spin orientation of an electron on the dot, we simply raise both dot levels above E_F, so that the electron can leave the dot. If the tunnel rate for spin-up electrons, $\Gamma_\uparrow$, is much larger than that for spin-down electrons, $\Gamma_\downarrow$, then at a suitably chosen time the dot will have a large probability to be already empty if the spin was up, but a large probability to be still occupied if the spin is down. Measuring the charge

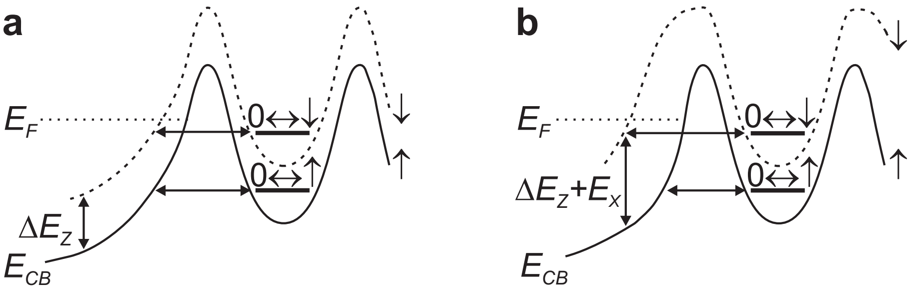
a
E_F
$0\leftrightarrow\downarrow$
$0\leftrightarrow\uparrow$
↓
↑
ΔE_Z
E_{CB}
b
E_F
$0\leftrightarrow\downarrow$
$0\leftrightarrow\uparrow$
↓
↑
ΔE_Z+E_X
E_{CB}

Figure 6.2: Exchange interaction in the reservoirs leading to spin-selective tunnel rates. **(a)** Schematic diagram of the conduction band edge E_{CB} near the dot for electrons with spin-up (solid line) and spin-down (dashed line). If ΔE_Z in the reservoirs is the same as in the dot, the tunnel rates do not depend on spin. **(b)** The exchange energy E_X in the reservoirs close to the dot induces spin-dependent tunnel rates.

on the dot within the spin relaxation time can then reveal the spin state.

This scheme is very robust against charge switches, since no precise positioning of the dot levels with respect to the leads is required: both levels simply have to be above E_F. Also, switches have a small influence on the tunnel rates themselves, as they tend to shift the whole potential landscape up or down, which does not change the tunnel barrier for electrons in the dot [6]. Of course, the visibility of this spin measurement scheme depends on the difference in tunnel rate we can achieve.

A difference in tunnel rate for spin-up and spin-down electrons is provided by the magnetic field. From large-bias transport measurements in a magnetic field parallel to the 2DEG [7], we find that the spin-selectivity ($\Gamma_\uparrow/\Gamma_\downarrow$) grows roughly linearly from ~ 1.5 at 5 Tesla to ~ 5 at 14 Tesla. This is in good agreement with the spin-selectivity of about 3 that was found at 10 Tesla using the single-shot spin measurement technique of chapter 5.

We believe that this spin-dependence of the tunnel rates is due to exchange interactions in the reservoirs. If ΔE_Z is the same in the dot as in the reservoirs, the tunnel barrier will be the same for $|\uparrow\rangle$ and $|\downarrow\rangle$ electrons, giving $\Gamma_\uparrow = \Gamma_\downarrow$ (Fig. 6.2a). However, close to the dot there is a region with only $|\uparrow\rangle$ electrons, where an electron that is excited from $|\uparrow\rangle$ to $|\downarrow\rangle$ must overcome not only the single-particle Zeeman energy but also the many-body exchange energy between the reservoir electrons [8]. We can describe this situation with an effective g-factor g_{eff}, which can be larger than the bare g-factor (Fig. 6.2b). In this case, $|\downarrow\rangle$ electrons experience a thicker tunnel barrier than $|\uparrow\rangle$ electrons, resulting in a difference in tunnel rates [9].

In a magnetic field parallel to the 2DEG, the effect only leads to a modest spin-selectivity that does not allow a single-shot measurement. However, a much larger spin-selectivity is possible in a perpendicular magnetic field [8], i.e. in the Quantum Hall regime. Magnetotransport measurements in 2DEGs with odd filling factor have shown that the g-factor can be enhanced by as much as a factor of ten, depending on the field strength. We anticipate that a convenient perpendicular field of ~ 4 T could already give enough spin-selectivity to allow high-fidelity spin read-out. Therefore, spin read-out should be feasible not only in a large parallel magnetic field, but also in a somewhat smaller perpendicular field.

6.4 Initialization

Initialization of the spin to the pure state $|\uparrow\rangle$ – the desired initial state for most quantum algorithms [10] – has been demonstrated in chapter 5. There it was shown that by waiting long enough, energy relaxation will cause the the spin on the dot to relax to the $|\uparrow\rangle$ ground state (Fig. 6.3a). This is a very simple and robust initialization approach, which can be used for any magnetic field orientation (provided that $g\mu_B B > 5k_B T$). However, as it takes about $5T_1$ to reach equilibrium, it is also a very slow procedure (≥ 10 ms), especially at lower magnetic fields, where the spin relaxation time T_1 might be very long.

A faster initialization method has been used in the 'reverse pulse' technique in chapter 5. By placing the dot in the read-out configuration (Fig. 6.3b), a spin-up electron will stay on the dot, whereas a spin-down electron will be replaced by a spin-up. After waiting a few times the sum of the typical tunnel times for spin-up and spin-down ($\sim 1/\Gamma_\uparrow + 1/\Gamma_\downarrow$), the spin will be with large probability

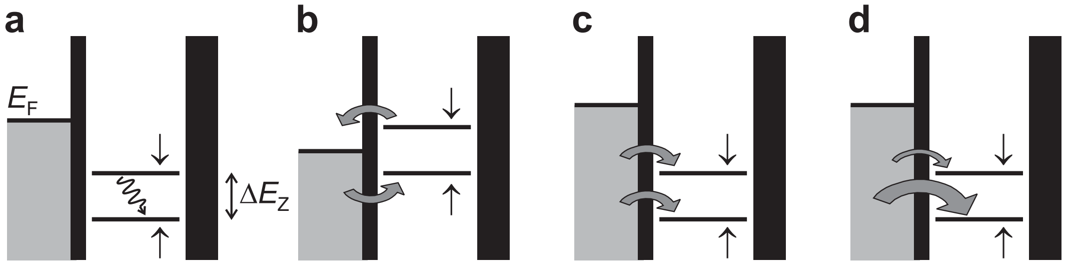

Figure 6.3: Schematic energy diagrams depicting initialization procedures in a large parallel or perpendicular magnetic field. **(a)** Spin relaxation to pure state $|\uparrow\rangle$. **(b)** The 'read-out' configuration can result in $|\uparrow\rangle$ faster. **(c)** Random spin injection gives a statistical mixture of $|\uparrow\rangle$ and $|\downarrow\rangle$. **(d)** In a large perpendicular field providing a strong spin-selectivity, injection results mostly in $|\uparrow\rangle$.

in the $|\uparrow\rangle$ state. This initialization procedure can therefore be quite fast (< 1 ms), depending on the tunnel rates.

We also have the possibility to initialize the dot to a mixed state, where the spin is probabilistically in $|\uparrow\rangle$ or $|\downarrow\rangle$. In chapter 5, mixed-state initialization was demonstrated in a parallel field by first emptying the dot, followed by placing both spin levels below E_F during the 'injection stage' (Fig. 6.3c). The dot is then randomly filled with either a spin-up or a spin-down electron. This is very useful, e.g. to test two-spin operations (see paragraph 6.7).

In a large perpendicular field providing a strong spin-selectivity, initialization to the $|\uparrow\rangle$ state is possible via spin relaxation (Fig. 6.3a) or via direct injection (Fig. 6.3d). Initialization to a mixed state (or in fact to any state other than $|\uparrow\rangle$) is very difficult due to the spin-selectivity. It probably requires the ability to coherently rotate the spin from $|\uparrow\rangle$ to $|\downarrow\rangle$ (see paragraph 6.6).

6.5 Coherence times

The long-term potential of GaAs quantum dots as electron spin qubits clearly depends crucially on the spin coherence times T_1 and T_2. In chapter 5, we have shown that the single-spin relaxation time, T_1, can be very long – on the order of 1 ms at 8 T. This implies that the spin is only very weakly disturbed by the environment. The dominant relaxation mechanism at large magnetic field is believed to be the coupling of the spin to phonons, mediated by the spin-orbit interaction [11].

The fundamental quantity of interest for spin qubits is the decoherence time of a single electron spin in a quantum dot, T_2, which has never been measured. Experiments with electrons in 2DEGs have established an ensemble-averaged decoherence time, T_2^*, of $\sim$ 100 ns [12]. Recently, a similar lower bound on T_2 has been claimed for a single trapped electron spin, based on the linewidth of the observed electron spin resonance [13]. Theoretically, it has been suggested that the real value of T_2 can be much longer [11], and under certain circumstances could even be given by $T_2 = 2T_1$, limited by the same spin-orbit interactions that limit T_1.

To build a scalable quantum computer, a sufficiently long T_2 (corresponding to more than 10^4 times the gate operation time) is essential in order to reach the 'accuracy threshold'. However, for experiments in the near future, we only need to perform a few spin rotations within T_2, which might already be possible for much shorter T_2, on the order of a μs. This should also be long enough to perform two-spin operations, which are likely to be much faster. To find the actual value of T_2, the ability to perform coherent spin operations is required. This is discussed in the next paragraphs.

6.6 Coherent single-spin manipulation: ESR

We have not yet satisfied the key requirement for an actual spin qubit: coherent manipulation of one- and two-spin states. To controllably create superpositions of $|\uparrow\rangle$ and $|\downarrow\rangle$, we can use the well-known electron spin resonance (ESR) effect. A microwave magnetic field $\vec{B_{ac}}$ oscillating in the plane perpendicular to $\vec{B}$, at a frequency $f = g\mu_B B/h$ (in resonance with the spin precession about $\vec{B}$) causes the spin to make transitions between $|\uparrow\rangle$ and $|\downarrow\rangle$. The choice of B strength is a trade-off between reliable initialization and read-out (strong B is better) and experimental convenience (low f is easier). We expect that a perpendicular field of 4 Tesla should be sufficient to provide high-fidelity read-out and initialization, with $f \approx 25$ GHz (for $g = -0.44$). Alternatively, in a parallel field we may have to go up to 8 Tesla, corresponding to $f \approx 45$ GHz [3], for high-fidelity spin measurement. However, since single-shot read-out is not strictly required, a somewhat lower field could also be enough.

Properly timed bursts of microwave power tip the spin state over a controlled angle, e.g. 90° or 180°. In order to observe Rabi oscillations, the Rabi period

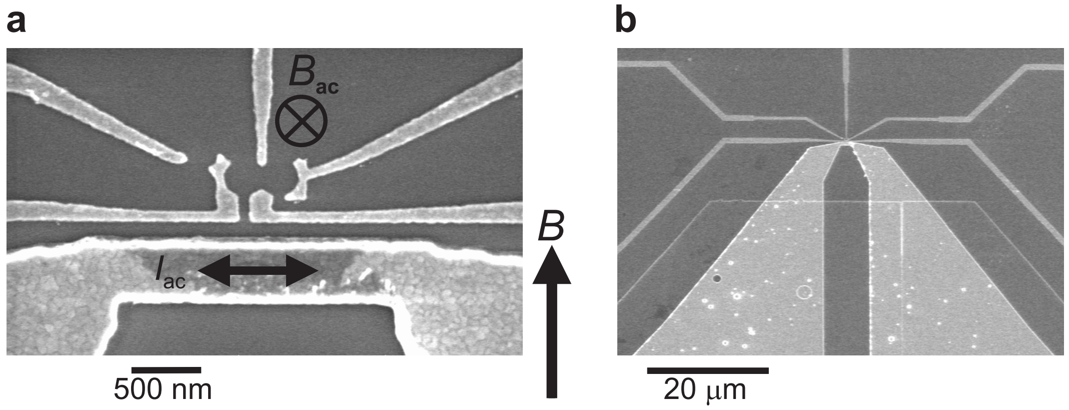

Figure 6.4: On-chip wire to apply microwaves to a nearby quantum dot. The device was made by Laurens Willems van Beveren and Jort Wever. **(a)** Scanning electron microscope image of a device consisting of a double quantum dot in close proximity to a gold wire. An AC current through the wire, I_{ac}, generates an oscillating magnetic field, B_{ac}, perpendicular to the plane. If the AC frequency is resonant with the Zeeman splitting due to a large static in-plane magnetic field, B, a spin on the dot will rotate. **(b)** Large-scale view of the wire, designed to be a 50 Ω coplanar stripline.

must be at most of the order of the single-spin decoherence time T_2. For a Rabi period of 150 ns, we need a microwave field strength B_{ac} of ~ 1 mT. If T_2 is much longer, there is more time to coherently rotate the spin, so a smaller oscillating field is sufficient.

We intend to generate the oscillating magnetic field by sending an alternating current through an on-chip wire running close by the dot (Fig. 6.4a). If the wire is placed well within one wavelength (which is a few mm at 30 GHz near the surface of a GaAs substrate) from the quantum dot, the dot is in the near-field region and the electric and magnetic field distribution produced by the AC current should be the same as for a DC current [14]. With a wire 200 nm from the dot, a current of ~ 1 mA should generate a magnetic field of about 1 mT and no electric field at the position of the dot. To minimize reflection and radiation losses, the wire is designed to be a shorted coplanar stripline (Fig. 6.4b) with a 50 Ω impedance.

To detect the electron spin resonance (ESR) and obtain a lower bound on T_2 from the linewidth of the resonance signal, various methods have been proposed, either using transport measurements [15] or relying on charge detection [16]. In both cases, the required spin-to-charge conversion is achieved by positioning the dot levels around the Fermi energy of the reservoir (Fig. 6.5a–b). The ESR-field induces spin flips, exciting $|\uparrow\rangle$ electrons to $|\downarrow\rangle$, which can then tunnel out of the dot. This leads to an average current (Fig. 6.5a) or to a change in the average occupation of the dot (Fig. 6.5b). However, in this configuration the dot is particularly sensitive to spurious effects induced by the microwaves, such as $|\uparrow\rangle$ electrons being excited out of the dot via thermal excitation or photon-assisted tunneling. These processes can completely obscure the spin resonance.

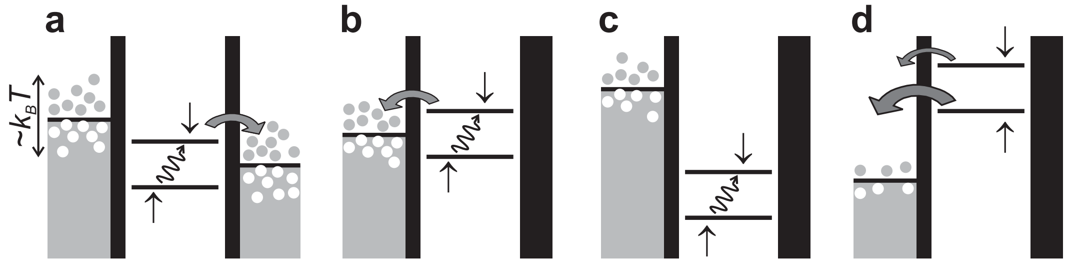

Figure 6.5: Detecting ESR. **(a)** To detect ESR in a transport measurement [15], the dot is placed in Coulomb blockade, so that electron spins that are flipped by the ESR field can contribute to a current. **(b)** A similar configuration is used to detect ESR via changes in the occupation of the dot [13], measured using a charge detector. **(c)** If the dot is deep in Coulomb blockade during the spin-flip stage, the electron is not easily excited to the reservoir via thermal excitation or photon-assisted tunneling. **(d)** The microwaves are off during the spin read-out stage to enhance the measurement fidelity.

Such problems can be avoided by combining (pulsed) electron spin resonance with *single-shot* spin measurement. This allows us to separate the spin manipulation stage (during which the microwaves are on) from the spin read-out stage (without microwaves). In this way, excitation out of the dot is prevented by Coulomb blockade (Fig. 6.5c), until spin read-out is initiated (Fig. 6.5d). In contrast to the techniques described above – which require a large spin flip rate to generate a *measurable* current or disturbance of the dot occupation – this approach only requires the spin flip rate to be faster than the decoherence rate. Therefore, a longer T_2 allows us to use a smaller B_{ac}, corresponding to (quadratically) smaller microwave power. This should help to suppress heating and photon-assisted tunneling.

In principle, an ESR experiment can be performed in a parallel or a perpendicular magnetic field. The read-out in a perpendicular field is particularly suitable for ESR detection, as the dot levels are far above E_F (so are not affected by photon-assisted tunneling or heating). If $\vec{B}$ is perpendicular to the surface, $\vec{B_{ac}}$ must run through the dot in a direction parallel to the surface, so we must place the wire above the dot rather than to its side. The wire could be located on top of an insulating dielectric layer that covers the gate electrodes.

6.7 Coherent spin interactions: $\sqrt{\text{SWAP}}$

Two electron spins $\vec{S_1}$ and $\vec{S_2}$ in neighbouring quantum dots are coupled to each other by the exchange interaction, which takes the form $J(t)\vec{S_1} \cdot \vec{S_2}$. If the double dot is filled with two identical spins, the interaction does not change their orientation. However, if the left electron spin starts out being $|\uparrow\rangle$ and the right one $|\downarrow\rangle$, then the states of the two spins will be swapped after a certain time. An interaction active for half this time performs the $\sqrt{\text{SWAP}}$ gate, which has been shown to be universal for quantum computation when combined with single qubit rotations [17]. In fact, the exchange interaction is even universal by itself when the state of each qubit is encoded in the state of three electron spins [18].

The strength $J(t)$ of the exchange interaction depends on the overlap of the two electron wavefunctions, which varies exponentially with the voltage applied to the gate controlling the inter-dot tunnel barrier. By applying a (positive) voltage pulse with a certain amplitude and duration, we can temporarily turn on the exchange interaction, thereby performing a $\sqrt{\text{SWAP}}$ gate. We expect that J may correspond to a frequency of $\sim$ 10 GHz, so two-qubit gates could be performed in $\sim$ 100 ps. A much larger value would not be convenient experimentally, as we would have to control the exact amplitude and duration of the pulse very precisely.

On the other hand, a very slow exchange operation would be more sensitive to decoherence resulting from fluctuations in the tunnel rate, due to charge noise. The value of J can in principle be determined in a transport measurement [19], or alternatively by using the QPC tunnel spectroscopy technique developed in chapter 3. However, in practical situations J might be too small to be resolved.

To explore the operation of the SWAP gate, we only need reliable initialization and read-out, without requiring ESR [1]. Imagine qubit 1 is prepared in a pure state $|\uparrow\rangle$ and qubit 2 is prepared in a statistical mixture of $|\uparrow\rangle$ and $|\downarrow\rangle$. Measurement of qubit 1 should then always give $|\uparrow\rangle$, while measurement of qubit 2 should give probabilistically $|\uparrow\rangle$ or $|\downarrow\rangle$. After application of the SWAP gate, in contrast, measurement of qubit 2 should always give $|\uparrow\rangle$, while measurement of qubit 1 should give a probabilistic outcome. This and other spin-interaction experiments are probably easiest in a parallel magnetic field, where initialization to a statistical mixture is convenient. In addition, a large perpendicular field shrinks the electron wavefunctions, lowering the tunnel coupling and thus the exchange interaction between the two dots.

6.8 Unresolved issues

Several issues are not yet fully resolved, both experimentally and theoretically. One of these is the question of electron spin resonance in the reservoir. There are indications that the g-factor in the dot is different from that in the reservoir [20] (disregarding enhancement due to exchange interactions, which are not relevant for a 'global' excitation such as ESR). However, if the two g-factors are equal, then any coherent operation of the spin on the dot will also influence the spin population outside the dot. This has not been taken into account in this chapter, but it could lead to complications for the proposed ESR experiments.

Another question is related to the $\sim 10^6$ nuclear spins in the quantum dot that couple to the electron spin via the hyperfine coupling. Through the Overhauser effect they produce an effective magnetic field, which can be very large (~ 5 T) for a fully polarized nuclear spin ensemble. Statistical fluctuations in the Overhauser field could lead to changes in the phase of the electron spin. It is not yet clear what the influence will be on spin manipulation experiments. If it turns out to be a problem, we may have to polarize the nuclear system completely in order to suppress the fluctuations.

A more practical consideration is the effect of charge switches in the heterostructure, which make any experiment more difficult. This is particularly true for two-spin interaction experiments, as charge noise can affect the inter-dot tunnel barrier and therefore the exchange interaction, resulting in decoherence. In collaboration with the group of Prof. Wegscheider in Regensburg, we have started to investigate the possible origin of charge switching, in an effort to produce more quiet heterostructures and devices.

Finally, so far we have used at most two quantum dots, not paying much attention to the scalability of our spin qubit approach. For instance, the ESR-field generated by the big wire runing next to the double dot will also influence other spins in nearby dots. We may therfore have to develop techniques to locally control the g-factor felt by the electron spin in a dot, in order to shift particular dots in or out of resonance.

6.9 Conclusion and outlook

In summary, we have demonstrated that single electrons trapped in GaAs lateral quantum dots are promising candidates for implementing a spin qubit. We have realized the 'hardware' for such a system: a device consisting of two coupled quantum dots that can be filled with one electron spin each, flanked by two quantum point contacts. Using these QPCs as charge detectors, we can determine all relevant parameters of the double dot. In addition, we have developed a technique to measure the spin orientation of an *individual* electron. Now we can proceed to combine all these ingredients with the ability to generate strong microwave magnetic fields close to the dot, and gate voltage pulses to control the inter-dot coupling, in order to demonstrate superposition and entanglement of spin states.

For such experiments, the QPC is an invaluable tool. It allows us to probe a dot that is nearly isolated from the reservoirs, which is a regime not accessible to conventional transport experiments. Most importantly, it enables us to study a *single* spin or charge, rather than measuring average properties of a large ensemble. The QPC charge and spin detector is therefore essential to achieve the kind of single-particle control that is required for creating a qubit – transport experiments are no longer necessary.

The techniques we have developed are not only suitable for quantum computation. Now that the spin orientation of a single electroncan be measured, we can think of using the spin as a local probe to explore the semiconductor environment. For instance, measuring the spin relaxation time in various situations could reveal details of different mechanisms for spin-orbit coupling. We could vary the orientation of the magnetic field with respect to the crystal axes, or investigate the effect of static or time-varying electric fields. Once we can measure the electron spin resonance frequency, this would allow us to study the polarization of the nuclear spin ensemble via the Overhauser effect. In all these cases, the fact that dot parameters such as the Zeeman splitting or the tunnel coupling to reservoirs can be controlled *in situ*, makes a lateral quantum dot filled with a single spin a system of great versatility and fundamental importance.

We thank C.J.P.M. Harmans, W.G. van der Wiel, M. Blaauboer, S. Tarucha, and D. Loss for useful discussions. We acknowledge financial support from the Specially Promoted Research Grant-in-Aid for Scientific Research; the Ministry of Education, Science and Culture in Japan; DARPA grant DAAD19-01-1-0659 of the QuIST program; the Dutch Organization for Fundamental Research on Matter (FOM); and the European Union through a TMR Program Network.

References

[1] D. Loss and D.P. DiVincenzo, Phys. Rev. A **57**, 120 (1998).

[2] D.P. DiVincenzo, Fortschr. Phys. **48**, 771 (2000).

[3] R. Hanson, B. Witkamp, L.M.K. Vandersypen, L.H. Willems van Beveren, J.M. Elzerman, and L.P. Kouwenhoven Phys. Rev. Lett. **91**, 196802 (2003).

[4] J.R. Petta, A.C. Johnson, C.M. Marcus, M.P. Hanson, and A.C. Gossard, cond-mat/0408139 (2004).

[5] R.J. Schoelkopf, P. Wahlgren, A.A. Kozhevnikov, P. Delsing, and D.E. Prober, Science **280**, 1238 (1998).

[6] S.W. Jung, T. Fujisawa, Y.H. Jeong and Y. Hirayama, cond-mat (2004).

[7] R. Hanson, L.M.K. Vandersypen, L.H. Willems van Beveren, J.M. Elzerman, I.T. Vink, and L.P. Kouwenhoven, cond-mat/0311414 (2003).

[8] T. Englert, D.C. Tsui, A.C. Gossard, and C. Uihlein. Surface Science **113**, 295 (1982).

[9] M. Ciorga *et al.* Phys. Rev. B **61**, R16315 (2000).

[10] M.A. Nielsen and I.L. Chuang, *Quantum computation and quantum information*, Cambridge University Press, Cambridge, England (2000).

[11] V.N. Golovach, A. Khaetskii, and D. Loss, Phys. rev. Lett. **93**, 016601 (2004).

[12] J.M. Kikkawa and D.D. Awschalom, Nature **397**, 139 (1999).

[13] M. Xiao, I. Martin, E. Yablonovitch, and H.W. Jiang, Nature **430**, 435 (2004).

[14] J.D. Jackson, *Classical electrodynamics*, Wiley, New York (1998).

[15] H.A. Engel and D. Loss, Phys. Rev. Lett. **86**, 4648 (2001).

[16] I. Martin, D. Mozyrsky, and H.W. Jiang, Phys. Rev. Lett. textbf90, 018301 (2003).

[17] G. Burkard, D. Loss, and D.P. DiVincenzo, Phys. Rev. B **59**, 2070 (1999).

[18] D.P. DiVincenzo, D.P. Bacon, D.A. Lidar, and K.B. Whaley, Nature **408**, 339 (2000).

[19] V.N. Golovach and D. Loss, Phys. Rev. B **69**, 245327 (2004).

[20] M. Dobers, K. v. Klitzing, and G. Weiman. Phys. Rev. B **38**, 5453 (1988).

Chapter 7

The Kondo effect in the unitary limit

W. G. van der Wiel, S. De Franceschi, T. Fujisawa,
J. M. Elzerman, S. Tarucha and L. P. Kouwenhoven

We observe a strong Kondo effect in a semiconductor quantum dot when a small magnetic field is applied. The Coulomb blockade for electron tunneling is overcome completely by the Kondo effect and the conductance reaches the unitary-limit value. We compare the experimental Kondo temperature with the theoretical predictions for the spin-1/2 Anderson impurity model. Excellent agreement is found throughout the Kondo regime. Phase coherence is preserved when a Kondo quantum dot is included in one of the arms of an Aharonov-Bohm ring structure and the phase behavior differs from previous results on a non-Kondo dot.

This chapter has been published in Science **289**, 2105 (2000).

7.1 Introduction

The Kondo theory explains the increased resistivity of a metal with magnetic impurities at low temperatures [1]. Predictions from 1988 indicate that quantum dots could also exhibit the Kondo effect [2-7], but now as an increased conductance, G, which can reach the unitary limit ($G = 2e^2/h$) at low temperature. Recent experiments have confirmed the presence of the Kondo effect in quantum dots, however not reaching the unitary limit [8-12]. We demonstrate the unitary limit Kondo effect in a semiconductor quantum dot. Our quantum dot is embedded in one of the arms of an Aharonov-Bohm (AB) ring, which enables us to show that electron transport through the many-body Kondo state is at least partly phase-coherent. The Kondo effect arises from the coupling between a localized electron spin to a sea of conduction electrons. The strength is characterized by the Kondo temperature, T_K [13]

$$T_K = \frac{\sqrt{\Gamma U}}{2} e^{\pi\varepsilon_0(\varepsilon_0+U)/\Gamma U} \tag{7.1}$$

where U is the on-site electron repulsion energy, or charging energy, ε_0 the energy of the single-particle state, and Γ reflects its width, due to a finite lifetime from tunneling to the leads (see left inset to Fig. 7.3a). In quantum dots these parameters can be controlled experimentally, resulting in a 'tunable Kondo effect' [8-12].

7.2 Strong Kondo effect at $B = 0.4$ T

Our device (Fig. 7.1a) consists of an AB ring defined in a 2-dimensional electron gas (2DEG) [14]. The conductance of the ring without applying gate voltages is $\sim 10e^2/h$, implying that the current is carried by several modes in each arm. In our experiment, a quantum dot has only been formed in the lower arm. One gate in the upper arm is used to pinch off the upper arm. All measurements are performed in a dilution refrigerator with a base temperature of 15 mK, using a standard lock-in technique with an ac voltage excitation between source and drain contacts of 3 μV.

The linear-response conductance, G, through the lower dot versus gate voltage, V_{gl}, and magnetic field, B, is shown in a color scale plot (Fig. 7.1b). Here, the left and right parts of the lower arm serve as leads to the dot. In Fig. 7.1c two $G(V_{gl})$ curves are extracted from Fig. 7.1b for $B = 0$ and 0.4 T. At $B = 0$, regular Coulomb oscillations are observed with low valley conductance. In some

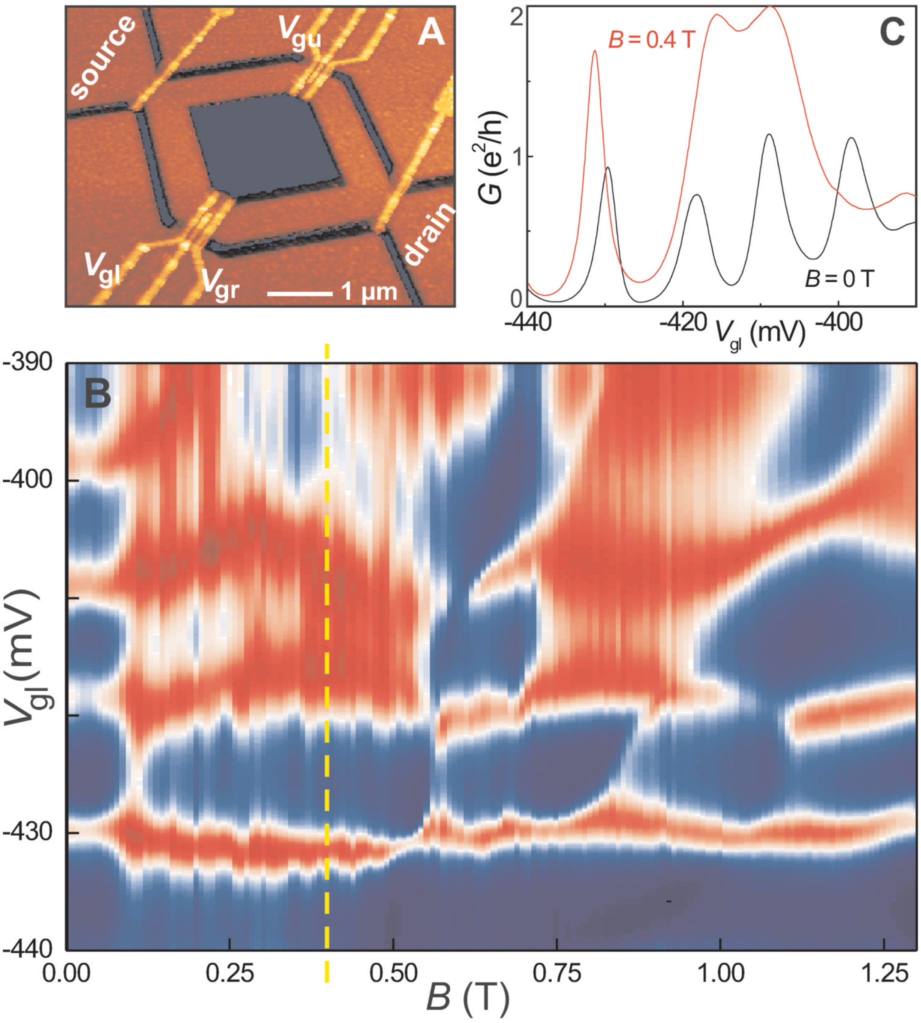

Figure 7.1: **(a)** Atomic force microscope image of the device. An Aharonov-Bohm (AB) ring is defined in a 2DEG by dry etching of the dark regions (depth is 75 nm). The 2DEG with electron density, $n_S = 2.6 \times 10^{15}$ m^{-2}, is situated 100 nm below the surface of an AlGaAs/GaAs heterostructure. In both arms of the ring (lithographic width 0.5 μm, inner perimeter 6.6 μm) a quantum dot can be defined by applying negative voltages to gate electrodes. The gates at the entry and exit of the ring are not used. A quantum dot of size ~200 nm × 200 nm, containing ~100 electrons, is formed in the lower arm using gate voltages, V_{gl} and V_{gr} (the central plunger gate was not working). The average energy spacing between single-particle states is 100 μeV. The conductance of the upper arm, set by V_{gu}, is kept zero except for AB measurements. **(b)** Color scale plot of the conductance, G, as function of V_{gl} and B for V_{gr} = -448 mV and T = 15 mK. The upper arm of the AB ring is pinched off by V_{gu} = -1.0 V. Red (blue) corresponds to high (low) conductance. **(c)** Two selected traces $G(V_{gl})$ for $B = 0$ and $B = 0.4$ T. The Coulomb oscillations at $B = 0$ correspond to the oscillating color in (b). For some ranges of B, the valley conductance increases considerably, reaching values close to $2e^2/h$, i.e. the unitary limit, e.g. along the yellow dashed line at 0.4 T.

magnetic field ranges, however, the valley conductance increases considerably and can even reach $2e^2/h$, for instance for $B = 0.4$ T. We will discuss Fig. 7.1b in more detail below, but first focus on the large conductance values observed at B = 0.4 T.

Figure 7.3a shows Coulomb oscillations for different temperatures. At base temperature, the valleys around V_{gl} = -413 mV and -372 mV reach the maximum possible conductance value of $2e^2/h$. In fact, the valleys tend to disappear. When the temperature is increased, two separate Coulomb peaks develop with growing peak spacing. The conductance in the center of the valley has a logarithmic T-dependence with a saturation at $2e^2/h$ for low T, which is not due to electronic noise (right inset to Fig. 7.3a). The adjacent Coulomb valleys show an opposite T-dependence. This even-odd asymmetry indicates an unpaired spin in a valley with an odd electron number, where we observe the Kondo anomaly, and a spin singlet for an even electron number [8, 9]. Figure 7.3b shows the differential conductance for different T in the middle of the Kondo plateau at $2e^2/h$. The pronounced peak around $V_{SD} = 0$ reflects the Kondo resonance at the Fermi energy. The peak height has the same T-dependence as shown in the right inset to Fig. 7.3a. The width of the peak increases linear with temperature (inset to Fig. 7.3b).

7.3 Unitary limit of conductance

These measurements are taken after optimizing the two barrier gate voltages, V_{gl} and V_{gr}, in order to obtain nearly equal tunnel barriers. However, sweeping V_{gl}, as in Fig. 7.3a, changes the left barrier much more effectively than the right tunnel barrier and hence the barriers cannot be symmetric over the whole V_{gl}-range. For a quantitative comparison to theory, we therefore optimize V_{gr} by fixing it at a value chosen such that, upon sweeping V_{gl}, we obtain a flat plateau close to $2e^2/h$ (Fig. 7.2a) [15]. The two discernable Coulomb oscillations at higher temperatures have completely merged together at low temperature. This unitary limit was predicted [3, 4], but not observed before. The unitary limit implies that the transmission probability through the quantum dot is equal to one. This is a remarkable phenomenon since the quantum dot contains two tunnel barriers, each with a transmission probability much less than one. In addition, the on-site Coulomb energy, U, tends to block the state with an extra electron on the dot. Despite U being an order of magnitude larger than the characteristic energy scale, k_BT_K, the Kondo effect completely determines electron tunneling at low energies (i.e. low T and V_{SD}). Note that in the absence of the Kondo effect (e.g. for electron number N = even), the system consists of two separated Fermi seas. In contrast, for N = odd the screening of the local spin creates a single, extended many-body system with a single, well-defined Fermi surface extending throughout the whole system. The quasi-particles at this Fermi surface no longer experience the repulsive barrier potentials, nor the on-site Coulomb repulsion. Also note that since the local spin for N = odd is completely screened and since the dot has zero spin for N = even, the whole system of leads and dot is in a singlet state over a wide gate voltage range (between -430 mV and -350 mV in Fig. 7.3a), although the nature of the ground state in the even and odd valleys is very different.

7.4 Kondo temperature and scaling

For a quantitative analysis we rewrite Eq. 7.1 as $\ln(T_K) = \pi\varepsilon_0(\varepsilon_0 + U)/\Gamma U$ + constant, indicating a quadratic dependence for $\ln(T_K)$ on gate voltage, V_{gl} [16]. Following the work in [17], we fit G versus T for different gate voltages (see Fig. 7.2c) to the empirical function

$$G(T) = G_0 \left(\frac{T_K'^2}{T^2 + T_K'^2} \right)^s \tag{7.2}$$

with $T_K' = T_K/\sqrt{2^{1/s} - 1}$ where the fit parameter $s \approx 0.2$ for a spin-1/2 system [17, 18]. Figure 7.2b shows the obtained Kondo temperatures, T_K versus V_{gl}. The red parabola demonstrates that the obtained values for T_K are in excellent agreement with Eq. 7.1 [19].

The Kondo temperature as derived above, is obtained from the linear response conductance. In earlier works [8-12] estimates for T_K were obtained from measurements of dI/dV_{SD} versus V_{SD} (I is the current between source and drain). In that case, the full width at half maximum (FWHM) was set equal to $k_B T_K/e$. However, applying a finite V_{SD} introduces dephasing even at $T = 0$ [6,20]. To compare these two methods, we also plot in Fig. 7.2b (FWHM/k_B) measured for different gate voltages at base temperature. Also now we find a parabolic dependence, but the values are larger than T_K obtained from linear-response measurements. The difference may indicate the amount of dephasing due to a non-zero V_{SD}.

The normalized conductance, $G/(2e^2/h)$, is expected to be a universal function of the normalized temperature, T/T_K, independent of the other energy scales, U, ε_0 and Γ. Over a range of $\Delta\varepsilon_0 = 225$ μeV corresponding to 2.6 Kelvin, which

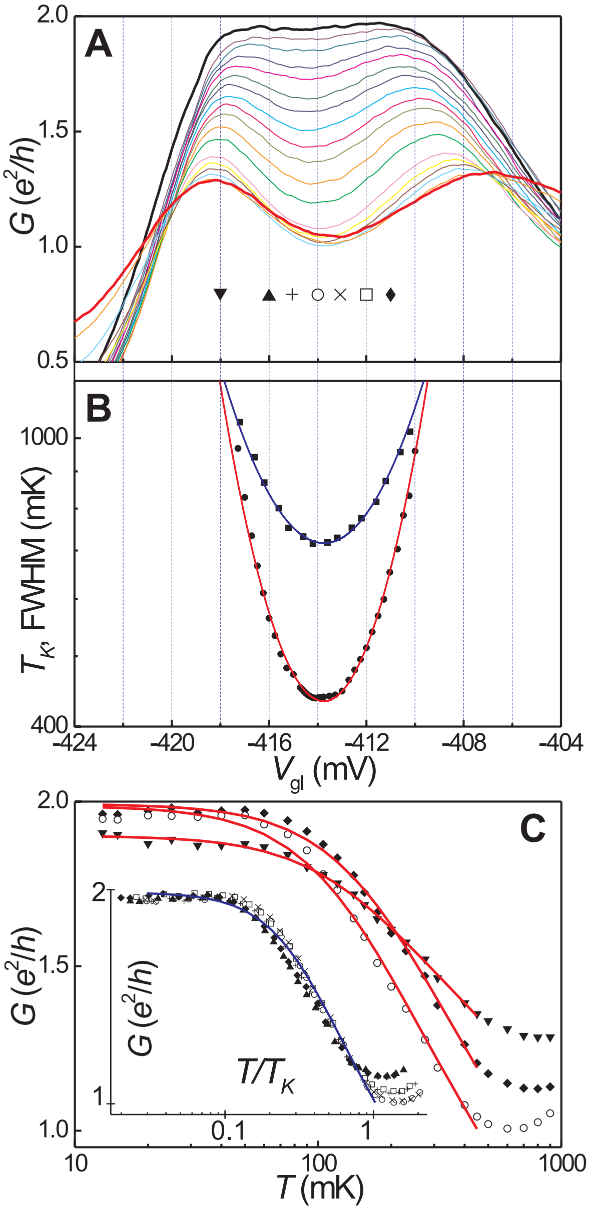

Figure 7.2: Quantitative analysis in the case of optimized symmetric tunnel barriers. **(a)** $G(V_{gl})$ for T = 15 mK (thick black trace) up to 900 mK (thick red trace) and V_{gr} = -448 mV, B = 0.4 T. **(b)** T_K versus V_{gl} (●) as obtained from many fits as in (c). In addition, we plot the peak width (FWHM/k_B) versus V_{gl} (■) as deduced from $dI/dV_{SD}(V_{SD})$ measurements at base temperature (see, e.g., black trace in Fig. 7.3b). Both data sets are fitted to Eq. 7.1, resulting in the red and blue parabolas, respectively. **(c)** $G(T)$ at fixed gate voltage as extracted from (a) for V_{gl} = -411 (♦), -414 (○) and -418 (▼) mV (labels are also indicated in (a)). The red curves are fits to Eq. 7.2. The inset shows that G versus normalized temperature T/T_K scales to a single curve for different gate voltages, V_{gl} = -411 (♦), -412 (□), -413 (×), -414 (○) -415 (+), -416 (▲) mV. The blue curve is a fit to Eq. 7.2 with fixed $T_K = 1$ and $G_0 = 2e^2/h$; $s = 0.29$ is the only fit parameter.

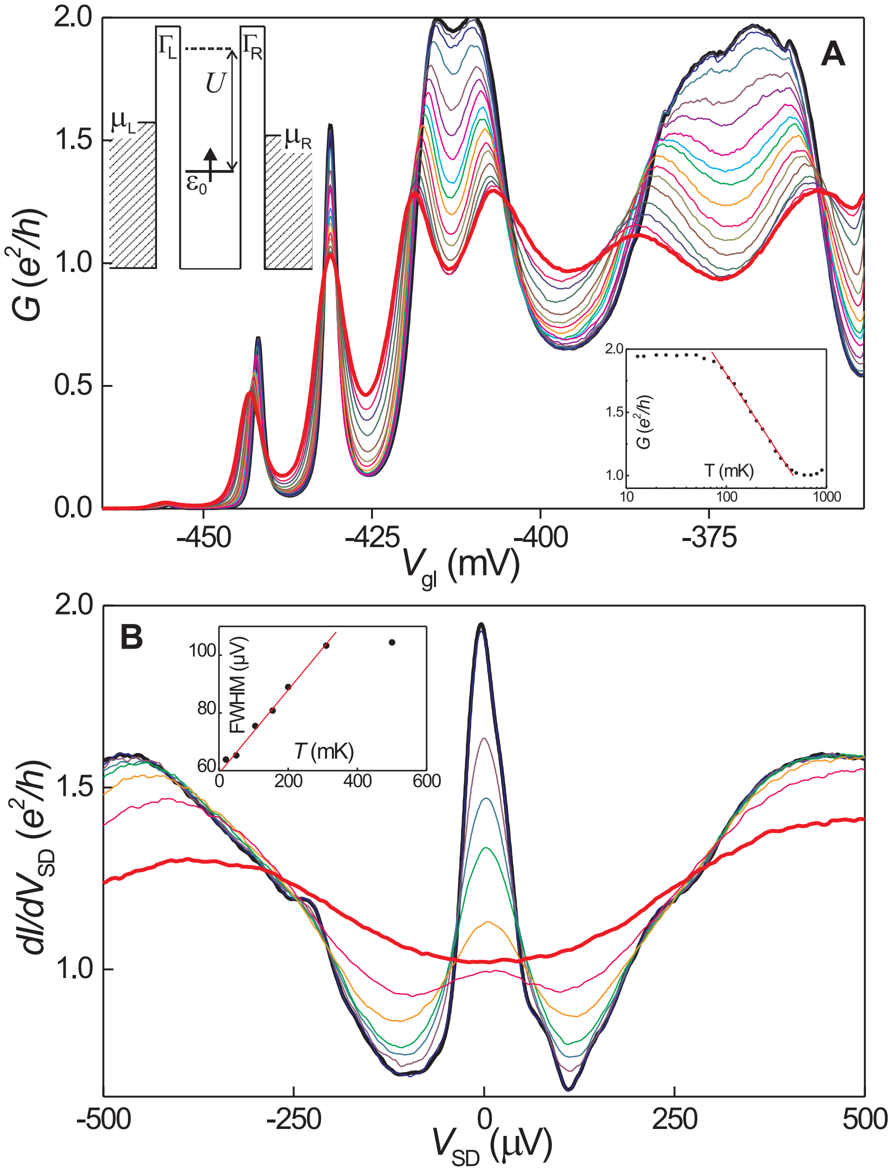

Figure 7.3: **(a)** Coulomb oscillations in G versus V_{gl} at $B = 0.4$ T for different temperatures. $T = 15$ mK (thick black trace) up to 800 mK (thick red trace). V_{gr} is fixed at -448 mV. The lower-right inset highlights the logarithmic T-dependence between 90 and 500 mK for $V_{gl} =$ -413 mV. The upper-left inset explains the symbols used in the text with $\Gamma = \Gamma_L + \Gamma_R$. Note that ε_0 is negative and measured from the Fermi level in the leads at equilibrium. **(b)** Differential conductance, dI/dV_{SD}, versus dc bias voltage between source and drain contacts, V_{SD}, for $T = 15$ mK (thick black trace) up to 900 mK (thick red trace), also at $V_{gl} =$ -413 mV and $B = 0.4$ T. The left inset shows that the width of the zero-bias peak, measured from the full-width-at-half-maximum (FWHM) increases linearly with T. The red line indicates a slope of 1.7 k_B/e, where k_B is the Boltzmann constant. At 15 mK the FWHM = 64 μV and it starts to saturate around 300 mK.

is several times larger than T_K, this expected one-parameter scaling is indeed observed in the inset to Fig. 7.2c.

7.5 Suppression of Kondo effect at $B = 0$ T

We now return to the significance of the applied magnetic field. Near $B = 0$ we observe in Fig. 7.1c regular Coulomb oscillations. Here, we find that the Kondo effect typically changes the valley conductance by only 20% [9]. In Fig. 7.1b a big change occurs at $B \sim 0.1$ T, reflecting the onset of a different transport regime, an observation that seems common for half-open quantum dots [21,22]. The magnetic field scale corresponds to adding a flux quantum to the area of the dot, implying, for instance, that time-reversal symmetry is broken. At $B = 0.4$ T, where we observe the unitary limit, the Zeeman spin splitting is much smaller than $k_B T_K$ and so it can safely be ignored. This magnetic field scale is also too small for the formation of Landau levels, which can introduce additional spin physics [22,23].

Recent calculations [24] indicate a spin polarization near $B = 0$ to enhanced values in line with earlier observations [25,26]. A small magnetic field reduces the spin values to $\frac{1}{2}$ for $N =$ odd and 0 for $N =$ even. Since higher spin states generally lead to a lower Kondo temperature, the Kondo effect can become much stronger by applying a magnetic field [27]. We believe this to be the origin for the transition in transport regimes near $B = 0.1$ T in Fig. 7.1b, although a thorough theoretical analysis would be desirable.

7.6 Aharonov-Bohm oscillations

So far, the upper arm of the ring was pinched off. To study how electron interference is affected by a Kondo quantum dot in the lower arm, we adjust the upper arm conductance to $\sim 2e^2/h$. In the gray-scale plot of Fig. 7.4a clear AB oscillations around $B = 0.4$ T are visible in the Kondo valley and the neighboring valleys. The period agrees well with a flux quantum, h/e, applied through the area enclosed by the ring. The AB oscillations demonstrate that at least part of the tunnel processes through the Kondo quantum dot is phase coherent. Our 2-terminal geometry only allows phase changes by multiples of π, due to symmetry reasons [28]. We observe a π phase flip at the left Coulomb peak, but no phase change is observed in the Kondo valley or at the right Coulomb peak (Fig. 7.4b). This behavior is different from the phase evolution described in [14]. A further study in a 4-terminal geometry should allow us to determine ar-

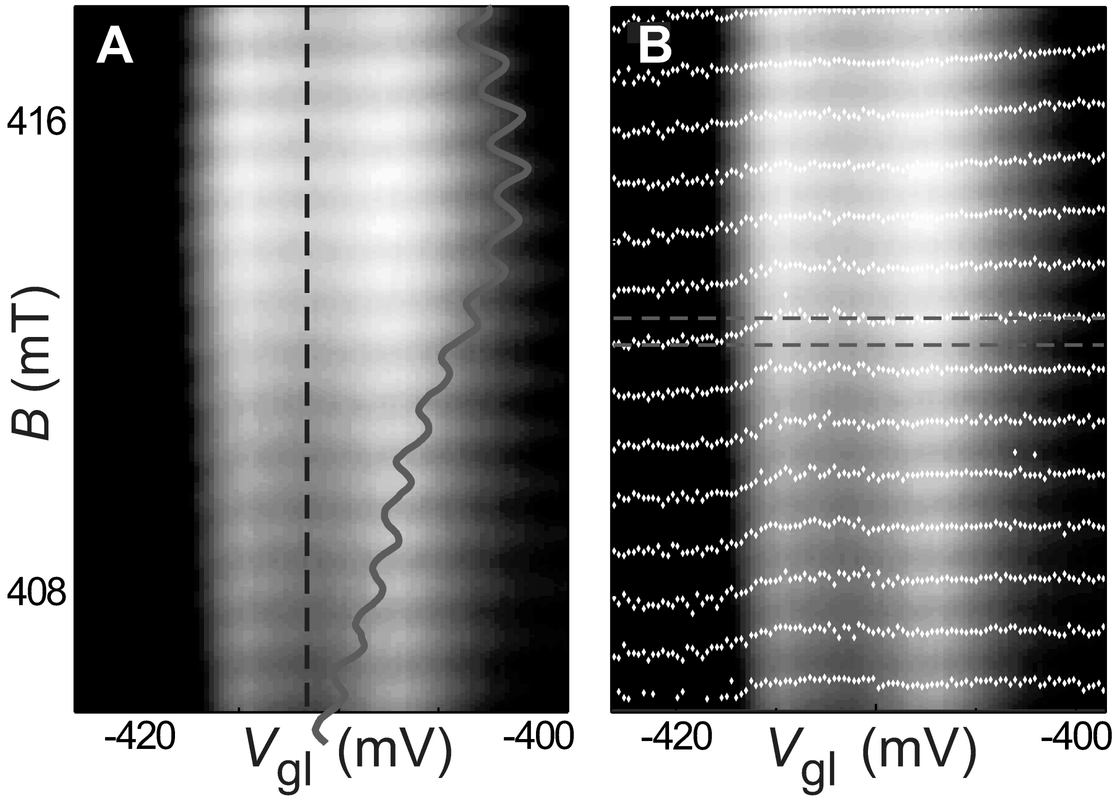

Figure 7.4: AB oscillations in the conductance through the ring containing the unitary Kondo quantum dot. In this measurement the conductance through the upper arm is set close to $2e^2/h$ in order to have approximately equal transmissions through both arms. **(a)** Gray-scale plot of the conductance, G, as function of V_{gl} and magnetic field B at 15 mK. Light (dark) corresponds to high (low) conductance. AB oscillations are observed over the whole gate voltage range. The red curve highlights the AB oscillations in the middle of the Kondo plateau (V_{gl} = -412 mV). The period of 0.87 mT corresponds well to a flux quantum, h/e, through the area enclosed by the ring. The modulation is 2-3% of the total conductance through the ring. **(b)** Same gray-scale plot with the AB conductance maxima indicated by white diamond symbols. A π phase flip is observed when stepping through the left Coulomb peak (e.g. along the red dashed lines). No phase change is observed in the Kondo valley or at the right Coulomb peak.

bitrary phase shifts in the transmission through a Kondo dot, as proposed in [29].

We thank E. Huizeling, T. Hayashi, S. Sasaki, D. Goldhaber-Gordon, Y. Meir, M. Eto, L. Glazman, Yu. Nazarov, and R. Schouten for their help. We acknowledge financial support from the Specially Promoted Research Grant-in-

Aid for Scientific Research, from the Ministry of Education, Science and Culture in Japan, from the Dutch Organization for Fundamental Research on Matter (FOM), from the NEDO joint research program (NTDP-98), and from the EU via a TMR network.

References

[1] J. Kondo, Prog. Theor. Phys. **32**, 37 (1964).

[2] L.I. Glazman and M.E. Raikh, JETP Lett. **47**, 452 (1988).

[3] T.K. Ng and P.A. Lee, Phys. Rev. Lett. **61**, 1768 (1988).

[4] A. Kawabata, J. Phys. Soc. Jpn. **60**, 3222 (1991).

[5] Y. Meir, N.S. Wingreen and P.A. Lee, Phys. Rev. Lett. **70**, 2601 (1993).

[6] N.S. Wingreen and Y. Meir, Phys. Rev. B **49**, 11040 (1994).

[7] W. Izumida, O. Sakai and Y. Shimizu, J. Phys. Soc. Jpn. **67**, 2444 (1998).

[8] D. Goldhaber-Gordon, H. Shtrikman, D. Mahalu, D. Abusch-Magder, U. Meirav and M.A. Kastner, Nature **391**, 156 (1998).

[9] S.M. Cronenwett, T.H. Oosterkamp and L.P. Kouwenhoven, Science **281**, 540 (1998).

[10] J. Schmid, J. Weis, K. Eberl and K. von Klitzing, Physica B **256-258**, 182 (1998).

[11] F. Simmel, R.H. Blick, J.P. Kotthaus, W. Wegscheider and M. Bichler, Phys. Rev. Lett. **83**, 804 (1999).

[12] S. Sasaki, S. De Franceschi, J.M. Elzerman, W.G. van der Wiel, M. Eto, S. Tarucha and L.P. Kouwenhoven, Nature **405**, 764 (2000).

[13] F.D.M. Haldane, Phys. Rev. Lett. **40**, 416 (1978).

[14] A. Yacoby, M. Heiblum, D. Mahalu and H. Shtrikman, Phys. Rev. Lett. **74**, 4047 (1995).

[15] The Kondo region around -372 mV does not develop a plateau at $2e^2/h$. In this gate voltage regime the tunnel coupling can be rather large so that charge fluctuations become important. This regime has been described by: L.I. Glazman, F.W.J. Hekking and A.I. Larkin, Phys. Rev. Lett. **83**, 1830 (1999), who predict a similar rounded-off Kondo region.

[16] $\varepsilon_0 = \alpha V_{gl}$ + constant, with $\alpha = C_{gl}/C_\Sigma = 45$ μeV/mV. Here, C_{gl} is the capacitance of the left gate electrode and C_Σ is the total capacicante of the

dot. Using this α-factor and the T-dependence of G, we obtain $U = 500$ μeV and $\Gamma = 240$ μeV.

[17] D. Goldhaber-Gordon, J. Göres, M.A. Kastner, H. Shtrikman, D. Mahalu and U. Meirav, Phys. Rev. Lett. **81**, 5225 (1998).

[18] Eq. 7.2 is an empirical fitting function to numerical renormalization group calculations reported in T.A. Costi, A.C. Hewson and V. Zlatić, J. Phys.: Condens. Matter **6**, 2519 (1994).

[19] From these fits we obtain $\Gamma = 231 \pm 12$ μeV taking $U = 500$ μeV. Since $\Gamma \gg k_B T_K$, we conclude that the low-energy properties are set by T_K, which is required for using Eq. 7.1, and that the dot is in the Kondo regime and not in the mixed-valence regime.

[20] A. Kaminski, Yu.V. Nazarov and L.I. Glazman, Phys. Rev. B **62**, 8154 (2000).

[21] S.M. Maurer, S.R. Patel, C.M. Marcus, C.I. Duruöz and J.S. Harris Jr., Phys. Rev. Lett. **83**, 1403 (1999).

[22] J. Schmid, J. Weis, K. Eberl and K. von Klitzing, Phys. Rev. Lett. **84**, 5824 (2000).

[23] C. Tejedor and L. Martin-Moreno, Phys. Rev. B **63**, 035319 (2001). The theory developed in this paper to describe the experimental results in [22], requires the formation of Landau levels, so it cannot describe our present results.

[24] M. Stopa, unpublished. The enhanced values for the spin polarization can sometimes reoccur at higher magnetic fields.

[25] S. Tarucha, D.G. Austing, T. Honda, R.J. van der Hage and L.P. Kouwenhoven, Phys. Rev. Lett. **77**, 3613 (1996).

[26] D.R. Stewart, D. Sprinzak, C.M. Marcus, C.I. Duruöz and J.S. Harris Jr., Science **278**, 1784 (1997).

[27] M. Stopa, W. Izumida and M. Eto, private communication.

[28] M. Büttiker, Phys. Rev. Lett. **57**, 176 (1986).

[29] U. Gerland, J. von Delft, T. Costi and Y. Oreg, Phys. Rev. Lett. **84**, 3710 (2000).

Chapter 8

Kondo effect in an integer-spin quantum dot

S. Sasaki, S. De Franceschi, J. M. Elzerman,
W. G. van der Wiel, M. Eto, S. Tarucha and L. P. Kouwenhoven

The Kondo effect is a key many-body phenomenon in condensed matter physics. It concerns the interaction between a localized spin and free electrons. Discovered in metals containing small amounts of magnetic impurities, it is now a fundamental mechanism in a wide class of correlated electron systems [1,2]. Control over single, localized spins has become relevant also in fabricated structures due to the rapid developments in nano-electronics [3,4]. Experiments have already demonstrated artificial realizations of isolated magnetic impurities at metallic surfaces [5,6], nanometer-scale magnets [7], controlled transitions between two-electron singlet and triplet states [8], and a tunable Kondo effect in semiconductor quantum dots [9-12]. Here, we report an unexpected Kondo effect realized in a few-electron quantum dot containing singlet and triplet spin states whose energy difference can be tuned with a magnetic field. This effect occurs for an even number of electrons at the degeneracy between singlet and triplet states. The characteristic energy scale is found to be much larger than for the ordinary spin-1/2 case.

This chapter has been published in Nature **405**, 764 (2000).

8.1 Kondo effect for odd and even N

Quantum dots are small electronic devices [13], which confine a well-defined number of electrons, N. The total spin is zero or an integer for N = even and half-integer for N = odd. The latter case constitutes the canonical example for the Kondo effect [14,15] when all electrons can be ignored, except for the one with the highest energy; i.e. the case of a single, isolated spin, $S = 1/2$ (see Fig. 8.1a). Although the energy level ε_0 is well below the Fermi energies of the two leads, Heisenberg uncertainty allows the electron on the dot to tunnel to one of the leads when it is replaced quickly by another electron. The time scale for such a co-tunneling process [16] is $\sim \hbar/U$, where $h = 2\pi\hbar$ is Planck's constant and U is the on-site Coulomb energy. Figure 8.1a illustrates that particle exchange by co-tunneling can effectively flip the spin on the dot. At low temperature, the coherent superposition of all possible co-tunneling processes involving spin flip can result in a time-averaged spin equal to zero. The whole system, i.e. quantum dot plus electrodes, forms a spin singlet. The energy scale for this singlet state is the Kondo temperature, T_K. In terms of density of states, a narrow peak with a width $\sim k_B T_K$ develops at the Fermi energy (k_B is Boltzmann's constant). Note that for N = even and $S = 0$, co-tunneling gives rise to a lifetime broadening of the confined state, without producing any Kondo resonance. Such even/odd behavior corresponding to no-Kondo/Kondo has been observed in recent experiments [9,10].

It is also possible that a quantum dot with N = even has a total spin $S = 1$; e.g. when the last two electrons have parallel spins. If the remaining $N - 2$ electrons can be ignored, this corresponds to a triplet state. Parallel spin filling is a consequence of Hund's rule occurring when the gain in exchange energy exceeds the spacing between single-particle states [8]. The spin of the triplet state can also be screened by co-tunneling events. These are illustrated in the center-left side of Fig. 8.1b. In contrast to single-particle states that are considered in the spin-1/2 Kondo problem, the spin triplet consists of three degenerate two-particle states. Co-tunneling exchanges only one of the two electrons with an electron from the leads. The total spin of the many-body Kondo state depends on how many modes in the leads couple effectively to the dot [17,18]. If there is only one mode, the screening is not complete and the whole system does not reach a singlet state. In this case the Kondo effect is called 'underscreened'. Calculations show that also for $S = 1$ a narrow Kondo resonance arises at the Fermi energy, however, the corresponding T_K is typically lower than in the case of $S = 1/2$ [19,20]. Some experiments have reported the absence of even/odd behavior [21,22], which may be related to the formation of higher spin states.

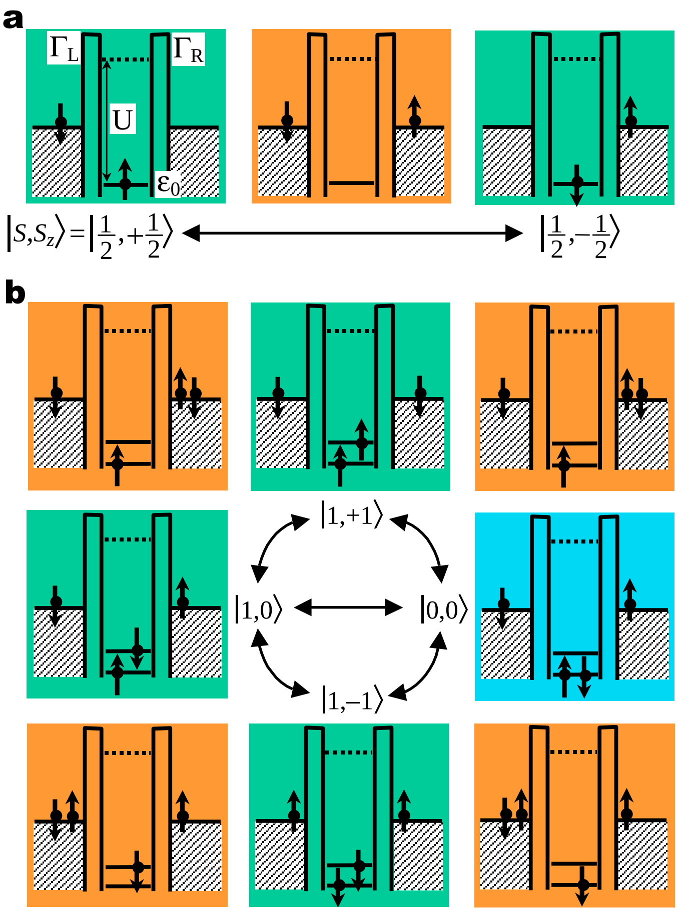

Figure 8.1: Spin-flip processes leading to ordinary and singlet-triplet Kondo effect in a quantum dot. **(a)** Co-tunneling event in a spin-1/2 quantum dot for N = odd. Only the highest-energy electron is shown, occupying a single spin-degenerate level, ε_0. (The case of two, or more, closely spaced levels has also been considered theoretically within the context of the spin-1/2 Kondo effect [30].) The green panels refer to $S_z = 1/2$ and -1/2 ground states, which are coupled by a co-tunneling event. The two tunnel barriers have tunneling rates Γ_R and Γ_L. In the Coulomb blockade regime ($|\varepsilon_0| \sim U$) adding or subtracting an electron from the dot implies an energy cost $\sim U$. Hence the intermediate step (orange panel) is a high-energy, virtual state. The spin-flip event depicted here is representative of a large number of higher-order processes which add up coherently such that the local spin is screened. This Kondo effect leads to an enhanced linear-response conductance at temperatures $T \lesssim T_K$. **(b)** Co-tunneling in an integer-spin quantum dot for N = even at a singlet-triplet degeneracy. Two electrons can share the same orbital with opposite spins (singlet state in the blue panel) or occupy two distinct orbitals in one of the three spin-triplet configurations (green panels). The different spin states are coupled by virtual states (orange panels). Similar to the spin-1/2 case, spin-flip events can screen the local magnetic moment. Note that an $S = 1$ Kondo effect only involves $|1, +1\rangle$, $|1, 0\rangle$ and $|1, -1\rangle$.

8.2 Enhanced Kondo effect at singlet-triplet degeneracy

Here, we investigate a quantum dot with $N =$ even where the last two electrons occupy a degenerate state of a spin singlet and a spin triplet. Figure 8.1b illustrates the different co-tunneling processes occurring in this special circumstance. Starting from $|S = 1, S_z = 1\rangle$, where S_z is the z-component of the total spin on the dot, co-tunneling via a virtual state $|1/2, 1/2\rangle$, can lead either to the triplet state $|1, 0\rangle$, or to the singlet state $|0, 0\rangle$. Via a second co-tunneling event the state $|1, -1\rangle$ can be reached. As for the $S = 1$ case, the local spin can fluctuate by co-tunneling events. By coupling to all triplet states, the singlet state enhances the spin exchange interaction between the dot and the leads, resulting in a higher rate for spin fluctuations. This particular situation yields a strong Kondo effect, which is characterized by an enhanced T_K. This type of Kondo effect has not been considered before, probably because a singlet-triplet degeneracy does not occur in magnetic elements. Recent scaling calculations indeed indicate a strong enhancement of T_K at the singlet-triplet degeneracy [23]. These workers also argue that the total spin of the many-body Kondo state behaves as in the case of $S = 1$.

Our quantum dot has the external shape of a rectangular pillar (see Fig. 8.2a,b) and an internal confinement potential close to a two-dimensional ellipse [24]. The tunnel barriers between the quantum dot and the source and drain electrodes are thinner than in our previous devices [8,24] such that co-tunneling processes are enhanced. Figure 2d shows the linear response conductance (dc bias voltage $V_{sd} = 0$) versus gate voltage, V_g, and magnetic field, B. Dark blue regions have low conductance and correspond to the regimes of Coulomb blockade for $N = 3$ to 10. In contrast to previous experiments [9-12] on the Kondo effect, all performed on lateral quantum dots with unknown electron number, here the number of confined electrons is precisely known. Red stripes represent Coulomb peaks as high as $\sim e^2/h$. The B-dependence of the first two lower stripes reflects the ground-state evolution for $N = 3$ and 4. Their similar B-evolution indicates that the 3rd and 4th electron occupy the same orbital state with opposite spin, which is observed also for $N = 1$ and 2 (not shown). This is not the case for $N =$ 5 and 6. The $N = 5$ state has $S = 1/2$, and the corresponding stripe shows a smooth evolution with B. Instead, the stripe for $N = 6$ has a kink at $B \approx 0.22$ T. From earlier analyses [24] and from measurements of the excitation spectrum at finite V_{sd} (discussed below) we can identify this kink with a transition in the ground state from a spin triplet to a spin singlet. Strikingly, at the triplet-singlet transition (at $B = B_0$ in Fig. 8.2c) we observe a strong enhancement of the conductance. In fact, over a narrow range around 0.22 T, the Coulomb gap for $N = 6$ has disappeared completely.

To explore this conductance anomaly, we show in Fig. 8.3a differential conductance measurements, dI/dV_{sd} vs V_{sd}, taken at $B = B_0$ and V_g corresponding to the dotted line in Fig. 8.2d. At $T = 14$ mK the narrow resonance around zero bias has a full-width-at-half-maximum, FWHM ≈ 30 μV. This is several times smaller than the lifetime broadening, $\Gamma = \Gamma_R + \Gamma_L \approx 150$ μV, as estimated from the FWHM of the Coulomb peaks. The height of the zero-bias resonance decreases logarithmically with T (see Fig. 8.3b). These are typical fingerprints of the Kondo effect. From FWHM $\approx k_B T_K$, we estimate $T_K \approx 350$ mK. We note that we can safely neglect the Zeeman spin splitting since $g\mu_B B_0 \approx 5$ μV $\ll k_B T_K$, implying that the spin triplet is in fact three-fold degenerate at $B = B_0$. This condition is essential to the Kondo effect illustrated in Fig. 8.1b. Alternative schemes have recently been proposed for a Kondo effect where the degeneracy of the triplet state is lifted by a large magnetic field [25,26].

For $N = 6$ we find markedly anomalous T-dependence only at the singlet-triplet degeneracy. Figure 8.3c shows the conductance versus V_g for different T. The upper panel is at $B = 0.12$ T. The two Coulomb peaks correspond to the transition from $N = 5$ to 6 and from $N = 6$ to 7. The small, short-period modulations superimposed on the Coulomb peaks are due to a weak charging effect in the upper part of GaAs pillar above the dot [27]. We will ignore this fine structure and focus on the general T-dependence. Upon increasing T, the valley conductance for $N = 6$ goes up due to thermally activated transport. A similar behavior is seen in the lower graph for $B = 0.32$ T. In contrast, at the singlet-triplet transition for $B = 0.22$ T we find an opposite T-dependence, again indicating the formation of a Kondo resonance. At the lowest T, the valley conductance is as high as 0.7 e^2/h, which is close to the height of the Coulomb peaks.

The T-dependence for $N = 5$ and 7 is visibly different than in the non-Kondo valley for $N = 6$ (lower panel). Such a difference is a manifestation of the ordinary spin-1/2 Kondo effect expected for $N =$ odd. Indeed the corresponding zero-bias resonances are clearly observed (see insets to Fig. 8.3a). Their height, however, is much smaller than for the singlet-triplet Kondo effect. There is also some indication for a triplet Kondo effect in the T-dependence for $N = 6$ at $B = 0.12$ T, although the associated zero-bias anomaly is not as apparent.

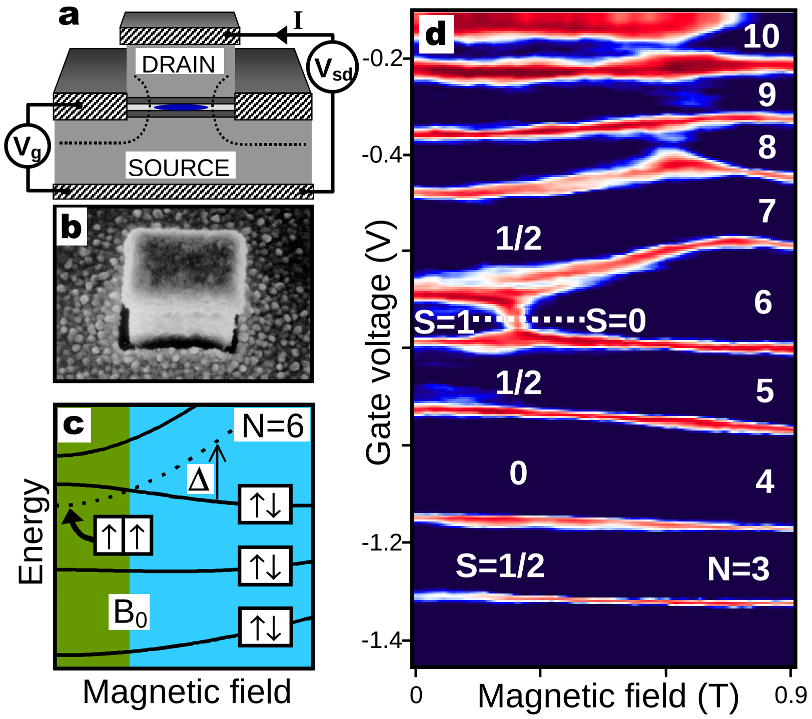

Figure 8.2: Sample description, energy spectrum and magnetic-field evolution of the ground state. **(a)** Cross-section of our rectangular quantum dot. The semiconductor material consists of an undoped AlGaAs(7nm)/InGaAs(12nm)/AlGaAs(7nm) double barrier structure sandwiched between n-doped GaAs source and drain electrodes. A gate electrode surrounds the pillar and is used to control the electrostatic confinement in the quantum dot. A dc bias voltage, V_{sd}, is applied between source and drain and current, I, flows vertically through the pillar. In addition to V_{sd}, we apply a modulation with rms amplitude $V_{ac} = 3\ \mu$V at 17.7 Hz for lock-in detection. The gate voltage, V_g, can change the number of confined electrons, N, one-by-one from ~ 10 at $V_g = 0$ to 0 at $V_g =$ -1.8 V. A magnetic field, B, is applied along the vertical axis. Temperature, T, is varied between 14 mK and 1 K. Our lowest effective electron temperature is 25 ± 5 mK. **(b)** Scanning electron micrograph of a quantum dot with dimensions 0.45×0.6 μm^2 and height of $\sim 0.5\ \mu$m. **(c)** Schematic energy spectrum. Solid lines represent the B-evolution of the first four orbital levels in a single-particle model. The dashed line is obtained by subtracting the two-electron exchange coupling from the fourth level. At the crossing between this dashed line and the third orbital level at $B = B_0$ the ground state for $N = 6$ undergoes a triplet-to-singlet transition. $B_0 \approx 0.22$ T with a slight dependence on V_g. We define Δ as the energy difference between the triplet and the singlet states. **(d)** Color-scale representation of the linear conductance versus V_g and B. Red stripes denote conductance peaks of height $\sim e^2/h$. Blue regions of low conductance indicate Coulomb blockade. The V_g-position of the stripes reflects the ground state evolution with B, for $N = 3$ to 10. The $N = 6$ ground state undergoes a triplet-to-singlet transition at $B_0 \approx 0.22$ T, which results in a conductance anomaly inside the corresponding Coulomb gap.

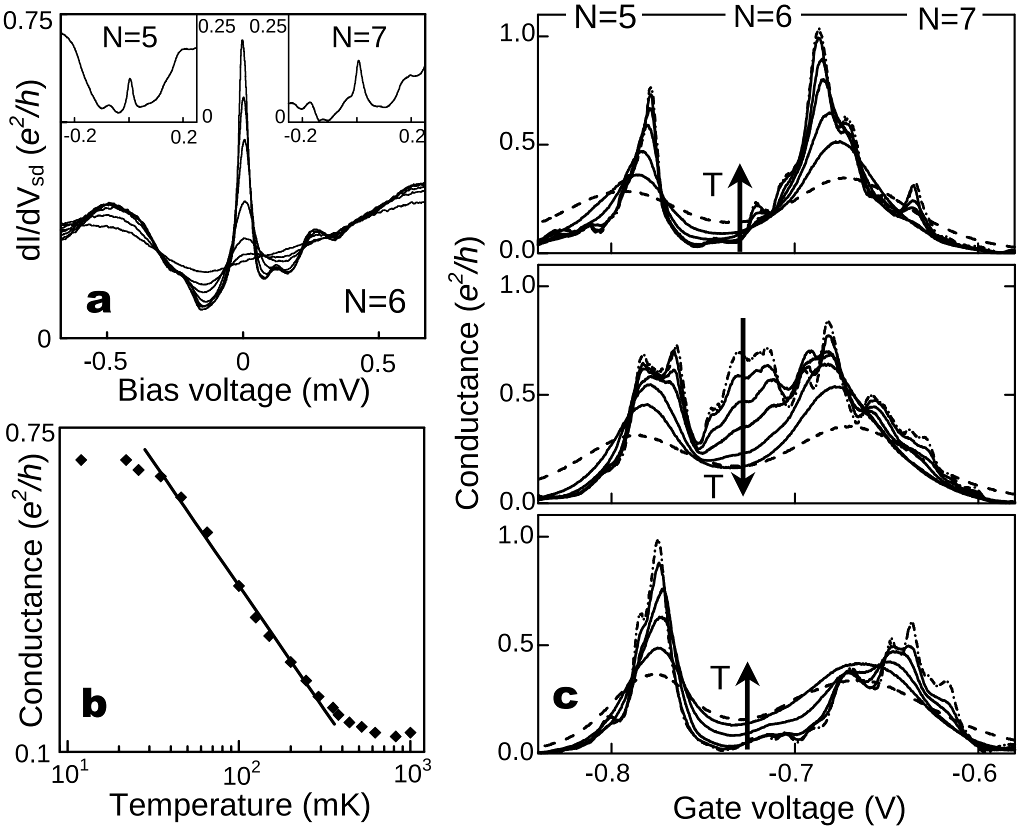

Figure 8.3: Zero-bias resonance and T-dependence of the conductance at the singlet-triplet degeneracy. **(a)** Kondo resonance at the singlet-triplet transition. The dI/dV_{sd} vs V_{sd} curves are taken at V_g = -0.72 V, B = 0.21 T and for T = 14, 65, 100, 200, 350, 520, and 810 mK. Insets to (a): Kondo resonances for N = 5 (left inset) and N = 7 (right inset), measured at V_g = -0.835 V and V_g = -0.625 V, respectively, and for B = 0.11 T and T = 14 mK. **(b)** Peak height of zero-bias Kondo resonance vs T as obtained from a (solid diamonds). The line demonstrates a logarithmic T-dependence, which is characteristic for the Kondo effect. The saturation at low T is probably due to electronic noise. **(c)** T-dependence of the linear conductance versus V_g for B = 0.12 T (spin-triplet ground state), B = 0.22 T (singlet-triplet degeneracy), and B = 0.32 T (spin-singlet ground state). Each panel shows 7 traces at T = 20 (dot-dashed line), 35, 70, 120, 260, 490 (solid lines), 1050 (dashed line) mK. The arrows emphasize the temperature dependence in the valley for N = 6.

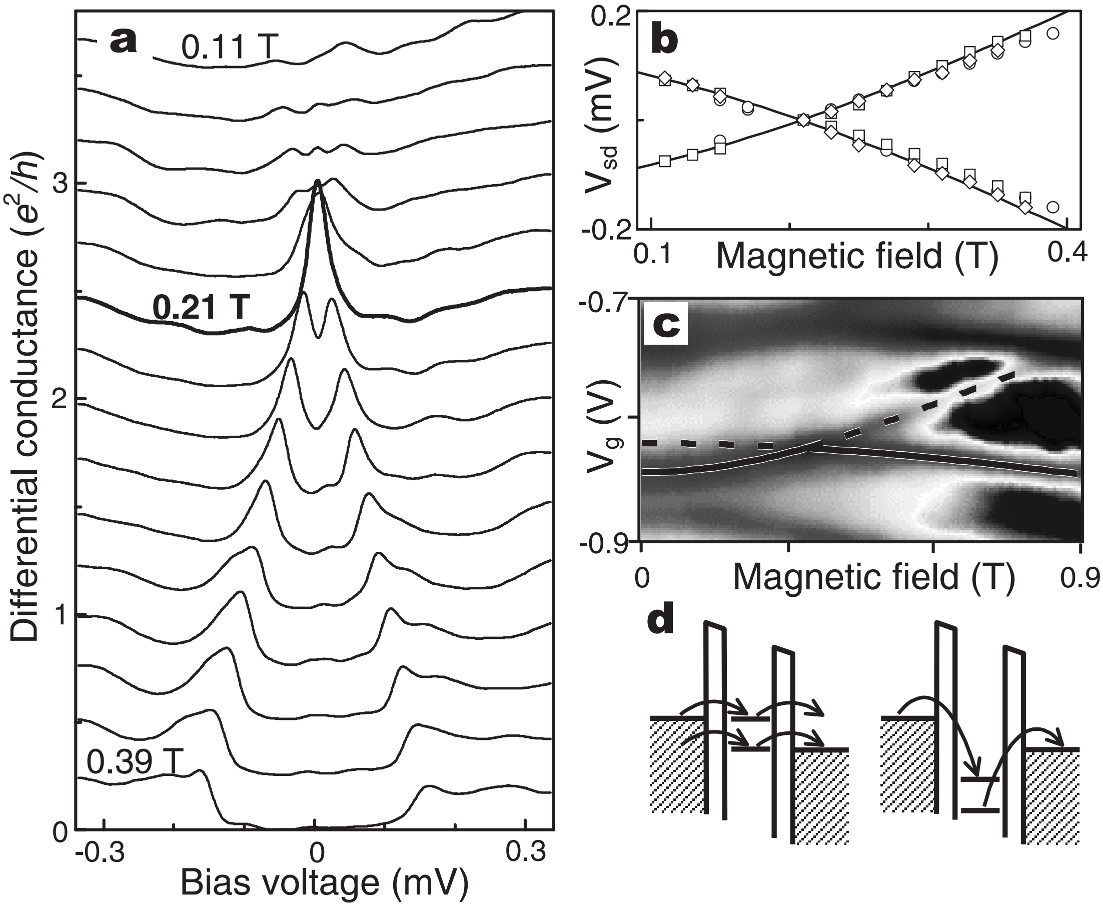

Figure 8.4: Singlet-triplet energy separation tuned by a magnetic field. **(a)** dI/dV_{sd} vs V_{sd} characteristics taken along the dotted line in Fig. 8.2d (V_g = -0.72 V) at equally spaced magnetic fields B = 0.11,0.13,...,0.39 T. Curves are offset by 0.25 e^2/h. **(b)** Extracted peak positions from dI/dV_{sd} curves in (a) versus B. Each symbol refers to a gate voltage taken between -0.72 and -0.70 V. **(c)** Gray-scale plot of dI/dV_{sd} measured at V_{sd} = 0.67 mV as a function of B and V_g. The solid line identifies the ground state, whereas the dashed line indicates the first excited state [8] for $N = 6$. From their difference we extract the singlet-triplet energy splitting, $\Delta(B)$, using a proportionality factor α = 6.7 meV/V to convert gate voltage into energy. The two solid lines in (b) represent $\pm\Delta(B)$ with a horizontal shift of 0.08 T to compensate for the shift of the singlet-triplet transition to a higher magnetic field in a high-bias measurement. **(d)** Energy diagrams for two different transport regimes, both with $eV_{sd} = \Delta$. Left: both ground and excited state lie between the two Fermi energies, so two channels are available for direct tunneling. The excitation spectrum in (c) is measured in this regime. Right: both ground and excited state lie below the Fermi levels of the leads (Coulomb blockade regime). Inelastic co-tunneling is illustrated, where one electron tunnels out of the lower energy state and another tunnels into the higher energy state.

8.3 Lifting the singlet-triplet degeneracy

We now investigate the effect of lifting the singlet-triplet degeneracy by changing B at a fixed V_g corresponding to the dotted line in Fig. 8.2d. Near the edges of this line, i.e. away from B_0, the Coulomb gap is well developed as denoted by the dark colors. The dI/dV_{sd} vs V_{sd} traces still exhibit anomalies, however, now at finite V_{sd} (see Fig. 8.4a). For $B = 0.21$ T we observe the singlet-triplet Kondo resonance at $V_{sd} = 0$. At higher B this resonance splits apart showing two peaks at finite V_{sd}. It is important to note that these peaks occur inside the Coulomb gap. They result from 'inelastic' co-tunneling events [16,28] where 'inelastic' refers to exchanging energy between quantum dot and electrodes (see right drawing in Fig. 8.4d). The upper traces in Fig. 8.4a, for $B < 0.21$ T, also show peak structures, although less pronounced.

In Fig. 8.4b we plot the positions of the dI/dV_{sd} peaks in the plane of V_{sd} and B. The symbols refer to different gate voltages indicating that these positions do not depend on V_g. The solid lines are obtained from the excitation spectrum measured (see Fig. 8.4c) in direct tunneling (explained on the left in Fig. 8.4d). They represent the measured B-dependence of the singlet-triplet energy difference, Δ. The fact that these independent measurements coincide implies that inelastic co-tunneling occurs when $eV_{sd} = \pm\Delta$. Note that this condition is independent of V_g, consistently with our observation. We believe that for small Δ ($\lesssim k_BT_K$) the split resonance reflects the singlet-triplet Kondo anomaly shifted to finite bias. This resembles the splitting of the Kondo resonance by the Zeeman effect [9,10,29], although on a very different B-scale. In the present case, the splitting occurs between two different multi-particle states and originates from the B-dependence of the orbital motion. For increasing Δ, the shift to larger V_{sd} induces spin-decoherence processes, which broaden and suppress the finite-bias peaks [29]. For $B \approx 0.39$ T the peaks have evolved into steps [28] which may indicate that the spin coherence associated with the Kondo effect has completely vanished.

We thank Yu.V. Nazarov, K. Maijala, S.M. Cronenwett, J.E. Mooij and Y. Tokura for discussions. We acknowledge financial support from the Specially Promoted Research, Grant-in-Aid for Scientific Research, from the Ministry of Education, Science and Culture in Japan, from the Dutch Organisation for Fundamental Research on Matter (FOM), from the NEDO joint research program (NTDP-98), and from the EU via a TMR network.

References

[1] A.C. Hewson, The Kondo Problem to Heavy Fermions (Cambridge University Press, Cambridge, 1993).

[2] D.L. Cox and M.B. Maple, Electronic pairing in exotic superconductors. Physics Today **48**, 32-40 (1995).

[3] G.A. Prinz, Magnetoelectronics. Science **282**, 1660-1663 (1998).

[4] D. Loss and D.P. DiVincenzo, Quantum computation with quantum dots. Phys. Rev. A **57**, 120-126 (1998).

[5] V. Madhavan, W. Chen, T. Jamneala, M.F. Crommie and N.S. Wingreen, Tunneling into a Single Magnetic Atom: Spectroscopic Evidence of the Kondo Resonance. Science **280**, 567-569 (1998).

[6] J. Li, W.-D. Schneider, R. Berndt and B. Delley, Kondo Scattering Observed at a Single Magnetic Impurity. Phys. Rev. Lett. **80**, 2893-2896 (1998).

[7] D.D. Awschalom and D.P. DiVincenzo, Complex Dynamics of Mesoscopic Magnets. Physics Today **48**, 43-48 (1995).

[8] S. Tarucha, D.G. Austing, Y. Tokura, W.G. van der Wiel and L.P. Kouwenhoven, Direct Coulomb and Exchange Interaction in Artificial Atoms. Phys. Rev. Lett. **84**, 2485-2488 (2000).

[9] D. Goldhaber-Gordon, H. Shtrikman, D. Mahalu, D. Abusch-Magder, U. Meirav and M.A. Kastner, Kondo effect in a single-electron transistor. Nature **391**, 156-159 (1998).

[10] S.M. Cronenwett, T.H. Oosterkamp and L.P. Kouwenhoven, A Tunable Kondo Effect in Quantum Dots. Science **281**, 540-544 (1998).

[11] J. Schmid, J. Weis, K. Eberl and K. v. Klitzing, A quantum dot in the limit of strong coupling to reservoirs. Physica B **256-258**, 182-185 (1998).

[12] F. Simmel, R.H. Blick, J.P. Kotthaus, W. Wegscheider and M. Bichler, Anomalous Kondo Effect in a Quantum Dot at Nonzero Bias. Phys. Rev. Lett. **83**, 804-807 (1999).

[13] L.P. Kouwenhoven, C.M. Marcus, P.L. McEuen, S. Tarucha, R.M. Westervelt and N.S. Wingreen, *Electron transport in quantum dots*, in Mesoscopic Electron Transport, edited by L.L. Sohn, L.P. Kouwenhoven and G. Schön, (Kluwer, Series E **345**, 1997), p.105-214.

[14] L.I. Glazman and M.E. Raikh, Resonant Kondo transparency of a barrier with quasilocal impurity states. JETP Lett. **47**, 452-455 (1988).

[15] T.K. Ng and P.A. Lee, On-site Coulomb repulsion and resonant tunneling. Phys. Rev. Lett. **61**, 1768-1771 (1988).

[16] D.V. Averin and Yu. V. Nazarov, Single Charge Tunneling, Proceedings of a NATO Advanced Study Institute, H. Grabert, M.H. Devoret, Eds., Les Houches, France, 5 March to 15 March, 1991 (Series B, **294**, 217, Plenum Press, New York, 1991).

[17] D.C. Mattis, Symmetry of ground state in a dilute magnetic metal alloy. Phys. Rev. Lett. **19**, 1478-1481 (1967).

[18] P. Nozières and A. Blandin, Kondo effect in real metals. J. Physique **41**, 193-211 (1980).

[19] Y. Wan, P. Phillips and Q. Li, Suppression of the Kondo effect in quantum dots by even-odd asymmetry. Phys. Rev. B **51**, 14782-14785 (1995).

[20] W. Izumida, O. Sakai and Y. Shimizu, Kondo Effect in Single Quantum Dot Systems - Study with NRG Method - J. Phys. Soc. Jpn. **67**, 2444-2454 (1998).

[21] S.M. Maurer, S.R. Patel, C.M. Marcus, C.I. Duruöz and J.S. Harris Jr., Coulomb Blockade Fluctuations in Strongly Coupled Quantum Dots. Phys. Rev. Lett. **83**, 1403-1406 (1999).

[22] J. Schmid, J. Weis, K. Eberl and K. von Klitzing, Absence of odd-even parity behaviour for Kondo resonances in quantum dots. Phys. Rev. Lett. **84**, 5824 (2000).

[23] M. Eto and Yu.V. Nazarov, Enhancement of Kondo effect in quantum dots with even number of electrons. Phys. Rev. Lett. **85**, (2000).

[24] D.G. Austing, S. Sasaki, S. Tarucha, S.M. Reimann, M. Koskinen and M. Manninen, Ellipsoidal deformation of vertical quantum dots. Phys. Rev. B **60**, 11514-11523 (1999).

[25] M. Pustilnik, Y. Avishai and K. Kikoin, Quantum dots with even number of electrons: Kondo effect in a finite magnetic field. Phys. Rev. Lett. **84**, 1756-1759 (2000).

[26] D. Giuliano and A. Tagliacozzo, Spin fractionalization of an even number of electrons in a quantum dot. Phys. Rev. Lett. **84**, 4677 (2000).

[27] U. Sivan *et al.*, Spectroscopy, Electron-Electron Interaction, and Level Statistics in a Disordered Quantum Dot. Europhys. Lett. **25**, 605-611 (1994).

[28] Y. Funabashi, K. Ohtsubo, M. Eto and K. Kawamura, Phase Relaxation and Non-Equilibrium Transport Properties through Multilevel Quantum Dot.

Jpn. J. Appl. Phys. **38**, 388-391 (1999).

[29] N.S. Wingreen and Y. Meir, Anderson model out of equilibrium: Noncrossing-approximation approach to transport through a quantum dot. Phys. Rev. B **49**, 11040-11052 (1994).

[30] T. Inoshita, A. Shimizu, Y. Kuramoto and H. Sakaki, Correlated electron transport through a quantum dot: The multiple-level effect. Phys. Rev. B **48**, 14725-14728 (1993).

Chapter 9

Electron cotunneling in a semiconductor quantum dot

S. De Franceschi, S. Sasaki, J. M. Elzerman,
W. G. van der Wiel, S. Tarucha and L. P. Kouwenhoven

We report transport measurements on a semiconductor quantum dot with a small number of confined electrons. In the Coulomb blockade regime, conduction is dominated by cotunneling processes. These can be either elastic or inelastic, depending on whether they leave the dot in its ground state or drive it into an excited state, respectively. We are able to discriminate between these two contributions and show that inelastic events can occur only if the applied bias exceeds the lowest excitation energy. Implications to energy-level spectroscopy are discussed.

This chapter has been published in Physical Review Letters **86**, 878-881 (2001).

9.1 Elastic and inelastic cotunneling

Quantum-dot devices consist of a small electronic island connected by tunnel barriers to source and drain electrodes [1]. Due to on-site Coulomb repulsion, the addition of an electron to the island implies an energy change $U = e^2/C$, where C is the total capacitance of the island. Hence the number of confined electrons is a well-defined integer, N, that can be controlled by varying the voltage on a nearby gate electrode. Transport of electrons through the dot is allowed only at the transition points where the N- and $(N+1)$-states are both energetically accessible. Otherwise, N is constant and current is strongly suppressed. This is known as Coulomb blockade [1]. At low temperature, however, higher-order tunneling events can become dominant. These are commonly known as *cotunneling* events since they involve the simultaneous tunneling of two or more electrons [2]. Electron cotunneling has received considerable attention over the last decade. Initially it was recognized as a limitation to the accuracy of single-electron devices. More recently, it has acquired a broader relevance, especially since an increasing activity has been focused on quantum dots with a deliberately enhanced tunnel coupling to their leads. These systems allow the investigation of high-order transport processes and many-body phenomena, such as the Kondo effect [3, 4]. The latter can be regarded as the result of a coherent superposition of higher-order cotunneling events. Here, we will focus on the lowest order contribution to cotunneling.

Previous experiments were performed with metallic islands [5, 6, 7] or large semiconductor dots [8, 9, 10], where the energy spectrum is essentially continuous and many levels contribute to cotunneling. Here, we study cotunneling through a small quantum dot where the energy levels are well separated, and where the absolute value of N is precisely known. A cotunneling event is called inelastic when it leaves the dot in an excited state. Otherwise it is classified as elastic. We identify two regimes: one consisting of elastic processes only, and one including both elastic and inelastic contributions. We note that the transition between these regimes can be sharper than the characteristic life-time broadening of the dot states. In such a case, the onset of inelastic cotunneling can be exploited to measure the energy spectrum of a quantum dot with improved resolution.

9.2 Charge stability diagram

The stability diagram of a generic quantum dot can be obtained by plotting the differential conductance ($\mathrm{d}I/\mathrm{d}V_{sd}$) as a function of bias, V_{sd}, and gate voltage, V_g. Coulomb blockade occurs within the diamond-shaped regions in Fig. 9.1a.

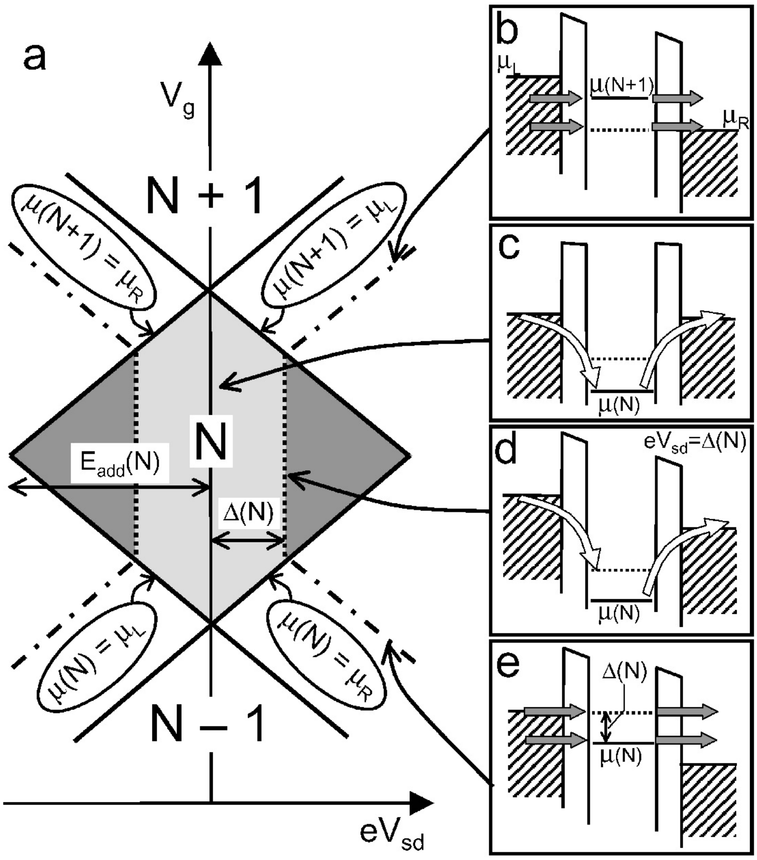

Figure 9.1: **(a)** Stability diagram in the plane of (V_{sd}, V_g). Angled lines correspond to *alignment* of a dot-state with the Fermi energy of the leads. In this case, first-order tunneling sets in, or is increased, as illustrated in **(b)** and **(e)**. In the light-grey area in (a), conduction is due to elastic cotunneling via virtual events as shown in **(c)**. For $eV_{sd} \geq \Delta(N)$, inelastic processes, illustrated in **(d)**, increase the cotunneling current (dark-grey areas). $\Delta(N)$ is the energy spacing between the ground state and the first excited state, which in (b)-(e) are represented by solid and dotted lines, respectively.

The diamond size is proportional to the addition energy, defined as $E_{add}(N) \equiv \mu_{dot}(N+1) - \mu_{dot}(N)$, where $\mu_{dot}(N)$ is the electrochemical potential of an N-electron dot. Inside the N-electron diamond, $\mu_{dot}(N) < \mu_L, \mu_R < \mu_{dot}(N+1)$, with μ_L, μ_R the Fermi energies of the leads. The diamond edges correspond to level alignment: $\mu_{dot}(N) = \mu_L$ or μ_R (see angled solid lines). This alignment determines the onset for first-order tunneling via the ground state of the dot, leading to a peak in $\mathrm{d}I/\mathrm{d}V_{sd}(V_{sd})$. The onset for first-order tunneling via the first excited state occurs at a somewhat higher bias (see dot-dashed lines in Fig. 9.1a, and the corresponding diagrams in Fig. 9.1b and 9.1e). These first-order processes have been exploited as a spectroscopic tool on the discrete energy spectrum of dots [1].

Here, we are interested in second-order tunneling of charge, which becomes more apparent when the tunnel coupling between the dot and the leads is enhanced. We neglect contributions from spin that could give rise to the Kondo effect. Elastic cotunneling is the dominant off-resonance process at low bias. It gives rise to current inside the Coulomb diamond (light-grey region in Fig. 9.1a). The corresponding two-electron process (Fig. 9.1c) transfers one electron from the left to the right lead, thereby leaving the dot in the ground state.

For $e|V_{sd}| \geq \Delta(N)$, where $\Delta(N)$ is the lowest on-site excitation energy for a constant N [11], similar two-electron processes can occur which drive the dot into an excited state. For instance, an electron can leave the dot from the ground state to the lowest Fermi sea, while another electron from the highest Fermi sea tunnels into the excited state (see Fig. 9.1d). Although this type of process is called inelastic [2], the total electron energy is conserved. The on-site excitation is created at the expense of the energy drop eV_{sd}. To first approximation, the onset of inelastic cotunneling yields a step in $\mathrm{d}I/\mathrm{d}V_{sd}(V_{sd})$ [12]. This step occurs when $e|V_{sd}| = \Delta(N)$, which is not or only weakly affected by V_g (see also Fig. 9.1c in Ref. [13]). As a result, inelastic cotunneling turns on along the vertical (dotted) lines in Fig. 9.1a. At the edge of the Coulomb diamond the condition for the onset of inelastic cotunneling connects to that for the onset of first-order tunneling via an excited state (dot-dashed lines).

9.3 Measuring the charge stability diagram in the few-electron regime

Our device has the external shape of a 0.5-μm-high pillar with a 0.6×0.45 $\mu\mathrm{m}^2$ rectangular base (inset to Fig. 9.2). It is fabricated from an undoped AlGaAs(7 nm)/InGaAs(12 nm)/AlGaAs(7 nm) double barrier heterostructure, sandwiched between n-doped GaAs source and drain electrodes [4]. The quantum dot is formed within the InGaAs layer. The lateral confinement potential is close to that of an ellipse [14]. Its strength is tuned by a negative voltage, V_g, applied to a metal gate surrounding the pillar. A dc bias voltage, V_{sd}, applied between source and drain, drives current vertically through the pillar. In addition, we apply a small bias modulation with rms amplitude $V_{ac} = 3$ μV at 17.7 Hz for lock-in detection. Measurements are carried out in a dilution refrigerator with a base temperature of 15 mK. We find an effective electron temperature $T_e = 25 \pm 5$ mK, due to residual electrical noise.

Figure 9.2 shows $\mathrm{d}I/\mathrm{d}V_{sd}$ in grey-scale versus (V_{sd},V_g) at 15 mK. Diamond-

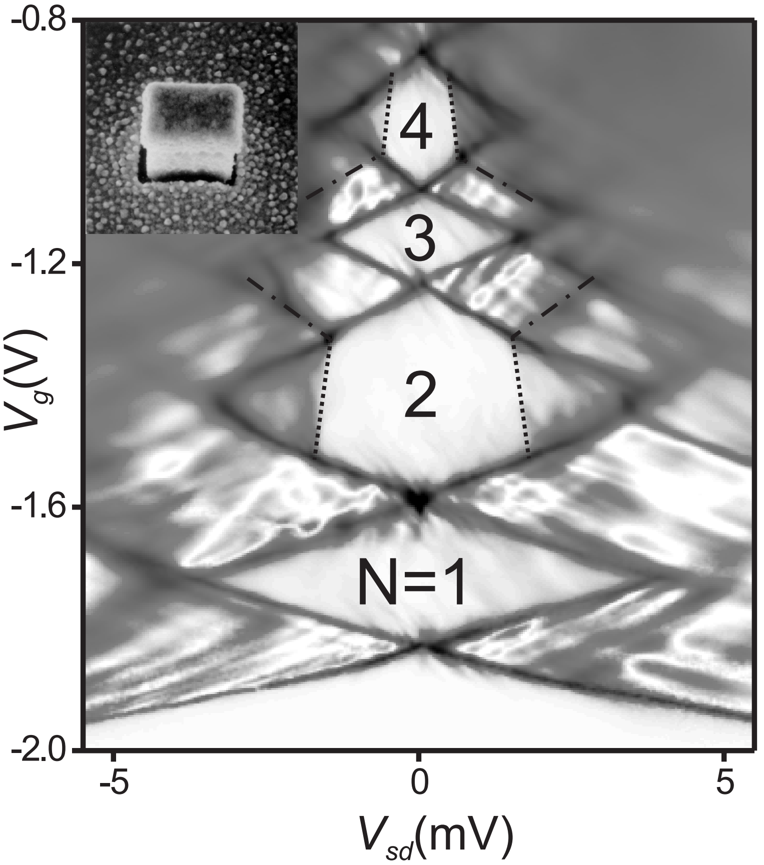

Figure 9.2: Measured stability diagram of our quantum dot at 15 mK and zero magnetic field. $\mathrm{d}I/\mathrm{d}V_{sd}$ is plotted in grey scale as a function of (V_{sd}, V_g). Dotted lines have been superimposed to highlight the onset of inelastic cotunneling. The dot-dashed lines indicate the onset of first-order tunneling via an excited state. Inset: scanning electron micrograph of the device.

shaped regions of low conductivity (light grey) identify the Coulomb blockade regimes for $N = 1$ to 4. The diamonds are delimited by dark narrow lines ($\mathrm{d}I/\mathrm{d}V_{sd} \sim e^2/h$) corresponding to the onset of first-order tunneling. For $N = 1$, as well as for $N = 3$, sub-gap transport is dominated by elastic cotunneling with no evidence for inelastic cotunneling. The differential conductance is uniformly low inside the Coulomb diamond. (Slight modulations are seen due to a weak charging effect in the GaAs pillar above the dot [15].) This is different for $N = 2$, where the onset of inelastic cotunneling is clearly observed. As argued before, this onset follows (dotted) lines, nearly parallel to the V_g axis [16]. At the diamond edges they connect to (dot-dashed) lines where first-order tunneling via an excited state sets in. Similar considerations apply to $N = 4$.

The different behavior observed for $N =$ *even* and $N =$ *odd* stems from the fact that inelastic cotunneling occurs only if $E_{add}(N) > \Delta(N)$, as apparent from Fig. 9.1a. In the case of non-interacting electrons, $E_{add}(N) = U(N)$ for $N = odd$ and $E_{add}(N) = U(N) + \Delta(N)$ for $N = even$, where $U(N)$ is the charging energy for N electrons; energy levels are spin degenerate and consecutively filled with pairs of electrons. This is a reasonable picture if the level spacing exceeds the exchange interaction energy [17]. In our small quantum dot the first three levels are indeed widely spaced as already discussed in Ref. [4]. For low N, $\Delta(N)$ exceeds not only the exchange energy but also $U(N)$. This implies that for $N = odd$, $\Delta(N)$ lies outside the Coulomb diamond (i.e. $\Delta(N) > E_{add}(N)$) and thus inelastic cotunneling is not observed. (Note that cotunneling between spin-degenerate states is an elastic process as initial and final state have the same energy.) For $N = even$, $\Delta(N)$ is always smaller than $E_{add}(N)$ and inelastic cotunneling can be observed.

9.4 Resonance width for first-and higher-order tunneling

We now discuss the difference in life-time broadening between first- and higher-order tunneling. At the onset of first-order tunneling a certain level is aligned to one of the Fermi energies. In this case, an electron can escape from the dot, which leads to a finite life-time broadening of the observed resonance by an amount $\hbar\Gamma$. Here, $\Gamma = \Gamma_L + \Gamma_R$, where Γ_L and Γ_R are the tunneling rates through the left and the right barrier, respectively. (Note that these rates are independent of V_{sd}, since our bias window (∼meV) is much smaller than the height of the AlGaAs tunnel barriers (≈50 meV).

The onset of inelastic cotunneling is also characterized by a width. In the zero-temperature limit, this is determined by the life-time broadening of the excited state. Two types of situations can occur. First, the excited state can be between μ_L and μ_R (see right inset to Fig. 9.3) so that inelastic cotunneling can be followed by first-order tunneling. Such a decay event leads to a life-time broadening of at least $\hbar\Gamma_R \approx \hbar\Gamma/2$. Second, the ground and excited state are both well below μ_L and μ_R, implying that only higher-order tunneling is allowed (see right inset to Fig. 9.4). Now, decay from the excited state can only rely on cotunneling. For this higher-order perturbation, the corresponding rate, Γ_{co}, is much smaller than Γ, leading to a reduced life-time broadening. To illustrate these arguments, we select different $\mathrm{d}I/\mathrm{d}V_{sd} - vs - V_{sd}$ traces and analyse their shape in detail.

Figure 9.3 shows two traces for $N = 2$, taken at 15 mK for gate voltages at the horizontal lines in the left inset. The dashed trace has several peaks. The

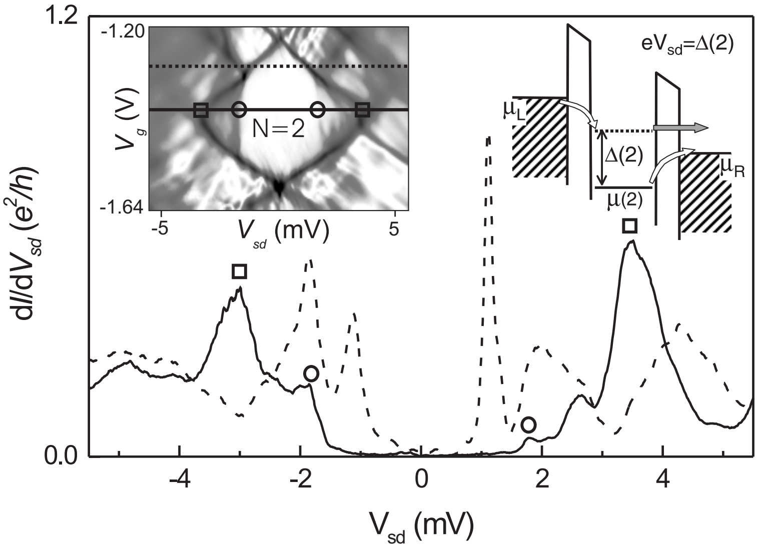

Figure 9.3: Differential conductance as a function of bias for $V_g = -1.40$ V (solid line) and $V_g = -1.30$ V (dotted line) at 15 mK. These traces are extracted from the stability diagram shown in the left inset. The horizontal lines indicate the corresponding V_g values. The right inset shows the qualitative energy diagram corresponding to the onset of inelastic cotunneling for $N = 2$. The horizontal arrow represents the possibility for an electron in the excited state to decay directly into the right lead by first-order tunneling.

two inner ones, at $|V_{sd}| \approx 1.1$ mV, correspond to first-order tunneling of the 3rd electron via the 3-electron ground state; i.e. $\mu_{dot}(3) = \mu_L$ or μ_R. The right (left) peak has a full width at half maximum (FWHM) of $\approx$200 ($\approx$400) μV. This is somewhat larger than the width, $\hbar\Gamma/e \simeq 150$ μV, measured in the zero-bias limit. Indeed a finite bias allows non-energy-conserving tunneling events leading to additional broadening. The most likely source for energy relaxation is acoustic-phonon emission [18]. The following pair of peaks, at $|V_{sd}| \approx 2$ mV, corresponds to the onset of first-order tunneling via the first excited state for $N = 2$ (see Fig. 9.1b). Because of the larger bias voltage, these peaks are visibly broader than the inner ones. Additional peak structures occur near the edges of the bias window. The origin of these peaks can not be precisely identified.

The solid trace contains structure from both first- and second-order tunneling. The peaks labeled by open squares arise from first-order tunneling at the edges of the Coulomb diamond (see left inset). Steps, labeled by open circles, identify the onset of inelastic cotunneling and correspond to the open circles in the left inset. Their different heights are probably due to a left-right asymmetry in the tunnel coupling to the leads. Their V_{sd}-position, which is symmetric around zero bias, provides a direct measure of $\Delta(2)$. The width of these steps is $\approx$150 μV [19]. Since $\Delta(2) \approx U(2)$, the first excited state lies unavoidably within the bias window when $|V_{sd}| = \Delta(2)/e$ and hence is allowed to decay into the lowest-energy lead (see the right inset to Fig. 9.3). As argued above, this situation leads to a step-width exceeding $\hbar\Gamma_R/e$, consistent with our finding.

Another structure occurs at $V_{sd} \approx 2.6$ mV and is probably due to the onset of inelastic cotunneling via the second excited state for $N = 2$. The corresponding line in the stability diagram is hardly visible due to its vicinity to the diamond edge.

9.5 Optimum energy resolution

To study inelastic cotunneling when both ground and excited state lie well below the Fermi energies of the leads (Fig. 9.1d) we need $\Delta(N) \ll E_{add}(N)$. To this aim we move to $N = 6$, since $\Delta(6)$ can be effectively tuned by a magnetic field applied along the vertical axis. We tune the field to 0.35 T, such that $\Delta(6) \approx 0.1$ meV, i.e. several times smaller than $E_{add}(6)$. From a previous study we know that the ground state is a spin singlet, and the first excited state is a spin triplet [4]. The $\mathrm{d}I/\mathrm{d}V_{sd} - vs - V_{sd}$ traces shown in Fig. 9.4 are taken at two different temperatures, but for the same V_g, at the horizontal line in the left inset. The solid trace (15 mK) shows a broad minimum around $V_{sd} = 0$, where transport is dominated by elastic cotunneling via the ground state (see also the light-grey region in the left inset). The differential conductance increases rapidly at the onset of inelastic cotunneling with a step-width of $\approx$20 μV, i.e. much smaller than $\hbar\Gamma/e$. This reduced width stems from the fact that the excited state can not decay directly into the lower energy lead (see right inset). The corresponding life-time broadening, $\hbar\Gamma_{co}$, can be estimated from the cotunneling current, I_{co}, at $V_{sd} = \Delta(6)/e$. We find $\hbar\Gamma_{co} = \hbar I_{co}/e \approx (\hbar/e) \int_0^{\Delta(6)/e} \mathrm{d}I/\mathrm{d}V_{sd}(V_{sd})$ $\mathrm{d}V_{sd} \simeq 10$ μeV, consistent with the observed step-width. At $T_e = 25$ mK the thermal broadening of the Fermi distribution functions leads to a step-width of $5.44 k_B T_e/e \simeq 12$ μeV [20]. Hence life-time broadening has been reduced here to the thermal limit.

The cotunneling onset in Fig. 9.4 shows a peak structure at low temperature (solid trace) in addition to the expected step structure. This is likely due to Kondo correlations, as discussed in Ref. [4]. On increasing temperature to 200 mK these Kondo correlations are suppressed such that only lowest order cotunneling contributes. This recovers the step structure (dashed trace).

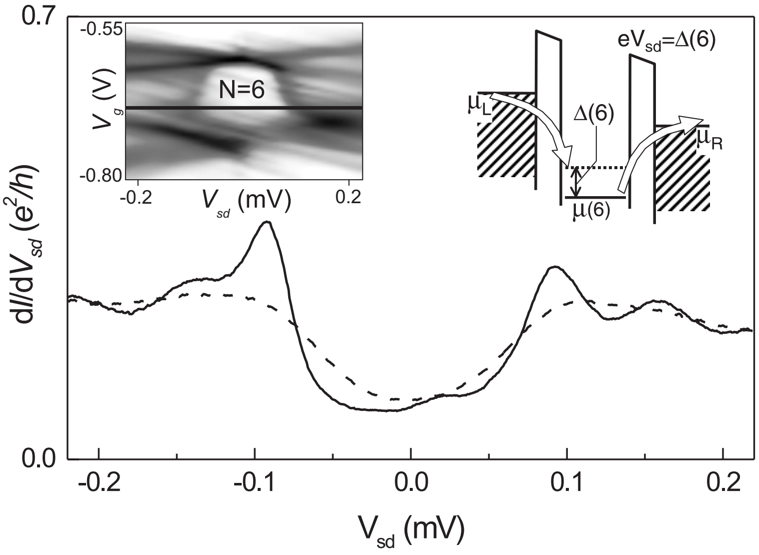

Figure 9.4: Differential conductance as a function of bias at $V_g = -0.685$ V. (Note that the bias window is much smaller than in Fig. 9.3.) The solid (dashed) line is taken at 15 mK (200 mK). Left inset: stability diagram at 15 mK, around the 6-electron Coulomb diamond. The horizontal line is at $V_g = -0.685$ V. Right inset: qualitative energy diagram corresponding to the onset of inelastic cotunneling for $N = 6$.

We thank Yu. V. Nazarov, M. R. Wegewijs, M. Eto, K. Maijala, and J. E. Mooij for discussions. We acknowledge financial support from the Specially Promoted Research, Grant-in-Aid for Scientific Research, from the Ministry of Education, Science and Culture in Japan, from the Dutch Organisation for Fundamental Research on Matter (FOM), from the NEDO joint research program (NTDP-98), and from the EU via a TMR network.

References

[1] L. P. Kouwenhoven, C. M. Marcus, P. L. McEuen, S. Tarucha, R. M. Westervelt, and N. S. Wingreen, in *Mesoscopic Electron Transport*, edited by L.L. Sohn, L. P. Kouwenhoven, and G. Schön, (Kluwer, Series E 345, 1997), p. 105-214.

[2] D. V. Averin and Yu. V. Nazarov, in *Single Charge Tunneling - Coulomb Blockade Phenomena in Nanostructures*, edited by H. Grabert and M. H. Devoret (Plenum Press and NATO Scientific Affairs Division, New York, 1992), p. 217.

[3] D. Goldhaber-Gordon *et al.*, Nature **391**, 156 (1998); Cronenwett *et al.*,

Science **281**, 540 (1998); Schmid *et al.*, Physica B **256-258**, 182 (1998).

[4] S. Sasaki *et al.*, Nature **405**, 764 (2000).

[5] L. J. Geerligs, D. V. Averin, and J. E. Mooij, Phys. Rev. Lett. **65**, 3037 (1990).

[6] T. M. Eiles *et al.*, Phys. Rev. Lett. **69**, 148 (1992).

[7] A. E. Hanna, M. T. Tuominen, and M. Tinkham, Phys. Rev. Lett. **68**, 3228 (1992).

[8] D. C. Glattli *et al.*, Z. Phys. B **85**, 375 (1991).

[9] C. Pasquier *et al.*, Phys. Rev. Lett. **70**, 69 (1993).

[10] S. M. Cronenwett *et al.*, Phys. Rev. Lett. **79**, 2312 (1997).

[11] In our definition $\Delta(N)$ is strictly positive. It reduces to the single-particle level spacing for non-interacting electrons (for instance, in the case of $N = 1$ and $N = 2$, $\Delta(N)$ is the spacing between the first two single-particle levels).

[12] Y. Funabashi *et al.*, Jpn. J. Appl. Phys. **38**, 388 (1999).

[13] J. Schmid *et al.*, Phys. Rev. Lett. **84**, 5824 (2000).

[14] D. G. Austing, *et al.*, Phys. Rev. B **60**, 11514 (1999).

[15] The top contact is obtained by deposition of Au/Ge and annealing at 400 °C for 30 s. This thermal treatment is gentle enough to prevent the formation of defects near the dot, but does not allow the complete suppression of the native Schottky barrier. The residual barrier leads to electronic confinement and corresponding charging effects in the GaAs pillar.

[16] V_g affects not only the bottom but also the shape of the confining potential. As a result, the level spacing (and hence $\Delta(N)$) depends weakly on V_g, leading to a non-zero angle between the dotted lines and the V_g axis.

[17] S. Tarucha *et al.*, Phys. Rev. Lett. **84**, 2485 (2000).

[18] T. Fujisawa *et al.*, Science **282**, 932 (1998).

[19] The step-width is estimated by taking the full width at half maximum of the corresponding peak (or dip) in $\mathrm{d}^2 I/\mathrm{d}V_{sd}^2(V_{sd})$.

[20] E. L. Wolf, *Principles of Electron Tunneling Spectroscopy*, (Oxford, New York, 1985) p. 438.

Summary

Electron spin and charge in semiconductor quantum dots

In this thesis the spin and charge degree of freedom of electrons in semiconductor lateral and vertical quantum dots are experimentally investigated. The lateral quantum dot devices are defined in a two-dimensional electron gas (2DEG) below the surface of a GaAs/AlGaAs heterostructure, by applying negative voltages to metallic gate electrodes on top of the heterostructure. The vertical quantum dots are sub-micron pillars surrounded by a metal gate electrode, fabricated in an In/Al/GaAs double-barrier heterostructure. Both kinds of quantum dots can be thought of as small 'boxes' filled with a controllable number of electrons. This box – the quantum dot – is coupled via tunnel barriers to reservoirs, with which electrons can be exchanged, and is coupled capacitively to one or more gate electrodes that allow the number of electrons on the dot to be varied. Due to the small dot size (typically $\sim$ 100 nm), comparable to the Fermi wavelength of the electrons, it exhibits a discrete energy spectrum.

There are two ways to probe the electrons in a quantum dot. The conventional approach is to use transport experiments. In this case, a bias voltage is applied over the device, and the resulting current flowing through it is measured. Alternatively, we can probe the dot via a nearby quantum point contact (QPC). This is a narrow channel with a small constriction, which has a conductance that can be very sensitive to the electrostatic environment. By applying a bias voltage over the constriction, and measuring the resulting current flowing through it, we can detect changes in the number of electrons on the nearby quantum dot.

In the first part of this thesis, we describe experiments aimed at using a single electron trapped in a lateral quantum dot as a spin qubit, building block of a quantum computer. The first step towards this goal is the development of the spin qubit 'hardware': a device consisting of two coupled quantum dots that can be filled with one electron spin each, flanked by two QPCs. We use both transport measurements as well as QPC charge detection to demonstrate control

over the precise charge configuration of the double dot. Even in the few-electron regime, parameters such as the inter-dot coupling remain fully tunable.

Using a QPC, we can determine all relevant parameters of the quantum dot even when it is coupled very weakly to only one reservoir. In this regime, inaccessible to conventional transport experiments, we determine the tunnel rate between the dot and the reservoir. By measuring changes in the effective tunnel rate, we can determine the excited states of the dot. We apply this technique to measure the Zeeman splitting between the proposed qubit states, i.e. the spin-up and spin-down state of a single electron spin in a large magnetic field.

Pushing the QPC charge detector to a faster regime ($\sim$ 100 kHz), we are able to detect single electron tunneling events in real-time. By tuning the gate voltages such that the number of electrons on the dot can vary between zero and one, stochastic tunneling of electrons between the dot and the reservoir is observed. After applying voltage pulses to a gate electrode, we obtain the tunnel rate between the dot and the reservoir. We also determine the dominant contributions to the noise in the QPC current, and estimate the ultimate speed and sensitivity that could be achieved with this very simple method of charge detection.

We then develop a technique to perform single-shot measurement of the spin orientation of an individual electron in a quantum dot. This is done by combining fast QPC charge detection with ‘spin-to-charge conversion’. The spin-to-charge conversion relies on a large Zeeman splitting between the spin-up and spin-down spin orientation, induced by a magnetic field parallel to the heterostructure surface. Due to this energy difference, a spin-up electron is trapped on the dot, whereas a spin-down electron has enough energy to escape. Measurement of the charge on the dot then reveals the spin. This constitutes a fully electrical technique to read out a spin qubit. We use it to determine the relaxation time of a single spin, and find a value of 0.85 ms at a magnetic field of 8 T, which becomes shorter at increasing magnetic field. This very long time indicates that the electron spin degree of freedom is only weakly disturbed by the environment. We conclude part one of this thesis with an overview of the progress made towards creating a spin qubit.

Part two focusses on quantum dots that are strongly coupled to the reservoirs. In this case, higher-order tunneling processes such as cotunneling and the Kondo effect can become important. The Kondo effect is a many-body phenomenon arising from the interaction between a localized spin and the spin of free conduction electrons. A strong Kondo effect is observed at small magnetic field in a lateral quantum dot. The Coulomb blockade is overcome completely by the Kondo effect and the conductance reaches the unitary-limit value of $2e^2/h$. The experimental Kondo temperature shows very good agreement with the spin-1/2 Anderson impurity model throughout the Kondo regime. It is also shown that phase-coherent transport through a Kondo quantum dot is possible, by measuring electron interference in an Aharonov-Bohm ring with the dot embedded in one of its arms.

In a vertical quantum dot containing six electrons, we observe an unexpected Kondo effect at the transition between a spin singlet and a spin triplet ground state. The characteristic energy scale is found to be much larger than for the ordinary spin-1/2 case in this system. By tuning the singlet-triplet splitting, the effect is shifted to higher energy.

Finally, the thesis concludes with an investigation of elastic and inelastic cotunneling in a few-electron vertical quantum dot containing two to six electrons.

Jeroen Elzerman
August 2004

Samenvatting

Elektron spin en lading in halfgeleider quantum dots

In dit proefschrift worden de spin- en ladingsvrijheidsgraad van elektronen in halfgeleider laterale en vertikale quantum dots experimenteel onderzocht. De laterale quantum dots zijn gedefinieerd in een tweedimensionaal elektronen gas (2DEG) beneden het oppervlak van een GaAs/AlGaAs heterostruktuur, door negatieve voltages aan te brengen op metalen 'gate' elektroden bovenop de heterostruktuur. De vertikale quantum dots zijn sub-micron pilaartjes omringd door een metalen gate elektrode, gefabriceerd in een In/Al/GaAs dubbel-barrière heterostruktuur. Beide typen quantum dot kunnen worden beschouwd als kleine 'doosjes' gevuld met een controleerbaar aantal elektronen. Dit doosje – de quantum dot – is via tunnel barrières gekoppeld aan reservoirs, waarmee elektronen kunnen worden uitgewisseld, en het is capacitief gekoppeld naar één of meer gate elektroden waarmee het elektronenaantal op de dot gevarieerd kan worden. Vanwege de kleine afmetingen van de dot (typisch ~ 100 nm), vergelijkbaar met de Fermi golflengte van de elektronen, vertoont de dot een discreet energie spectrum.

Er bestaan twee manieren om de elektronen in een quantum dot te onderzoeken. De conventionele aanpak is om transportmetingen te verrichten. In dit geval wordt een 'bias' voltage aangelegd over de struktuur, en wordt de resulterende stroom die er doorheen vloeit gemeten. Als alternatief kunnen we de dot onderzoeken via een nabij quantum punt contact (QPC). Dit is een smal kanaaltje met een kleine vernauwing die heel gevoelig kan zijn voor de elektrostatische omgeving. Door een bias voltage aan te leggen over de vernauwing en de resulterende stroom te meten, kunnen we veranderingen in het aantal elektronen op de nabije quantum dot meten.

In het eerste deel van dit proefschrift beschrijven we experimenten met als doel om een enkel elektron opgesloten in een quantum dot te gebruiken als spin qubit, bouwsteen van een quantum computer. De eerste stap naar dit doel is het ontwikkelen can de spin qubit 'hardware': een struktuur bestaande uit twee gekoppelde quantum dots die beide gevuld kunnen worden met één elektron, en geflankeerd door twee QPC's. We gebruiken zowel transportmetingen als QPC ladinsdetectie om controle over de precieze ladingsconfiguratie van de dubbele dot te demonstreren. Zelfs in het enkel-elektron regime blijven parameters als de inter-dot koppeling volledig instelbaar.

Met gebruikmaking van een QPC kunnen we alle relevante parameters van de quantum dot bepalen, zelfs indien die zeer zwak gekoppeld is naar maar één reservoir. In dit regime, niet toegankelijk voor conventionele transport experimenten, bepalen we de tunnelfrequentie tussen de dot en het reservoir. Door veranderingen in de effectieve tunnelfrequentie te meten, kunnen we de aangeslagen toestanden van de dot bepalen. We passen deze techniek toe bij het meten van de Zeeman splitsing tussen de voorgestelde qubit toestanden, d.w.z. de spin-op en spin-neer toestand van een enkele elektron spin in een sterk magnetisch veld.

Door de QPC ladingsdetector naar een sneller regime te stuwen (~ 100 kHz) zijn we in staat om individuele tunnelgebeurtenissen tijdsopgelost te detecteren. Door de gate voltages zo in te stellen dat het aantal elektronen op de dot kan variëren tussen nul en één, wordt stochastisch tunnelen tussen de dot en het reservoir waargenomen. Na aanbrengen van voltage-pulsen op de gate elektrode verkrijgen we de tunnelfrequentie tussen de dot en het reservoir. We bepalen ook de dominante contributies in de ruis van de QPC stroom, en schatten de uiteindelijke snelheid en gevoeligheid die met deze simpele ladingsdetectie methode kunnen worden bereikt.

Vervolgens ontwikkelen we een techniek om de spin oriëntatie van een enkel elektron in een quantum dot uit te lezen in een enkele meting. Dit wordt bereikt door snelle QPC ladingsdetectie te combineren met 'spin-naar-ladings conversie'. De 'spin-naar-ladings conversie' berust op een grote Zeeman splitsing tusseen de spin-op en spin-neer spin oriëntatie, die veroorzaakt wordt door een magnetisch veld parallel aan het oppervlak van de heterostructuur. Door dit energieverschil is een spin-op elektron opgesloten in de dot, terwijl een spin-neer elektron genoeg energie heeft om te ontsnappen. Meting van de lading op de dot onthult vervolgens de spin. Dit vormt een volledig elektrische techniek om een spin qubit uit te lezen. Wij gebruiken deze om de relaxatietijd van een enkele spin te bepalen, en vinden een waarde van 0.85 ms bij een magnetisch veld van 8 T, die kleiner wordt bij hoger veld. Deze zeer lange tijd toont aan dat de spin vrijheidsgraad maar weinig verstoord wordt door de omgeving. We concluderen deel één van dit proefschrift met een overzicht van de voortgang die is gemaakt op weg naar het maken van een spin qubit.

Deel twee richt zich op quantum dots die sterk zijn gekoppeld met de reservoirs. In dit geval kunnnen hogere-order tunneleffecten zoals cotunneling en het Kondo effect belangrijk worden. Het Kondo effect is een veel-deeltjes fenomeen dat voortkomt uit de interactie tussen een gelocaliseerde spin en de spin van vrije geleidingselektronen. Een sterk Kondo effect wordt waargenomen bij zwak veld in een laterale quantum dot. De Coulomb blokkade wordt volledig overwonnen door het Kondo effect en de geleiding bereikt de unitaire-limiet waarde van $2e^2/h$. De experimentele Kondo temperatuur vertoont goede overeenstemming met het spin-1/2 Anderson onzuiverheid model in het hele Kondo regime. Er wordt ook aangetoond dat fase-coherent transport door een Kondo dot mogelijk is, door elektron interferentie te meten in een Aharonov-Bohm ring met een dot in één van de armen.

In een verticale quantum dot die zes elektronen bevat observeren we een onverwacht Kondo effect bij de overgang tussen een spin singlet en een spin triplet grondtoestand. De karakteristieke energieschaal blijkt veel groter te zijn dan in de normale spin-1/2 situatie in dit systeem. Door de singlet-triplet energie te veranderen, wordt het effect naar hogere energie verschoven.

Tenslotte eindigt het proefschrift met het onderzoeken van elastisch en inelastisch cotunnelen in een verticale quantum dot die twee tot zes elektronen bevat.

Jeroen Elzerman
augustus 2004

Curriculum Vitae

Jeroen Martijn Elzerman

08-04-1973	Born in Leiderdorp, the Netherlands.
1985-1991	Secondary school at the Gymnasium Celeanum in Zwolle.
1991-1999	M.Sc. Applied Physics, Delft University of Technology. Graduate research in the Quantum Transport group of prof.dr.ir. J.E. Mooij. Subject: Kondo effects in semiconductor quantum dots
200-2004	Ph.D research at Delft University of Technology under supervision of prof.dr.ir. L.P. Kouwenhoven Subject: Semiconductor few-electron quantum dots as spin qubits

List of publications

1. *Real-time detection of single electron tunneling using a quantum point contact*
   L. M. K. Vandersypen, J. M. Elzerman, R. N. Schouten, L. H. Willems van Beveren, R. Hanson, and L. P. Kouwenhoven, Submitted to Applied Physics Letters (2004).

2. *Semiconductor few-electron quantum dot operated as a bipolar spin filter*
   R. Hanson, L. M. K. Vandersypen, L. H. Willems van Beveren, J. M. Elzerman, I. T. Vink, and L. P. Kouwenhoven, Submitted to Physical Review Letters (2004). See also http://xxx.lanl.gov/abs/cond-mat/0311414 (2003).

3. *Single shot read-out of an individual electron spin in a quantum dot*
   J. M. Elzerman, R. Hanson, L. H. Willems van Beveren, B. Witkamp, L. M. K. Vandersypen, and L. P. Kouwenhoven, Nature **430**, 431 (2004).

4. *Measurement efficiency and n-shot read out of spin qubits*
   H. A. Engel, V. N. Golovach, D. Loss, L. M. K. Vandersypen, J. M. Elzerman, R. Hanson, and L. P. Kouwenhoven, Physical Review Letters **93**, 106804 (2004).

5. *Excited-state spectroscopy on a nearly-closed quantum dot via charge detection*
   J. M. Elzerman, R. Hanson, L. H. Willems van Beveren, L. M. K. Vandersypen, and L. P. Kouwenhoven, Applied Physics Letters 84, 4617 (2004).

6. *Zeeman energy and spin relaxation in a one-electron quantum dot*
   R. Hanson, B. Witkamp, L. M. K. Vandersypen, L. H. Willems van Beveren, J. M. Elzerman, and L. P. Kouwenhoven, Physical Review Letters **91**, 196802 (2003).

7. *Few-electron quantum dot circuit with integrated charge read-out*
   J. M. Elzerman, R. Hanson, J. S. Greidanus, L. H. Willems van Beveren, S. De Franceschi, L. M. K. Vandersypen, S. Tarucha, and L. P. Kouwenhoven, Physical Review B **67** 161308 (2003).

8. *Electro-magnetic Aharonov-Bohm effect in a 2-D electron gas ring*
   W. G. van der Wiel, Yu. V. Nazarov, S. De Franceschi, T. Fujisawa, J. M. Elzerman, E. W. G. M. Huizeling, S. Tarucha, and L. P. Kouwenhoven, Physical Review B **67** 033307 (2003).

9. *Electron transport through double quantum dots.*
W. G. van der Wiel, S. De Franceschi, J. M. Elzerman, T. Fujisawa, S. Tarucha, and L. P. Kouwenhoven, Reviews of Modern Physics **75**, No. 1, 1-22 (2003).

10. *Quantum computing with electron spins in quantum dots*
L. M. K. Vandersypen, R. Hanson, L. H. Willems van Beveren, J. M. Elzerman, J. S. Greidanus, S. De Franceschi, and L. P. Kouwenhoven, in *Quantum Computing and Quantum Bits in Mesoscopic Systems*, Kluwer Academic/Plenum Publishers (2003).
See also http://xxx.lanl.gov/abs/quant-ph/0207059 (2002).

11. *Out-of-equilibrium Kondo effect in a mesoscopic device*
S. De Franceschi, R. Hanson, W. G. van der Wiel, J. M. Elzerman, J. J. Wijpkema, T. Fujisawa, S. Tarucha, and L. P. Kouwenhoven, Physical Review Letters **89**, 156801 (2002).

12. *Low temperature transport in dual-gated SETs fabricated by selective area metalorganic vapor phase epitaxy*
J. Motohisa, W. G. van der Wiel, J. M. Elzerman, S. De Franceschi, F. Nakajima, Y. Ogasawara, T. Fukui, and L. P. Kouwenhoven, Physica E **13**, 687-690 (2002).

13. *Fabrication and low-temperature transport properties of selectively grown dual-gated single-electron transistors*
J. Motohisa, F. Nakajima, T. Fukui, W. G. van der Wiel, J. M. Elzerman, S. De Franceschi, and L. P. Kouwenhoven, Applied Physics Letters **80**, 2797-2799 (2002).

14. *Two-stage Kondo effect in a quantum dot at high magnetic field*
W. G. van der Wiel, S. De Franceschi, J. M. Elzerman, S. Tarucha, L. P. Kouwenhoven, J. Motohisa, F. Nakajima, and T. Fukui, Physical Review Letters **88**, 126803 (2002).

15. *Spin effects in semiconductor quantum dot structures*
S. Tarucha, D. G. Austing, S. Sasaki, Y. Tokura, J.M. Elzerman, W.G. van der Wiel, S. de Franceschi, and L. P. Kouwenhoven, Physica E **10**, 45-51 (2001).

16. *Kondo-effect in kwantumdots*
Wilfred van der Wiel, Jeroen Elzerman en Leo Kouwenhoven, Natuur en Techniek, Feb. 2001, p. 44-49 (2001).

17. *Electron cotunneling in a semiconductor quantum dot*
S. De Franceschi, S. Sasaki, J. M. Elzerman, W. G. van der Wiel, S. Tarucha, and L. P. Kouwenhoven, Physical Review Letters **86**, 878-881 (2001).

18. *Electron transport through quantum dots: an unusual Kondo effect*
S. De Franceschi, S. Sasaki, J. M. Elzerman, W. G. van der Wiel, M. Eto, S. Tarucha, and L. P. Kouwenhoven, Proceedings of the NATO Advanced Research Workshop on Size Dependent Magnetic Scattering Pcs, Hongarije, p. 153-161, Kluwer Academic Publishers, Dordrecht, ISBN 1-4020-0400-1 (2001).

19. *Multi-level Kondo regimes in a quantum dot*
S. De Franceschi, W. G. van der Wiel, T. Fujisawa, J. M. Elzerman, W. Izumida, S. Tarucha, and L. P. Kouwenhoven, in: Proceedings of the 36th Rencontres de Moriond 2001 Conference on Electronic Correlations: from meso- to nanophysics T. Martin, G. Montambaux and J. Tran Thanh Van (eds.): Les Arcs, France, January 20-27, 361-366 (2001).

20. *Novel Kondo anomaly in quantum dots*
S. Tarucha, D. G. Austing, S. Sasaki, T. Fujisawa, Y. Tokura, J. M. Elzerman, W. G. van der Wiel, S. De Franceschi, and L. P. Kouwenhoven, Journal of Materials Science and Engineering, B **84**, 10-16 (2001).

21. *The Kondo effect in the unitary limit*
W. G. van der Wiel, S. De Franceschi, T. Fujisawa, J. M. Elzerman, S.Tarucha, and L. P. Kouwenhoven, Science **289**, 2105-2108 (2000).

22. *Kondo effect in an integer-spin quantum dot*
S. Sasaki, S. De Franceschi, J. M. Elzerman, W. G. van der Wiel, M. Eto, S.Tarucha, and L. P. Kouwenhoven, Nature **405**, 764-767 (2000).

23. *Suppression of the Kondo effect in a quantum dot by microwave radiation*
J. M. Elzerman, S. De Franceschi, D. Goldhaber-Gordon, W. G. van der Wiel, and L. P. Kouwenhoven, Journal of Low Temperature Physics **118**, 375-389 (2000).